

ORDERING OF BLOCK COPOLYMERS AND SMECTIC ELASTOMERS

ORDERING OF BLOCK COPOLYMERS AND
SMECTIC ELASTOMERS

PROEFSCHRIFT

ter verkrijging van de graad van doctor aan de
Technische Universiteit Eindhoven, op gezag van de
Rector Magnificus, prof.dr.ir. C. J. van Duijn, voor een
commissie aangewezen door het College voor
Promoties in het openbaar te verdedigen
op dinsdag 7 juni 2005 om 17.00 uur

door

Denitza Mihailova Lambreva

geboren te Sofia, Bulgarije

Dit proefschrift is goedgekeurd door de promotoren:

prof.dr.ir. W.H. de Jeu
en
prof.dr. M.A.J. Michels

CIP-DATA LIBRARY TECHNISCHE UNIVERSITEIT EINDHOVEN

Lambreva, Denitza M.

Ordering of block copolymers and smectic elastomers/by Denitza M. Lambreva. –
Eindhoven : Technische Universiteit Eindhoven, 2005.

Proefschrift. – ISBN 90-386-3056-5

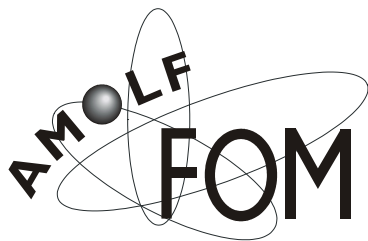
NUR 913

Subject headings: polymer morphology/self-assembly/block copolymers/polymeric liquid
crystals; smectic elastomers/fluorinated alkanes/x-ray scattering

Trefwoorden: polymeermorfologie/zelforganisatie/blokcopolymeren/vloeibare kristallen;
smectische elastomeren/gefluorideerde alkanen/röntgenverstrooiing

Printed by Febodruk – www.febodruk.nl

The work described in this thesis was performed at the FOM-Institute for Atomic and
Molecular Physics (AMOLF), Kruislaan 407, 1098 SJ Amsterdam. This work is part of the
research program of the “Stichting voor Fundamenteel Onderzoek der Materie (FOM)”,
which is financially supported by the “Nederlandse Organisatie voor Wetenschappelijk
Onderzoek (NWO)”.



To my family

This thesis is based on the following articles:

Chapter 3

D.M. Lambreva, R. Opitz, G. Reiter, P.M. Frederik and W.H. de Jeu,
Morphology of an asymmetric ethyleneoxide-butadiene di-block copolymer in bulk and thin films,
Polymer (in press), 2005.

R. Opitz, D. M. Lambreva, and W. H. de Jeu,
Confined crystallization of ethyleneoxide-butadiene di-block copolymers in lamellar films,
Macromolecules 35, 6930, 2002.

L. Li, D. M. Lambreva and W. H. de Jeu,
Lamellar ordering and crystallization in a symmetric block copolymer,
J. Macromol. Sci. B Physics 43, 59, 2004.

Chapter 4

A. Mourran, B. Tartsch, M. Gallyamov, S. Magonov, D.M. Lambreva, B.I. Ostrovskii, I.P. Dolbnya, W. H. de Jeu, M. Moeller,
Self-assembly of the perfluorinated-alkane F14H20 in ultrathin films,
Langmuir 21, 2308, 2005.

Chapter 5

D.M. Lambreva, B.I. Ostrovskii, W.H. de Jeu,
Disorder by random crosslinking in smectic elastomers,
Phys. Rev. Lett. 93, 185702, 2004.

Contents

Chapter 1	General introduction	1
1.1	Ordering in condensed soft-matter systems	2
1.2	Block copolymers	4
1.3	Semi-fluorinated alkanes	7
1.4	Smectic liquid crystal ordering	8
1.5	Goals and organisation of this thesis	9
Chapter 2	Experimental	13
2.1	X-ray scattering	14
2.2	Bulk x-ray methods	17
2.3	Surface x-ray methods	19
2.4	Direct methods	25
2.5	Film preparation by spin-coating	26
Chapter 3	Microphase separation and crystallisation in bulk and thin films of diblock copolymers	29
3.1	Introduction	30
3.2	Block copolymer microphase separation	32
3.3	Experimental	36
3.4	Symmetric PB _n - <i>b</i> -PEO systems	39
3.5	Asymmetric PB _n -PEO system	51
3.6	Concluding remarks	62
Chapter 4	Nano-structures in thin films of semifluorinated alkanes	67
4.1	Introduction	68
4.2	Experimental	70
4.3	Results and discussion	72
4.4	Conclusions	81

Chapter 5	Order and disorder in smectic elastomers	85
5.1	Order and disorder in smectic systems	86
5.2	The structure factor in the smectic phase.....	89
5.3	Smectic elastomers	95
5.4	Experimental.....	96
5.5	Results and discussion	99
5.6	Conclusions.....	106
Chapter 6	Concluding remarks and outlook	111
Summary.....		115
Samenvatting		119
Acknowledgements		123
Curriculum Vitae		125

Chapter 1 General introduction

1.1 Ordering in condensed soft-matter systems

Soft materials like surfactants, block copolymers and liquid crystals can display in their condensed state ordering effects on a mesoscopic scale (typically 5-100 nm). This is due to the intrinsic incompatibilities in the structure of the constituting molecules that can be brought to expression by changing thermodynamic variables like temperature and pressure. Alternatively external fields can be applied, including surface fields from interfaces. Due to this potential to order at a mesoscopic scale, soft condensed matter is easily perturbed by external stimuli. The relaxation times involved are typically of the order of seconds, much longer than the time scale for reorientation of individual (macro)molecules. Hence quite modest fields are sufficient to cause a quite massive reorganisation, often leading to the formation of complex patterns at intermediate length scales. To understand the attendant rich physics, insight is needed in the different types of ordering at various length scales. Some typical molecules involved in ordering processes are pictured in Figure 1.1.

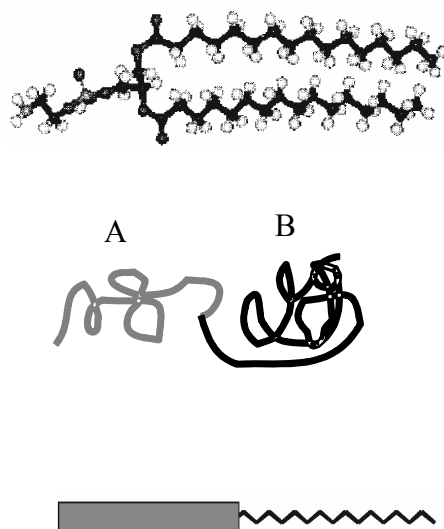


Figure 1.1. *Typical self-assembling soft-matter molecules. From top to bottom: surfactant, diblock copolymer, perfluoroalkyl-alkane.*

On top a conventional surfactant is shown, consisting of a polar head and aliphatic tail(s). Due to this difference the polar part of the molecule is soluble in water and the aliphatic part in hydrocarbons (oils). In a single solvent, the molecules self-assemble in a rich variety of so-called lyotropic liquid-crystal phases such that the insoluble part of the molecule is minimally exposed to the solvent. Though these systems do not play a role in this thesis, they are relevant in connection with the second example: block copolymers. These form the macromolecular equivalent of low-molar-mass surfactants. In block copolymers the chemically different blocks are in general immiscible, but because of their chemical linkage they can only phase separate on a microscopic scale. Finally Figure 1.1 shows a model of a perfluoroalkyl-alkane. Here the intrinsic incompatibility between the hydrogenated and the fluorinated part is limited ('primitive surfactant'). However, the difference in Van der Waals diameter of the two parts now adds to the complex behaviour.

Liquid crystals form a somewhat different class of materials. In the first place the elongated molecules are – on average – aligned with their long axis parallel to each other leading to a preferred direction. When only this orientational ordering is present (nematic phase) the centres of mass of the molecules still have full translational symmetry (liquid state). In the smectic phase a one-dimensional density wave develops parallel to the preferred direction. This leads to a situation of stacks of liquid layers (see Figure 1.2). The one-dimensional density wave in the smectic phase constitutes the simplest case of

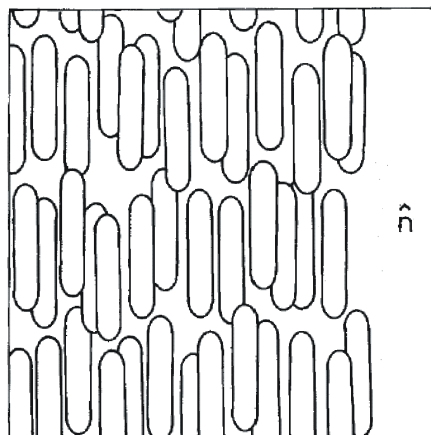


Figure 1.2. *Smectic-A phase displaying 1D positional ordering.*

positional ordering. As a result the smectic-nematic phase transition is the simplest form of melting. The relation with the previous examples lies in the intrinsic density variation in the constituting molecules that is a prerequisite of the smectic density modulation. Hence not surprisingly surfactant and block copolymers can form lamellar phases with properties very similar to the smectic phase. In the following sections we shall introduce the systems relevant to the work in this thesis in some more detail.

1.2 Block copolymers

The simplest case of a block copolymer is a diblock consisting of two covalently bonded polymers with chemically distinct repeat units A and B. If A and B are incompatible, below the order-disorder transition at T_{ODT} microphase separation is obtained into, for example, a spherical, a cylindrical or a lamellar phase. The phase behaviour depends on the relative volume fraction of A and B and on the magnitude of the product $\chi_{\text{AB}}N$, where χ_{AB} is the Flory-Huggins interaction parameter between the two polymers, and N the total degree of polymerisation.¹ We can write

$$\chi_{\text{AB}} = \frac{Z}{k_{\text{B}}T} [\varepsilon_{\text{AB}} - \frac{1}{2}(\varepsilon_{\text{AA}} + \varepsilon_{\text{BB}})] , \quad (1.1)$$

in which ε is the interaction energy and Z the number of relevant nearest neighbours. Note that $\chi \sim 1/T$. In Figure 1.3 both a theoretical² and an experimental³ phase diagram is displayed as function of the block volume fraction f . In case of about equal blocks sizes, the block copolymer microphase separates in a lamellar phase. This result stems from the balance between the enthalpic gain of demixing A and B (Eq. 1.1) and the entropic cost of chain confinement within the layers.^{1,4,5} Note that the experimental phase behaviour, as picture in Figure 1.3b, is somewhat more complicated than the simple theoretical diagram of Figure 1.3a. Additional phases like the gyroid phase (G) with cubic symmetry and a hexagonal perforated lamellar phase (HPL) can intervene.

In thin films the morphology near interfaces can be dramatically affected by the difference in wetting properties of the various blocks at the substrate and at the air

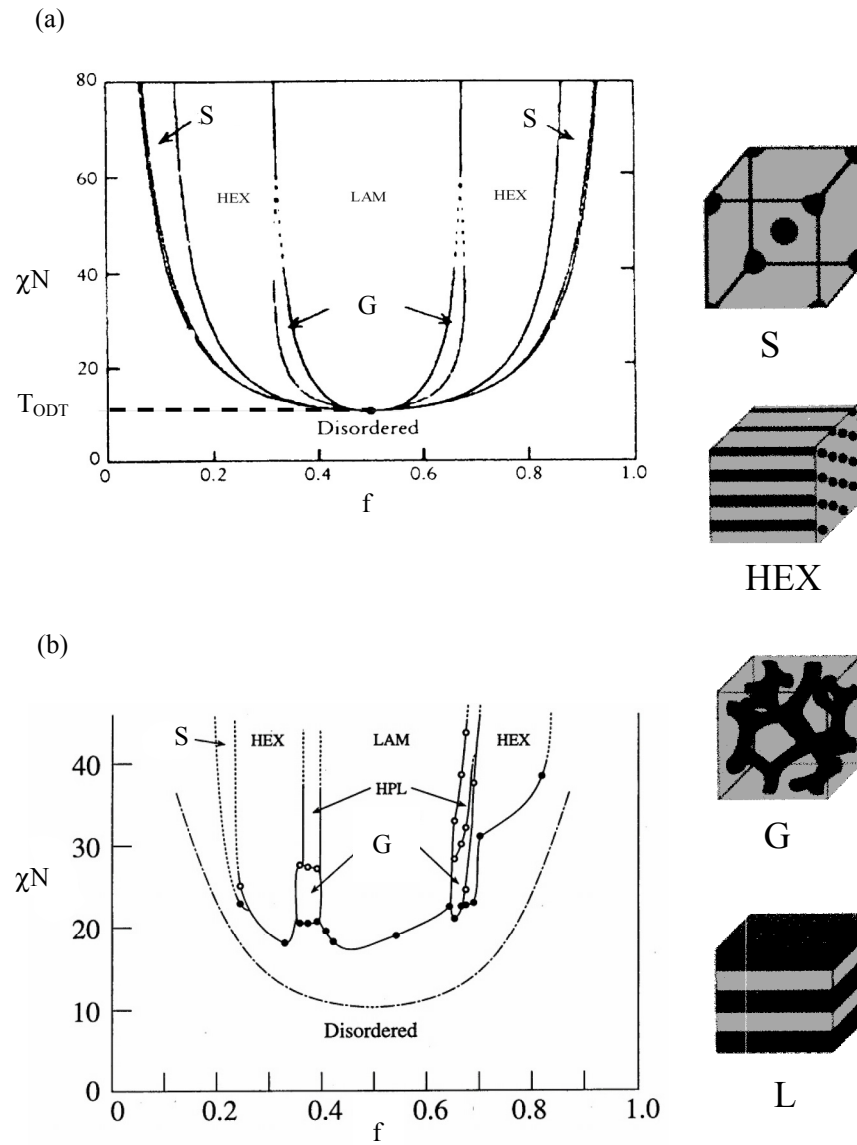


Figure 1.3. (a) Theoretical phase diagram for diblock copolymers.² (b) Experimental phase diagram for PS-PI.³ The right side shows some of the phases observed in diblock copolymers.

interface. As a result the randomly oriented lamellar microdomains become macroscopic lamellae. For example, as we shall see in Chapter 3, in the case of thin block copolymer films of poly-ethylene/butylene (PB_h) and poly-ethyleneoxide (PEO) we find that PEO wets the Si-substrate while PB_h prefers the air interface. This can be accommodated in a simple quantized lamellar structure of thickness $(n+1/2)L$, where L is the ABBA repetition period. Usually the amount of material supplied does not fit in exactly with such a quantized film thickness. Then depressions and elevations are observed for which the film thickness corresponds to $(n+1/2)L$ and $(n+3/2)L$. This situation is schematically sketched in Figure 1.4, both for the asymmetric wetting discussed for PB_h -*b*-PEO as for a situation of symmetric wetting.

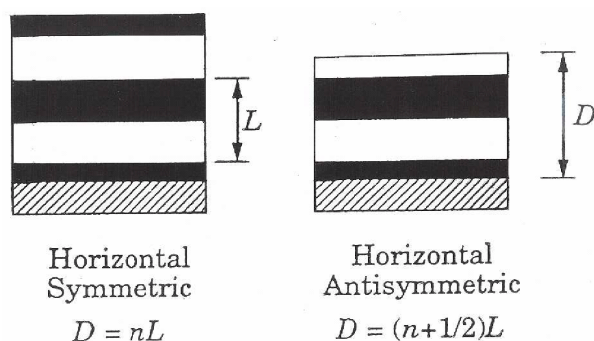


Figure 1.4. *Quantized thickness in thin lamellar diblock copolymer films as a result of the preferential affinity of the blocks.*

In Chapter 3 block copolymers will be considered in more detail, both in bulk and in thin films. We shall also discuss the situation that one block is crystallisable. Then uniform diblock copolymer films provide a precise control of the boundary conditions for crystallisation. In polymer crystallisation folded chain structures occur that are kinetically determined.⁶ In contrast for block copolymers such structures can be in thermodynamic equilibrium, as the extended chain form would lead to an excessive entropy cost of stretching the non-crystallisable block.⁷

1.3 Semi-fluorinated alkanes

Semi-fluorinated alkanes of the general structure $F-(CF_2)_m-(CH_2)_n-H$ (in short F_mH_n) self-assemble in a wide number of different smectic and crystalline phases due to the incompatibility between the fluorinated and the alkylated part. The incompatibility arises from the presence of the two ‘mutually phobic’ blocks, a fluorinated and a hydrogenated chain, linked by a covalent bond. Though both segments dislike water, the atomic properties of fluorinated part are very different from those of the hydrogenated tail. The fluorinated part has higher electronegativity and a reduced conformational freedom giving typically a helical conformation (see Figure 1.5). This in turn leads to stiff bulky chains, in contrast to the hydrogenated part that is flexible due to a relatively low barrier to gauche-trans conformation. As a result the Van der Waals radius of the fluorinated part exceeds that of the hydrocarbon tail in its all-trans ground state (as pictured in Figure 1.5) by 25-30%.

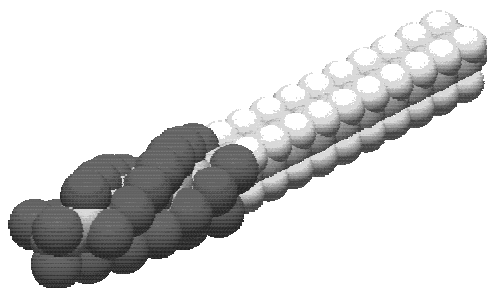


Figure 1.5. *Model of an F_mH_n molecule. The dark and light sections indicate the fluorinated and hydrogenated parts, respectively.*

Semifluorinated alkanes F_nH_m self-assemble in a variety of crystalline and mesogenic phases. The electron-rich outer part of the fluorinated chain gives low intermolecular interactions leading to a low surface tension and extraordinary spreading properties. In films of molecular thickness the geometrical constraints imposed by the interfaces in combination with the competing ordering of the building blocks can result in structures that differ significantly from the bulk smectic phases.^{8,9} When a Langmuir-Blodgett monolayer

of F_8H_{16} is transferred onto a silicon oxide surface, scanning force microscopy investigations shows that the layer consists of monodisperse discrete aggregates. The formation of such structures has been explained by surface induced aggregation, i.e., as ‘surface micelles’, whose size is controlled by the density mismatch between the fluorinated and hydrogenated segments in dependence of their relative length.^{10,11} The interactions between the fluorinated segments dominate the ordering while the hydrocarbon blocks form a liquid-like layer.^{12,13} In Chapter 4 we shall discuss monolayers of $F_{14}H_{20}$ deposited on a silicon substrate, for which these properties play an essential role in the formation of self-assembled nanostructures.

1.4 Smectic liquid crystal ordering

Long-range translational order is a defining quality of three-dimensional (3D) crystals; it leads to the existence of Bragg reflections in x-ray scattering. In a 3D crystal the particles vibrate around well-defined lattice positions with amplitudes small compared to the lattice spacing. As the dimensionality is decreased, fluctuations become increasingly important. As a result long-range translational order cannot exist below 3D; it would be destroyed by thermal fluctuations.¹⁴ For example, for a 2D solid the positional correlation decays algebraically as a function of distance. The 1D layer correlations in a smectic-A phase show a similar behaviour. This property lies at the basis of the fundamental interest in smectic phases as model systems of low-dimensional order. The correlation function describing the smectic layer periodicity decays as $r^{-\eta}$, in which the exponent η is small and positive. It can be studied by high-resolution x-ray scattering. The delta-function type Bragg peaks with diffuse tails characteristic of a 3D crystal periodicity change into Caillé lineshapes with an asymptotic power-law form.¹⁵

A combination of liquid crystalline (LC) ordering and macromolecular properties can be obtained on a macroscopic scale in LC polymers. For example LC or mesogenic units can be built into a polymer as side groups attached to the polymer backbone: comb-shaped LC polymers. Various types of LC phase (nematic, smectic) can be found, just as in the corresponding monomers. In the case of a smectic phase the 1D quasi-long-range layer ordering can be combined with polymer properties. The backbone polymer, in turn, can be

weakly crosslinked to form an elastomer (see Figure 1.6).¹⁶ The macroscopic rubber elasticity introduced via such a percolating network interacts with the LC ordering field. This gives rise to a rich theoretical behaviour that will be considered in Chapter 5. In fact two opposing tendencies are predicted. (i) Crosslinks pin the smectic layers in a number of points, thus suppressing long-wave layer fluctuations. If the suppression of the fluctuations is strong enough this can restore true long-range order. (ii) Crosslinks disturb the local layer structure and give rise to dislocations that preferentially reduce the smectic density around their position and could destroy the smectic ordering.

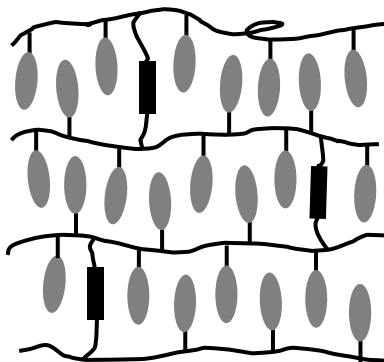


Figure 1.6. Schematic picture of a smectic elastomer.

1.5 Goals and organisation of this thesis

In the previous sections we have introduced various soft-matter systems that have as common property intrinsic molecular incompatibilities that act as a source for self-assembly. The objective of the work to be described in this thesis is to investigate and where possible control the self-assembly by varying external conditions (bulk, thin films) as well as specific molecular parameters. Emphasis is on a precise evaluation of the resulting structures, for which advanced x-ray methods have been used, complemented by atomic force and optical microscopy. The choice of the specific systems is largely determined by historical reasons, and partly also by co-operations within the EU Marie-Curie Research and Training Network POLYNANO.

The structure of the thesis is as follows. After this general introduction in Chapter 2 the various experimental methods – in the first place x-ray scattering, but also optical and atomic force microscopy – will be discussed. Chapter 3, 4 and 5 form the core of the thesis and can be read to a large extent independently. Chapter 3 is concerned with ordering and crystallisation in block copolymers, both in the bulk and in thin films. In Chapter 4 nanostructures formed by monolayers of the semifluorinated alkane $F_{14}H_{20}$ are discussed. Finally in Chapter 5 ordering and disordering effects are investigated due to random crosslinking smectic elastomers.

References

- [1] Bates, F. S., Frederickson, G. H., *Annu. Rev. Phys. Chem.* 41, 525, 1990.
- [2] Matsen, M. W., Schick, M., *Phys. Rev. Lett.* 72, 2660, 1994.
- [3] Khandpur, A. K., Forster, S., Bates, F. S., Hamley, I. W., Ryan, A. J., Bras, W., Almdal, K., Mortensen, K., *Macromolecules* 28, 8796, 1995.
- [4] Bates, F. S., Frederickson, G. H., *Physics Today, February* 52(2), 32, 1999.
- [5] Hamley, I. W., *The Physics of Block Copolymers* (Oxford University Press, New York), 1998.
- [6] Keller, A., Goldbeck-Wood, G., p. 241 in *Comprehensive Polymer Science, 2nd Supplement*, S.L. Aggarwal and S. Russo, eds., Elsevier, Oxford, 1996.
- [7] M.D. Whitmore, J. Noolandi, *Macromolecules* 21, 1482, 1988.
- [8] Marczuk, P., Lang, P., Findenegg, G. H., Mehta, S. K., Moeller, M., *Langmuir* 18, 6830, 2002.
- [9] Gang, O., Ellmann, J., Moeller, M., Kraack, H., Sirota, E. B., Ocko, B. M., Deutsch, M., *Europhys. Lett.* 48, 761, 2000.
- [10] Maaloum, M., Muller, P., Krafft, M.-P. *Angew. Chem., Int. Ed.* 41, 4331, 2002.
- [11] Krafft, M. P., Giulieri, F., Fontaine, P., Goldmann, M., *Langmuir* 17, 6577, 2001.
- [12] Huang, Z., Acero, A. A., Lei, N., Rice, S. A., Zhang, Z., Schlossman, M. L. J., *Chem. Soc., Faraday Trans.* 92, 545, 1996.
- [13] Krafft, M.-P., *Curr. Opin. Colloid Interface Sci.* 8, 243, 2003.
- [14] Chaikin, P. M., Lubensky, T. C., *Principles of Condensed Matter Physics* (Cambridge University Press), 1995.
- [15] Als-Nielsen, J., Litster, J. D., Birgeneau, R. J., Kaplan, M., Safinya, C. R., Lindegaard-Andersen, A., Mathiesen, S., *Phys. Rev. B* 22, 312, 1980.
- [16] M. Warner and E. M. Terentjev, *Liquid Crystal Elastomers* (Clarendon Press, Oxford), 2003.

Chapter 2 Experimental

In this chapter we discuss the various experimental methods that play a role in the work to be presented in this thesis. A variety of x-ray methods have been applied to probe bulk structures (small- and wide-angle x-ray scattering) and surface ordering (x-ray reflectivity and grazing-incidence x-ray diffraction). In several cases the x-ray results were complemented with direct images from atomic force microscopy and optical microscopy. In this chapter we summarize the basic principles of these methods and the main experimental features. In addition some aspects of sample preparation will be described.

2.1 X-ray scattering

As introduction for the x-ray methods described in the subsequent sections, we give in this part the basic quantities and definitions regarding x-ray scattering. A complete overview on the subject is given in Ref. 1 and 2. When an x-ray beam impinges on a medium, it induces secondary radiating sources by the interaction with the individual electrons that constitute the material. Classically, the wavelength λ of the outgoing wave is the same as that of the incident one, and the scattering is considered to be elastic. Figure 2.1 gives a sketch of a general set-up of a scattering experiment. An incident monochromatic x-ray beam with wave vector \mathbf{k}_i scatters from a sample and the intensity of the scattered waves $I(q)$ with wave vector \mathbf{k}_o is registered by a detector, while $|\mathbf{k}_i| = |\mathbf{k}_o| = k = 2\pi/\lambda$. The wave vector transfer is given by $\mathbf{q} = \mathbf{k}_o - \mathbf{k}_i$ in which $q = |\mathbf{q}|$ is related to the scattering angle 2θ by $q = (4\pi/\lambda)\sin\theta$.

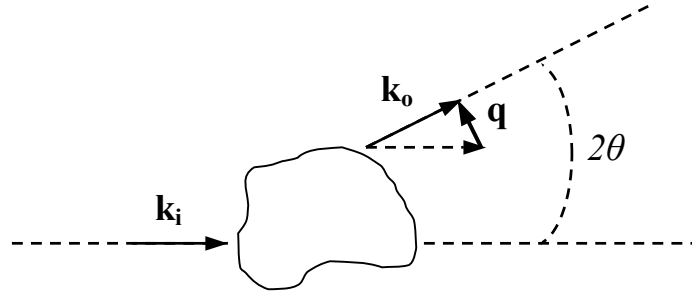


Figure 2.1. *Typical scattering geometry showing the incident, outgoing and scattering wave vectors \mathbf{k}_i , \mathbf{k}_o , and \mathbf{q} .*

The main objective in measuring $I(\mathbf{q})$ is to obtain information on the structure of the sample as contained in the electron density distribution function $\rho(\mathbf{r})$. As a starting point, we note that the total amplitude $A(\mathbf{q})$ of the scattered waves is related to the Fourier transform of $\rho(\mathbf{r})$:

$$A(\mathbf{q}) = A_0 r_{\text{el}} P(\theta) \frac{e^{ikR}}{R} \int_V \rho(\mathbf{r}) e^{i\mathbf{q}\cdot\mathbf{r}} d\mathbf{r}. \quad (2.1)$$

In this equation A_0 is the amplitude of the incident wave, r_{el} is the classical electron radius, $P(\theta)$ is a constant factor related to the polarization of the incident wave, $\rho(\mathbf{r})d\mathbf{r}$ is the number of electrons at position \mathbf{r} in a volume element $d\mathbf{r}$ and R is the distance from the scattering volume V to the observation point (detector). During measurement the positions of the scattering elements change and therefore the intensity is averaged over time $I(\mathbf{q}) = \langle A(\mathbf{q})A^*(\mathbf{q}) \rangle$. The $\langle \dots \rangle$ denotes ensemble average, which is equivalent to time average if the scattering medium is ergodic. The intensity of the scattered beam $I(\mathbf{q})$ is defined by the structure factor $S(\mathbf{q})$, given by:

$$S(\mathbf{q}) = \int d\mathbf{r} G(\mathbf{r}) e^{i\mathbf{q}\cdot\mathbf{r}}, \quad (2.2)$$

where $G(\mathbf{r})$ is defined as

$$G(\mathbf{r}) = \int \rho(\mathbf{u}) \rho(\mathbf{u} + \mathbf{r}) d\mathbf{u}. \quad (2.3)$$

$G(\mathbf{r})$ is the density-density autocorrelation function and specifies how, on average, the densities in neighbouring regions separated by a distance $\mathbf{r} = \mathbf{u}' - \mathbf{u}$ are correlated to each other. As a result a reconstruction of $G(\mathbf{r})$ from $S(\mathbf{q})$ yields information on the nature of the translational order of the system, as will be discussed in more detail in Chapter 5. Note that $\rho(\mathbf{r})$ can be converted to $G(\mathbf{r})$ and $S(\mathbf{q})$, however there is no way to perform the reverse operation. Consequently, given that the scattered amplitude is a complex quantity, information on the phase is lost. The alternative practice is to assume a model structure and check whether the derived intensity pattern $I(\mathbf{q})$ agrees with the experimentally determined one. Hence the question whether the chosen model represents the unique solution to the problem always remains.

Two major theoretical approaches are in use for treating the scattering process. Kinematical scattering theory (or first Born approximation) is based on the assumption that for a given incident x-ray beam, the scattering process in the sample occurs at most once. This assumption is correct if the scattering represents a weak disturbance of the transmitted wave, in which case the probability of a scattered wave to be scattered again is small. Alternatively, dynamic scattering theory is needed that takes multiple scattering processes into account. Yet, under some broad assumptions concerning the type of structure, some

basic information can be directly extracted from $I(\mathbf{q})$. For the scattering from a material with a density variation that is periodic in space, Bragg's law holds:

$$m\lambda = 2d \sin \theta, \quad (2.4)$$

where m is an integer. This condition refers to constructive interference of waves from a set of lattice planes at a distance d apart. The position of the Bragg peaks in the spectrum of $I(\theta)$ allows determination of the periodicities related to the specific unit cell.

Long-range translational order in ideal three-dimensional (3D) crystals results in delta-function type diffraction peaks. However, in reality various types of complication arise. At finite temperatures thermal vibrations reduce the intensity of Bragg peaks by a Debye-Waller factor, $\exp[-q_n^2 \langle u^2(\mathbf{r}) \rangle]$, where $u(\mathbf{r})$ is the displacement from the time-averaged mean position of lattice site. In addition this also introduces diffuse tails. Furthermore, for finite-size samples (small crystals) the width of the diffraction peaks increases due to the truncation of the periodicity. It can be expressed in terms of the crystallite size; more details will be given in Chapter 5. In systems with a dimensionality lower than three, thermal fluctuations destroy any long-range translational order. In 2D crystals the ordering decays algebraically, leading to power-law singularities instead of delta function peaks. These are referred to as quasi-Bragg peaks and differ from true Bragg behaviour by a slow fall-off of the diffuse tails. Hence, the lineshape associated with an x-ray peak carries information about the nature of ordering. In conventional liquid the positional correlations decay exponentially with distance, giving a Lorentzian scattering profile with a width inversely proportional to the correlation length ξ .

$$S(\mathbf{q}) \propto \frac{1}{\xi(q - q_0)^2 + 1}. \quad (2.5)$$

In practice, the overall intensity observed in a scattering experiment is expressed as a convolution of the structure factor $S(\mathbf{q})$, the form factor $F(\mathbf{q})$ (scattering from the basic unit) and the instrumental resolution function $R(\mathbf{q})$:

$$I(\mathbf{q}) = S(\mathbf{q}) \otimes F(\mathbf{q}) \otimes R(\mathbf{q}). \quad (2.6)$$

The resolution function describes the dispersions Δq_j ($j = x, y, z$) relative to \mathbf{k}_i and \mathbf{k}_o due to the random deviations in the various angles involved in the scattering geometry. For most practical purposes these deviations are small and statistically independent and thus can be described by a Gaussian distribution. As a result $R(\mathbf{q})$ can be written as³

$$R(\mathbf{q}) = \frac{(2\pi)^{-2/3}}{\Delta q_x \Delta q_y \Delta q_z} \exp\left(-\frac{1}{2} \frac{q_x^2}{\Delta q_x^2}\right) \exp\left(-\frac{1}{2} \frac{q_y^2}{\Delta q_y^2}\right) \exp\left(-\frac{1}{2} \frac{q_z^2}{\Delta q_z^2}\right). \quad (2.7)$$

As the Fourier transform of a Gaussian is again a Gaussian, this result is convenient for analysis purposes. It allows a straightforward deconvolution of the experimental data – often also described by a Gaussian lineshape – as the convolution of two Gaussians of width σ_1 and σ_2 is another Gaussian of width $(\sigma_1^2 + \sigma_2^2)^{1/2}$.

2.2 Bulk x-ray methods

2.2.1 Fundamentals

Small-angle x-ray scattering (SAXS) probes length scales of 1-100 nm. This range covers typically microstructures of block copolymers as well as the ‘long period’ (lamellar thickness) occurring in polymer crystallisation. Of course, a prerequisite is always that sufficient electron density contrast is needed between the scattering elements that form the periodic structure. In general a number of Bragg reflections d_{hkl} will be observed that depend on the symmetry of the lattice and which are related to the unit cell parameters hkl (Miller indexes). As a relevant example for this thesis, the reflections d_{hkl} associated with a hexagonal lattice can be written as

$$\frac{1}{d_{hkl}^2} = \frac{4}{3} \left(\frac{h^2 + hk + k^2}{a^2} \right) + \frac{l^2}{c^2}. \quad (2.8)$$

In this equation a , b and c are the lattice parameters that define the unit cell, for the hexagonal case $a = b$ with $\alpha = \beta = 90^\circ$ and $\gamma = 120^\circ$. In the case of block copolymers, the

relative positions of the x-ray reflections corresponding to a set of d_{hkl} - values usually allow an unambiguous identification of the morphology. Some typical ratios of q -values relative to the fundamental reflection at q^* are given for various symmetries in Table 2.1.

Table 2.1. Ratios q/q^* for Bragg reflections from various structures.

Structure	Ratio q/q^*
Lamellar	1: 2: 3: 4: 5: 6 ...
Hexagonal	1: $\sqrt{3}$: $2=\sqrt{4}$: $\sqrt{7}$: $3=\sqrt{9}$: $\sqrt{11}$...
Cubic bcc	1: $\sqrt{2}$: $\sqrt{3}$: $2=\sqrt{4}$: $\sqrt{5}$: $\sqrt{6}$...
Cubic fcc	1: $\sqrt{(4/3)}$: $\sqrt{(8/3)}$: $\sqrt{(11/3)}$: $2=\sqrt{(12/3)}$: $\sqrt{(16/3)}$...
Cubic gyroid	1: $\sqrt{(4/3)}$: $\sqrt{(7/3)}$: $\sqrt{(8/3)}$: $\sqrt{(10/3)}$: $\sqrt{(11/3)}$: $2=\sqrt{(12/3)}$: $\sqrt{(13/3)}$: $\sqrt{(15/3)}$...

Wide-angle x-ray scattering (WAXS) concerns scattering at relatively large angles and assesses structures with repeat distances less than 1 nm. Applications of WAXS in polymer science are the determination of crystallinity, of the unit cell dimensions and of the strain in the crystalline phase. Evidently the combination of SAXS and WAXS is very appropriate for many anisotropic systems. We performed simultaneous SAXS/WAXS to determine mesophase structures in block copolymers (SAXS) and to assess any crystallization process within one of the blocks (WAXS).

2.2.2 In-house SAXS-WAXS set-up

Figure 2.2 shows the in-house SAXS/WAXS set-up built at AMOLF and used for most of the experiments presented in this thesis. It consists of an x-ray generator (Rigaku RU-300, 18 kW, copper target, focus $0.5 \times 1 \text{ mm}^2$), equipped with two graded parabolic multilayer mirrors (Bruker, Karlsruhe, $40 \times 20 \text{ mm}^2$, $60 \times 20 \text{ mm}^2$). The use of these mirrors has two important effects. First it leads to an almost parallel x-ray beam with a divergence of about 12 mdeg. Second the take-off angle with respect to the source is increased to several degrees. In bypassing, the mirrors also act as monochromator, separating the CuK_α and CuK_β lines. As a result the flux at the CuK_α wavelength of $\lambda = 0.154 \text{ nm}$ is an order of magnitude larger compared to conventional slit/pinhole collimation and a nickel filter. The beam size of about $0.6 \times 0.6 \text{ mm}^2$ is defined by the first two slits ($0.6 \times 0.6 \text{ mm}$) of a

collimation system. The third and last slit (1.14×1.14 mm) acts as guard slit to reduce the background. The SAXS and WAXS intensities are recorded by a 2D detector (Bruker Hi-Star) and by a linear one (PSD-50M, M. Braun), respectively. A semi-transparent beamstop is placed in front of the SAXS detector, which allows monitoring of the beam intensity. Finally a Linkam CSS 450 temperature-controlled shear system serves as sample stage.

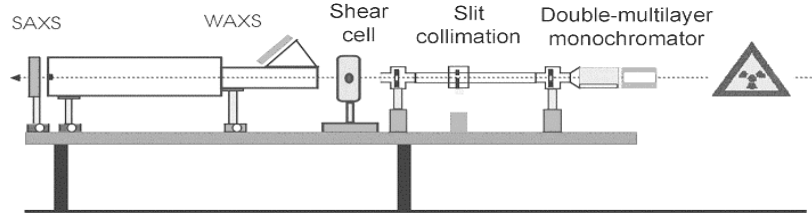


Figure 2.2. Scheme of the in-house SAXS/WAXS set-up.

2.3 Surface x-ray methods

2.3.1 X-ray reflectivity

The scattering of x rays from a planar interface can be described in optical terms like reflection and we speak of x-ray reflectivity. This approach can be extended to thin films (say up to tens of μm) like polymer films on a substrate, Langmuir films, smectic membranes, etc. The method provides information on film thickness, the roughness (fluctuations) of the interfaces, and the laterally averaged electron-density profile perpendicular to the interfaces. In this approach the medium can be considered as an ensemble of free electrons with a refractive index n deviating only slightly from unity: $n = 1 - \delta + i\beta$. Here $\delta = \rho r_e \lambda^2 / (2\pi)$ while $\beta = \mu \lambda / (4\pi)$ where $1/\mu$ is the absorption length of x-rays in the medium. For the materials studied in this thesis typically $\delta \approx 10^{-6}$. Hence the wavelength inside the material is almost indistinguishable from that in vacuum. Furthermore $\beta \approx 10^{-8}$ and we can neglect absorption in the following.

The x-ray reflectivity geometry is presented in Figure 2.3a. Under specular conditions the exit angle θ_o is equal to the impinging angle θ_i ; then the momentum transfer \mathbf{q} is normal to the surface. As for x rays $n < 1$, thus a critical angle of total reflection θ_c exists. For $\theta < \theta_c$

the incident wave is totally reflected from the interface and only an evanescent wave is travelling parallel to the surface. For small angles and using $\delta \ll 1$, according to Snell's law $\cos\theta_c = 1 - \delta$ and we find $\theta_c \approx (2\delta)^{1/2} = \lambda(\rho r_e \pi)^{1/2}$. In practical situations this leads to total

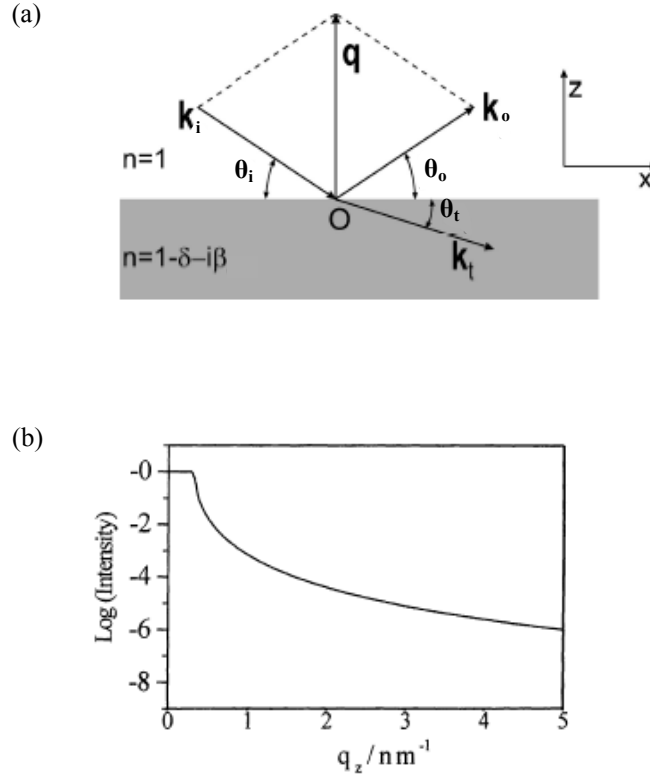


Figure 2.3. (a) Scattering geometry for x-ray reflectivity experiment. (b) Fresnel reflectivity of a single smooth interface.

reflection below $\theta_c \approx 0.2^\circ$. The intensity of an electromagnetic wave reflected at an ideally sharp interface can be derived straightforwardly from Maxwell's equations. The result is called the Fresnel reflectivity R_F , which is defined as the ratio of the intensities of the reflected and the incoming beam.⁴ R_F can be written as

$$R_F \approx \left(\frac{q_c}{2q} \right)^4 = \frac{16\pi^2 \rho^2 r_e^2}{q^4}. \quad (2.9)$$

At large angles the reflected intensity decays as q^{-4} . Owing to the rapid falloff in intensity with increasing angle, the range of q in reflectivity measurements is small, typically $q_{\max} \approx 6 \text{ nm}^{-1}$ (see Figure 2.3b).

In the case of non-ideal stratified medium (film) with thickness D the reflectivity can be calculated directly using Parratt's dynamical matrix method,⁵ taking multiple scattering, refraction and absorption into account. The reflectance at an interface between layer j and $(j+1)$ is given by the Fresnel coefficient

$$r_{j,j+1} = \frac{q_{j+1} - q_j}{q_{j+1} + q_j}. \quad (2.10)$$

For a single slab the ratio of reflected to incident intensity from the total film becomes $R_F(q) = r r^*$ in which

$$r = \frac{r_{0,1} + r_{1,2} e^{-iq_1 L}}{1 + r_{0,1} r_{1,2} e^{-iq_1 L}}. \quad (2.11)$$

The result is shown in Figure 2.4. Constructive and destructive interference of x-rays reflected from the top and bottom of the film occurs with a period $2\pi/D$. As a result the

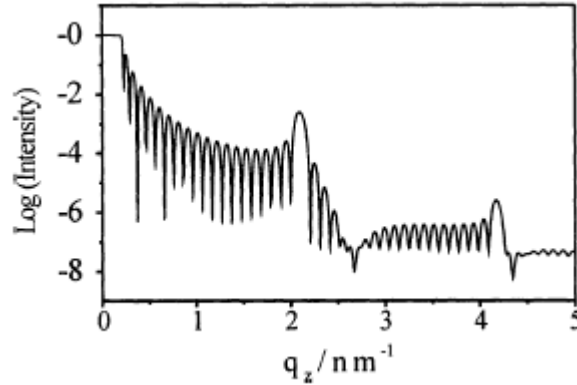


Figure 2.4. Calculated reflectivity from a stratified film with a periodic variation of δ .

reflectivity curve exhibits a series of oscillations, the so-called Kiessig fringes. The amplitude of these oscillations depends on the contrast in electron density between the film and the surrounding material. In addition, the scattered waves yield finite-size broadened Bragg peaks. Interference between the Fresnel reflection and Bragg scattering enhances and extinguishes the scattered intensity at q -values directly below and above the Bragg positions, respectively. In fact this involves phase information of the layering, and the situation depicted describes a low-density termination at the interfaces.

So far only sharp interfaces have been considered, which does not apply to reality. In many situations the interface roughness can be described by a Gaussian function with a width σ corresponding to the mean-square roughness. This leads to an error function for the refractive index profile. Roughness can be incorporated into the reflectance by multiplying the Fresnel coefficient in Eq. 2.10 by a Gaussian factor leading to⁶

$$r_{j,j+j} = \frac{q_{j+1} - q_j}{q_{j+1} + q_j} \exp(-2q_i q_j \sigma_{i,j}^2). \quad (2.12)$$

Note that a similar expression would be found for a flat graded interface. On the basis of specular reflectivity alone one cannot discriminate between these two cases. However, a rough surface also scatters diffusely while a graded interface does not. Measurements of both mean level and amplitude of the fringes far from a Bragg peak enable a determination of the mean squared roughness.

In actual experiments we use specular reflectivity scans and rocking scans. A specular reflectivity scan maps reciprocal space along q_z by varying θ_i keeping $\theta_i = \theta_o$. Rocking scans are needed to align the sample and to assess the misorientation of the layering (mosaic distribution). Fixing the detector at an angle 2θ (specular position) while the sample is rocked in the beam gives a rocking curve with a full-width-at-half-maximum (FWHM) that directly reflects the distribution of the layer normal in the sample.

To fit the experimental data we use the REFLAN software package.^{7,8} This program calculates the reflected intensity using the recursive matrix formalism, taking the deviations from the ideal decay of the reflectivity for a perfectly smooth surface due to the presence of roughness into account. The fitting consists of two stages. In the first step the program finds

the local minimum difference corresponding to the initial trail structure. During the second stage this structure is progressively distorted exploring the whole parameter space and eventually finding the global minimum. The method is also known as successive descent from local minima. Constraining the parameters makes it possible to bias the process towards relevant solutions. The calculated reflectivity profiles were convoluted with the experimental resolution. During the minimization process the experimental errors are taken into account by weighting the data accordingly.

2.3.2 In-house x-ray reflectivity set-up

Figure 2.5 presents the two-circle diffractometer attached to the same rotating anode x-ray generator mentioned before, working again at $\lambda = 0.154$ nm (CuK $_{\alpha}$ -line). A single graded parabolic W/B $_4$ C multilayer mirror reduces the divergence of the incident beam to about 25 mdeg in the horizontal scattering plane (xz -plane, z -axis along the film normal). Additional pre-sample (S2) and pre-detector slits (S4) collimate the beam further horizontally as well as perpendicular to the scattering plane. The overall in-plane resolution is given by $\Delta q_z = 0.043$ nm $^{-1}$ and $\Delta q_x = (5 \times 10^{-3}) q_z$.

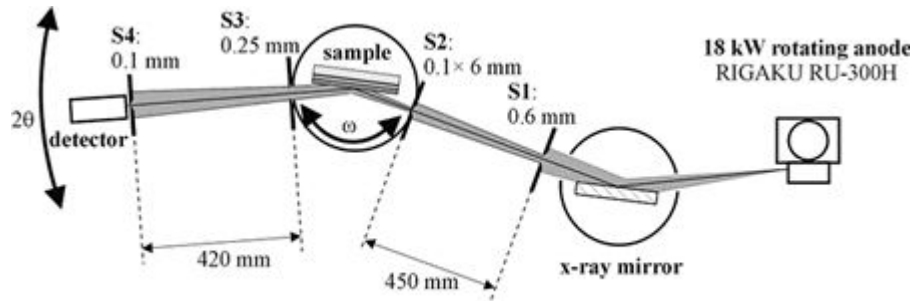


Figure 2.5. Scheme of the in-house reflectivity set-up.

2.3.3 Grazing incidence x-ray diffraction

We used grazing incidence x-ray diffraction (GIXD) to probe the in-plane structure at the free surface of polymer films. To perform a GIXD experiment the incident angle is set at $\theta_i \leq \theta_c$, in a condition of total external reflection (see Figure 2.6). Hence only an evanescent

wave penetrates the sample below the surface. The amplitude of the evanescent wave decays exponentially with the penetration depth Λ (1/e value), given by⁶

$$\Lambda = \frac{\lambda}{2\pi\sqrt{2}} \left\{ \sqrt{(\theta_i^2 - \theta_c^2 + 4\beta^2) - (\theta_i^2 - \theta_c^2)} \right\}^{-1/2}. \quad (2.13)$$

For $\theta_c \rightarrow 0$, $\Lambda = \lambda/(2\pi\theta_c) \approx 5 - 40$ nm indicating that only the top layer(s) are probed.

Figure 2.7 shows Λ as a function of θ_i/θ_c for different ratios of β/δ . By scanning the detector angle δ out of the specular scattering plane, the intensity is measured as a function of the in-plane component q_{xy} of the wave vector transfer. Note that in GIXD the reference surface is

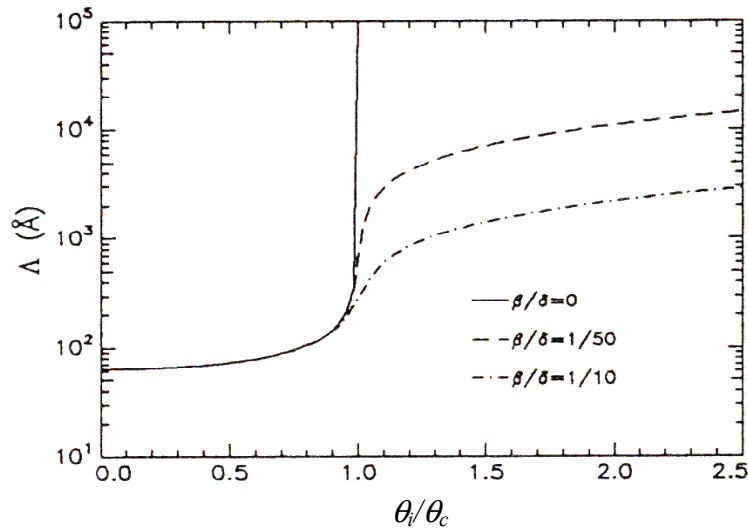


Figure 2.7. Penetration depth Λ of x-rays ($\lambda=0.154$ nm) into silicon as a function of the normalized angle of incidence θ_i/θ_c for different adsorption/dispersion ratios β/δ . (After Ref. 6)

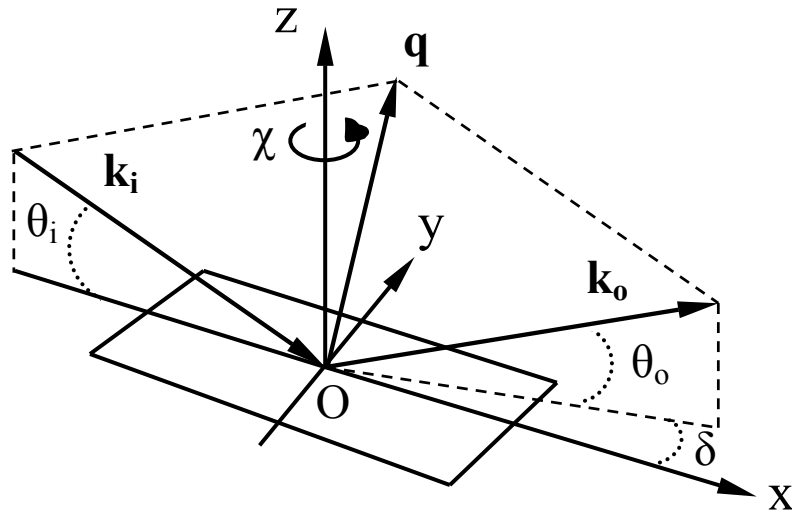


Figure 2.6. *General scattering geometry. For grazing-incidence diffraction the angle δ is varied for $\theta_i \leq \theta_c$.*

a lattice plane whereas it is the physical surface for x-ray reflectivity. The resulting peak position and its width provide information about the in-plane ordering at the surface averaged over the penetration depth. Furthermore, by measuring the scattered intensity along q_z at in-plane diffraction peaks by varying θ_o , so-called Bragg rods are obtained that provide form-factor information including possible orientation effects.

GIXD experiments have exclusively been performed at synchrotron sources, taking advantage of the large x-ray flux. Details of the respective instrumental characteristics will be given in the particular chapters.

2.4 Direct methods

2.4.1 Atomic force microscopy

Atomic force microscopy (AFM) can be applied to characterize nanoscale structures at the surface of bulk materials as well as of thin film systems. We have mainly used AFM to assess the morphology of diblock copolymer films with different composition and

thickness. With AFM the deflection of a cantilever is measured due to the repulsive interactions of an attached sharp tip with the surface. The microscopic movement of the tip creates a force with a certain magnitude, which is mapped as a digital image of the surface structure. In the resonant or tapping mode the tip oscillates with a particular frequency and amplitude close to the surface. The surface forces in the vicinity of the sample lead to damping of the vibrating amplitude, which yields information about the surface topography. In addition the phase shift between the oscillator frequencies of driver and tip is monitored to obtain a phase image. The latter provides information on the visco-elastic response of the sample.

The experiments were performed using a Solver AFM from NT-MDT (Zelenograd, Russian Federation). Typically a vibrating cantilever with a resonant frequency of about 300 kHz and a silicon tip with a radius of curvature less than 10 nm were used.

2.4.2 Optical microscopy

Optical microscopy with visible light reveals details with a resolution of the order of μm , limited by the objective lens and the wavelength of the light. For block copolymers, it allows assessment of processes such as melting, crystallization and order-disorder transitions. We used a Leitz Orthoplan microscope equipped with a Linkam THMS600 hot stage to examine thin film surfaces. All images were taken in the reflection mode using a white light source in order to obtain interference colours.

2.5 Film preparation by spin-coating

Spin-coating is the preferred method for preparation of thin, uniform layers on a flat surface. The process can be separated into two stages. The first one is deposition of an excess amount of solution on a substrate fixed to a turntable. During the second stage the substrate is accelerated up to the desired rotation speed (typically 2000-3000 rpm). The centrifugal force associated with the rotation spreads the fluid while the volatile solvent evaporates simultaneously. During this process the fluid thins gradually and in general quite uniformly. Nevertheless edge effects are often observed. As the solution flows uniformly

outwards, droplets form at the edge of the substrate to be flung off. Thus, depending on surface tension, viscosity, rotation speed and time, a small difference in the thickness may be found between the rim and the central part of the final coating.

In the present work the substrate was always a silicon wafer, covered by a natural SiO₂ layer. The spin-coating process took place in a class 100 dust-free cabinet. In addition the polymer solutions were applied through a sub-micron filter to eliminate dust particles from the solvent that could lead to flaws. After spinning the films were annealed in an inert atmosphere at 50-60°C to remove the final traces of solvent. Depending on the system, subsequently the sample was annealed at higher temperatures to reach equilibrium ordering corresponding to the preferential affinity of its components to the surfaces.

References

- [1] Warren, B. E., X-ray Diffraction (Dover Publications, New York), 1990.
- [2] Hukins, D. W. L., X-ray Diffraction by Disordered and Ordered Systems (Pergamon Press, Oxford), 1984.
- [3] Sentenac, D., Shalaginov, A. N., Fera, A., de Jeu, W. H., *J. Appl. Crystallogr.* 33, 130, 2000.
- [4] Born, M., Wolf, E., Principles of Optics (Pergamon, Oxford), 1959.
- [5] Parrat, L. G., *Phys. Rev.* 95, 359, 1954.
- [6] Tolan, M., X-ray Scattering from Soft-Matter Thin Films (Springer, Berlin), 1998.
- [7] Samoilenko, I. I., Shchedrin, B. M., Feigin, L. A., *Physica B* 221, 542, 1996.
- [8] Samoilenko, I. I., Konovalov, O. V., Feigin, L. A., Shchedrin, B. M., Yanusova, L. G., *Cryst. Rep.* 44, 310, 1999.

Chapter 3 Microphase separation and crystallisation in bulk and thin films of diblock copolymers

*In this chapter we consider microphase separation and crystallisation in a series of poly(butadiene-*b*-ethyleneoxide) diblock copolymers. Two approximately symmetric compounds with different molecular masses form lamellar phases. They are investigated in bulk and in thin films with respect to the microphase separation and the crystallisation of the polyethyleneoxide block. In the latter case the amorphous block provides a rubbery confinement for the crystallisation process. In addition an asymmetric compound is considered with an hexagonal cylinder morphology in the bulk. In this situation the crystallisation of the polyethyleneoxide block leads to competition and coupling of the microphase separation and the crystallisation.*

3.1 Introduction

Semicrystalline-amorphous block copolymers provide unique opportunities to examine the interplay of various types of phase transitions, resulting in a rich phase behaviour including molecular ordering over several length scales. Below the order-disorder transition at a temperature T_{ODT} , microphase separation drives the formation of nanoscale lamellae, cylinders or other structures, depending on the degree of incompatibility and the volume fractions of the A- and B-blocks.¹ However, upon crystallisation of one of the blocks the development of crystalline lamellae is favoured.²⁻⁴ These processes depend strongly on the particular morphology, the degree of supercooling and the nature of the confinement.^{5,6} In particular when T_{ODT} and the melting temperature T_{m} are close, competition and coupling between the microphase separation and crystallisation can occur.⁷

In the block copolymer melt mesophases are stabilized by competition between the interfacial and conformational contributions to the free energy of the chains. The former arises from the contact interaction between chemically dissimilar segments and drives the system to minimize the interfacial area of the morphology; the latter is entropic in origin and drives the blocks to adopt random coil conformations. The degree of segregation is controlled by χN , where χ is the Flory-Huggins interaction parameter (see Sec. 1.2) and N is the number of monomers. From the classic work of Leibler,⁸ the mean-field order-disorder transition for symmetric diblock copolymers occurs for weak segregation at $(\chi N)_{\text{ODT}} = 10.5$.

The knowledge of polymer crystallisation and the resulting morphology is a key to understand many aspects of polymer ordering and self-assembly. The chain folding that usually accompanies polymer crystallisation^{9,10} depends strongly on the kinetic pathways of the process. Recent progress in understanding polymer crystallisation using advanced techniques indicates pre-ordering occurring in the early stages of the process. Though the exact nature of these effects is still a matter of considerable debate¹⁰⁻¹² some form of consensus has evolved about the existence of local ordering of the polymer chains as a basis for the formation of a nucleus. In addition computer simulations have also strongly challenged some of the accepted textbook ideas about the onset of crystallisation.^{13,14} In this context the application of external ‘fields’ exerted by pressure, shear flow or well-defined boundary conditions, provides a means to influence and possibly to control the pathways to

nucleation and chain folding. In the case of diblock copolymers with one semicrystalline block, a specific situation occurs of confined crystallisation within the microphase-separated morphology. Interestingly in such a system equilibrium chain folding can be achieved.²⁻⁴ A structure of alternating amorphous and crystalline layers has been predicted, the latter with regular chain folding with chain stems perpendicular to the interface. The alternative situation of extended crystallised chains cannot be an equilibrium situation (as is the case for homopolymers), as it would lead to strongly increased entropy due to the necessary accompanying stretching of the chains of the amorphous block. In spite of the extensive bulk work, far less is known about confined crystallisation of a semi-crystalline block in thin films. Evidently in the lamellar morphology thin block copolymer films provide a precise control of the boundary conditions over macroscopic areas.

Bulk investigations of diblock copolymer systems with one crystallisable block are numerous and have been reviewed.¹⁵ Depending on T_{ODT} , the crystallisation temperature T_{cr} of the crystallisable block, and the glass transition temperature T_g of the amorphous block, the confinement can be hard ($T_{cr} < T_g < T_{ODT}$) or soft ($T_g < T_{cr} < T_{ODT}$). The type of morphology determines whether the confinement is one-, two-, or three-dimensional, respectively.^{5,6} However, because of the covalent connection between the amorphous and the crystalline block, the confinement is not simply geometrical. Both theory and experiment indicate that the molecular chains are highly stretched in the ordered phase well below T_{ODT} , creating a low-entropy molten state.^{16,17} This can be expected to influence the nucleation process and thus the crystallisation kinetics. Furthermore, when T_{cr} and T_{ODT} are of the same order of magnitude, coupling and competition can occur between the crystallisation and the microphase separation process.

In the present context recent work involving PEO is of special interest. Crystallisation in a series of PEO-*b*-PBO (polybutyleneoxide) and PEO-*b*-PPO (polypropyleneoxide) was studied by Ryan and co-workers.¹⁸⁻²¹ Cheng and co-workers⁵ investigated the PEO-*b*-PS (polystyrene) system. In that case the PEO crystallisation from a microphase separated melt takes place between hard glassy PS boundaries. Depending on the morphology this can lead to a 'breaking out' of the crystalline structure from the original morphology, which is destroyed. Lamellar diblock copolymers consisting of an amorphous hydrogenated polybutadiene block and a crystallisable polyethyleneoxide block, indicated as BE or PB_n-*b*-PEO, have been studied as model systems for confined crystallisation.²² In thin films of

$B_{3700}E_{4300}$ with an approximately symmetric composition (E volume fraction 47%) the lamellae orient parallel to the substrate, which results in many orders of Bragg peaks in x-ray reflectivity measurements.²³ The slightly more asymmetric diblock $B_{3700}E_{2900}$ (E volume fraction 37%) revealed a rather different bulk and surface behaviour.^{24,25} In particular in thin films for specific supercooling a unique structure of crystalline lamellae perpendicular to the substrate was found.

In this chapter we focus on the morphology of BE block copolymers with different volume fractions and molecular weights in the molten and crystalline state. In Sec. 3.4 we compare – both for bulk and thin films – the approximately symmetric compound $B_{3700}E_{4300}$ with $B_{1270}E_{1450}$ that has similar relative volume fraction but a much lower molecular weight. This brings the ODT relatively close to the melting point of the PEO block. In Sec. 3.5 we consider the differences with the slightly asymmetric situation of $B_{3700}E_{2900}$. These results are preceded by a summary of the background of diblock microphase separation in Sec. 3.2 and of the experimental aspects in Sec. 3.3.

3.2 Block copolymer microphase separation

As preparation for the discussion in the subsequent sections, we give in this part a summary of the phase behaviour of diblock copolymers, following largely the review of Bates and Fredrickson.²⁶ Microphase separation in AB diblock copolymers is driven by chemical incompatibilities between the different A and B blocks. Unlike binary mixtures of low molecular weight compounds, the entropy of mixing per unit volume of dissimilar polymers is small and varies inversely with molecular mass. As a result, even small differences between the two polymers A and B can produce excess free energy contributions leading to demixing. The crucial element of block copolymers is that the chemical linkage between the blocks prevents demixing on a macroscopic scale. The non-ideal part of the mixing free energy is described in terms of the Flory-Huggins interaction parameter χ_{AB} , which gives the free-energy penalty to put monomer A from an A-environment into a B-environment:

$$\chi_{AB} = \frac{Z}{k_B T} [\epsilon_{AB} - \frac{1}{2}(\epsilon_{AA} + \epsilon_{BB})] \quad (3.1)$$

A positive χ_{AB} indicates net repulsion between species A and B, whereas a negative value indicates a free energy drive towards mixing. Typically, χ_{AB} is positive and small compare to unity. As χ_{AB} varies inversely with temperature, mixing is promoted as the temperature rises. On another hand, in a block copolymer melt the thermodynamic forces driving microphase separation are counterbalanced by entropy forces (chain elasticity), needed to retain uniform density in a microphase separated structure. For a block of N monomers extended to a distance R , in the harmonic approximation the elastic free energy can be expressed as $F_{\text{elas}} = 3k_{\text{B}}TR^2/(2Na^2)$, in which a is a monomer dimension. Overall, the competing free-energy contributions of interaction energy and elastic energy determine the phase behaviour of a block copolymer of a given composition and molecular mass.

To illustrate the essential physics of microphase separation, we consider the case of a symmetric diblock copolymer of about equal volume fractions f of the A and B blocks, which self-assembles into a lamellar phase. At low temperatures the segregation is strong, leading to microdomains from nearly pure A and B, separated by interfaces that are much narrower than the lamellar domain period L . The chains will be stretched up to $R = L/2$. Assuming that the stretching is uniform we can write for the free energy of the lamellar phase:

$$F_{\text{lam}} = \frac{3k_{\text{B}}TL^2}{8Na^2} + \gamma_{\text{AB}}\sigma. \quad (3.2)$$

The first term is the stretching energy; the second term is expressed as a product of the AB interfacial tension, $\gamma_{\text{AB}} = (k_{\text{B}}T/a^2)\sqrt{\chi_{\text{AB}}/6}$, and the interfacial area per chain, $\sigma = 2Na^3/L$. It describes interactions confined to the narrow interfacial region between A and B microdomains. Minimization of the expression for F_{lam} with respect to L leads to:

$$L = 1.03a\chi_{\text{AB}}^{1/6}N^{2/3} \quad (3.3)$$

and

$$F_{\text{lam}} = 1.19(\chi_{\text{AB}}N)^{1/3} \quad (3.4)$$

Note that the lamellar period scales as $N^{2/3}$. Using Eq. 3.4 we can locate the order-disorder phase boundary. In the disordered phase, the A and B blocks are homogeneously mixed.

The free energy per chain can then be approximated by the AB contact energy alone: $F_{\text{disorder}}/(k_B T) = \chi_{AB} f_A f_B N = (\chi_{AB} N)/4$. Equating F_{lam} to F_{disorder} leads to $(\chi_{AB} N)_{\text{ODT}} = 10.4$ as the location of the order-disorder transition. This result is remarkably close to the mean-field value of 10.5 obtained by Leibler.⁸ Some earlier theoretical work in this field was done by Helfand and Noolandi.²⁷ More elaborate theories have been developed by Semenov²⁸ for the strong segregation limit $\chi_{AB} N \rightarrow \infty$, and by Matsen and Schick.²⁹ Thus, symmetric diblock copolymers of high molecular mass or with strongly incompatible blocks ($\chi_{AB} N > 10.5$) are predicted to be microphase separated into lamellae, whereas smaller copolymers or more compatible blocks ($\chi_{AB} N < 10.5$) should show no microphase separation.

So far we have restricted the discussion to a mean-field picture. However, above T_{ODT} nonlinear effects of composition fluctuations appear and a weak stretching of the chains is observed. Quite generally such thermally induced composition fluctuation can suppress the critical point and produce a weak first-order transition. Hence as a consequence of the connectivity of the blocks, symmetric or near-symmetric diblock copolymers are expected to exhibit a first-order transition rather than critical behaviour. As the ODT is approached from the high-temperature side, composition fluctuations grow as the respective blocks mix into the opposite phase, and the junctions between blocks delocalize from the interphase region. Frederickson and Helfand incorporated this fluctuation behaviour in the theory.³⁰⁻³² As a result the mean-field prediction for symmetric diblock copolymers is modified to $(\chi_{AB} N)_{\text{ODT}} \approx 10.5 + 41N^{-1/3}$.

The theoretical mean-field phase diagram for AB diblock copolymers has been given in Figure 1.3 together with a comparison to the experimental phase diagram for poly(isoprene-*b*-styrene). As illustrated, the volume fraction controls which ordered structures are accessible at temperatures below the ODT. Depending on the degree of incompatibility $\chi_{AB} N$, several regimes have been identified. In the weak segregation limit corresponding to $\chi_{AB} N \geq 10.5$ the composition profile is essentially sinusoidal. In the strong segregation regime, effectively pure A and B domains are separated by a narrow interphase region. From Figure 1.3a we note that apart from the disordered melt five thermodynamically stable microphase separated structures are predicted. The lamellar phase is stable for nearly symmetric diblocks, while for intermediate levels of compositional asymmetry a hexagonally packed cylinder phase is found. In this phase the longer A blocks reside on the

convex side of the AB interface, which allows a larger configurational entropy (or reduces the elastic energy). A further increase of the compositional asymmetry leads to a body-centered cubic phase, close-packed spheres and a complex periodic bicontinuous (gyroid) phase. The experimental phase diagram (Figure 1.3b) shows similarity with the overall topology of the predicted phase diagram, with a few exceptions. In particular an overall asymmetry is observed that can be attributed to conformational asymmetry (different sizes and shapes of the monomers) not incorporated in the present theory. Secondly, the experimental phase diagram contains a small region of a second complex phase, the perforated lamellae (PL). The PL phase is considered to be thermodynamically not stable, but to be a rather long-lived transient structure with epitaxial relations to the cylindrical and lamellar phases.³³ However, this is to some extent still a matter of dispute. The identification of this phase will be discussed in Sec. 3.5. A final discrepancy between Figures 1.3a and 1.3b concerns the region of the phase diagram near the ODT. In the experimental diagram clearly direct transitions between the disordered phase and the various ordered phases are present. In contrast, the theory predicts all order-order lines to converge to a single critical point at $\chi_{AB}N = 10.5$ and $f_A = 1/2$. This discrepancy is due to composition fluctuations that become important near the weakly first-order ODT, particularly for symmetric melts.

Finally we come to the nature of the x-ray scattering around the ODT. In the mean-field approximation the structure factor for the melt of a diblock copolymer AB is given by⁸

$$NS^{-1}(q) = F(x, f) - 2\chi N, \quad (3.5)$$

where $x = (qR_G)^2$. According to Eq. 3.1 $\chi \sim 1/T$, but χ is independent of molecular mass and composition. As $F(x, f)$ does not contain χ it is independent of temperature. Hence plotting $S^{-1}(q)$ against reciprocal absolute temperature T^{-1} should give a linear relation. Going beyond mean-field theory Eq. 3.5 should be expanded to³⁰

$$NS^{-1}(q) = F(x, f) - 2\chi N + cN^{-1/3}, \quad (3.6)$$

where c is a constant. At the lamellar ODT $c \approx 90$. Upon introducing fluctuations the scattering curve retains its shape and the position of the maximum at q^* . As the last term in

Eq. 3.6 is independent of q , only the peak height will be affected. At high temperatures in the disordered phase the inverse intensity determined by $S^{-1}(q)$ decreases linearly with T^{-1} following the mean field result, Eq. 3.5. As the ODT is approached, composition fluctuations become more important and show up in a plot of $S^{-1}(q)$ as a function of T^{-1} as pronounced deviation from linearity.³⁴

3.3 Experimental

3.3.1 Materials

We used poly(butadiene-*b*-ethyleneoxide) diblock copolymers differing in molecular mass and volume fraction, which are summarised in Table 3.1. The samples B₃₇₀₀E₄₃₀₀ and B₃₇₀₀E₂₉₀₀ were obtained from Goldschmidt AG (Germany) and B₁₂₇₀E₁₄₅₀ from Polymer Source Inc (Canada). Synthesis was done by sequential anionic polymerization of ethylene oxide and butadiene (about equal amounts of 1,2 and 1,4 units, statistically distributed). The

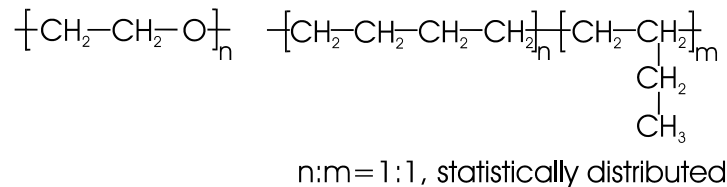


Figure 3.1. Chemical structures of a PB_n-*b*-PEO block copolymer with poly(ethylene oxide) and hydrogenated polybutadiene.

resulting copolymer consists of an OH-terminated PEO-block and a hydrogenated polybutadiene block (PB_n) (see Figure 3.1). The melting point for B₃₇₀₀E_x is about 57°C and for B₁₂₇₀E₁₄₅₀ about 47°C. Prior to use the polymers were dried under vacuum at 80°C to remove any residual solvent. The molecular volume V_{mol} of each of the blocks was calculated using $V_{mol} = M_n / (\rho N_A)$, in which N_A is Avogadro's number and ρ the density of the particular block. Then the volume fraction PEO simply follows from $f_E = V_{mol}^E / (V_{mol}^E + V_{mol}^B)$. We used for the density of the PEO and PB_n blocks values of 1.13 g/cm³ and 0.86 g/cm³, respectively.²³ Upon crystallisation the density ρ_{PEO} changes to

about 1.23 g/cm³. Note that B₃₇₀₀E₂₉₀₀ and B₁₂₇₀E₁₄₅₀ have effectively the same volume fractions but that B₁₂₇₀E₁₄₅₀ has a much smaller molecular mass. As we shall see this brings the ODT within experimental reach for B₁₂₇₀E₁₄₅₀.

Table 3.1 Molecular characteristics of BE diblock copolymers in the melt.

Sample	B ₃₇₀₀ E ₄₃₀₀		B ₁₂₇₀ E ₁₄₅₀		B ₃₇₀₀ E ₂₉₀₀	
	PEO	PB _n	PEO	PB _n	PEO	PB _n
M _n (g/mol)	4300	3700	1450	1270	2900	3700
Number of monomers N	98	66	33	23	66	66
Volume fraction f	0.47	0.53	0.45	0.55	0.37	0.63
Radius of gyration $R_G = a\sqrt{N/6}$ (nm)	1.1	1.3	0.65	0.69	0.93	1.28
Length of nonfolded block (nm)	27.4	25.4	9.2	8.7	18.5	25.4
Polydispersity	1.02		1.09		1.1	

3.3.2 Experimental methods

Small-angle and wide-angle x-ray scattering (SAXS/WAXS). Simultaneous SAXS and WAXS measurements were performed using an in-house set-up with a rotating anode x-ray generator (Rigaku RU-H300, 18 kW). A monochromatic beam (CuK_α-line, wavelength $\lambda = 0.154$ nm) with a divergence about 0.012° was acquired using two parabolic multilayer mirrors (Bruker, Karlsruhe, Germany). The SAXS and WAXS intensities were recorded by a two-dimensional detector (Bruker Hi-Star) and a linear one (PSD-50M, M. Braun), respectively. The collected data were azimuthally integrated and corrected for the geometry of the scattering entities ('Lorentz correction'). Graphically the relative intensity is presented vs $q = (4\pi/\lambda)\sin\theta$, where q is the modulus of the wave vector transfer and 2θ is the scattering angle. A Linkam CSS450 temperature-controlled shear system was used as sample holder.

X-ray reflectivity. X-ray reflectivity measurements were carried out using a two-circle diffractometer attached to the same rotating anode generator. The incident beam was

monochromatized to $\lambda = 0.154$ nm and collimated to a divergence of about 0.025° in the horizontal scattering plane (xz-plane with the z-axis along the film normal) by a W/B₄C graded parabolic multilayer mirror (Osmic, Auburn Hills, USA). Additional pre-sample and pre-detector slits lead to an overall in-plane resolution given by $\Delta q_z = 0.043$ nm⁻¹ and $\Delta q_x = 5 \times 10^{-3} q_z$.

In reciprocal space specular reflectivity scans probe the scattered intensity along q_z . The x-ray intensity was corrected for sample size effects at small incidence angles as well as for background scattering; the incident intensity was normalized to unity. The data was analysed by an iterative matrix formalism derived from the Fresnel equations, using the REFLAN software package (see Sec. 2.3.1) The calculated reflectivity profiles were convoluted with the experimental resolution, assumed to be of Gaussian statistics

Optical microscopy. A Leitz Orthoplan microscope equipped with a Linkam THMS600 hot stage was used to examine thin film surfaces. All images were taken in the reflection mode using a white light source in order to obtain interference colours. The samples were kept in a dry nitrogen atmosphere.

Atomic force microscopy (AFM). Height and phase images of the crystalline morphology of the diblock copolymers were taken using a Solver AFM from NT-MDT (Zelenograd, RF) at ambient conditions in the tapping mode. A vibrating cantilever with a resonant frequency of about 300 kHz and a silicon tip with a radius of curvature less than 10 nm were used. To examine the bulk crystalline morphology by AFM the crystallized samples were quenched in liquid nitrogen and cut. As discussed earlier⁷ in this way surfaces smooth enough for AFM imaging can be obtained that reflect the bulk morphology.

Transmission electron microscopy (TEM). TEM measurements were carried out by P.M. Frederik and P.H.H. Bomans at the Department of Pathology, Electron Microscopy, University of Limburg, Maastricht, using a CM12 microscope (Philips, Eindhoven, The Netherlands). Cryo-sections were obtained from bulk BE36 and observed at low temperatures in the electron microscope using low-dose conditions for imaging. A small part of the sample (less than a cubic mm) was mounted on a silver pin, frozen by dropping into liquid nitrogen and mounted in a Leica Ultracut S (Vienna, Austria) equipped with an FCS attachment for low temperature sectioning. At -70°C thin sections were cut on a 'dry' diamond knife. Smooth sections were collected with a dry eye-lash probe and pressed by hand onto the carbon coated formvar supporting film of a specimen grid. The grids were

transferred to the cryo-holder (Gatan 626, Pleasanton, Ca USA) of the microscope using the cryo-transfer station. During observation and imaging the temperature was kept at -170°C to minimize beam damage.

3.3.3 *Samples preparation and measurement procedure*

For SAXS the polymer was put between two pieces of a kapton foil separated by a metal ring fixing the thickness to about 0.5 mm and put in the sample holder. In order to probe the polymer morphology in the melt we initially kept the sample at 90°C for 10 min and then cooled it down to 40°C . Subsequently we increased the temperature and took SAXS scans at various temperatures up to 300°C . To study bulk crystallisation again each sample was kept at 90°C for 10 min and then cooled to the crystallisation temperature T_{cr} at about $10^{\circ}\text{C}/\text{min}$. The SAXS and WAXS signals were monitored simultaneously in order to track the crystallisation process. The measurements were done in a dry nitrogen atmosphere and no degradation effects were observed during the annealing at 90°C .

Thin films were prepared by spincoating low-concentration solutions of diblock copolymer in dichloromethane (DCM) on a silicon wafer at 2000 rpm. The wafers were first cleaned in chromic acid for about 10 min and then rinsed in ultra-pure water. During x-ray reflectivity measurements the sample was kept in a two-stage oven regulated within 0.1°C by a Eurotherm controller and evacuated to $\sim 10^2$ Pa. The films were annealed at $T_{\text{ann}} = 90^{\circ}\text{C}$ and then cooled down to T_{cr} at about $10^{\circ}\text{C}/\text{min}$.

3.4 **Symmetric PB_n-b-PEO systems**

3.4.1 *Microphase separation*

First we present experimental results concerning the phase-separated morphology of the symmetric diblock copolymers B₃₇₀₀E₄₃₀₀ and B₁₂₇₀E₁₄₅₀ in the bulk melt. Figure 3.2a shows an overview of the SAXS patterns for B₃₇₀₀E₄₃₀₀. For temperatures up to 300°C the block copolymer remains phase separated, hence T_{ODT} is well above this value. Pronounced scattering peaks appear at relative positions 1:2:3, which corresponds to a lamellar phase with long period $L = 2\pi/q^*$ in which q^* is the position of the first-order scattering

maximum. The period increases from 14.7 nm around 300°C to 19.9 nm at 35°C (see Figure 3.2b).

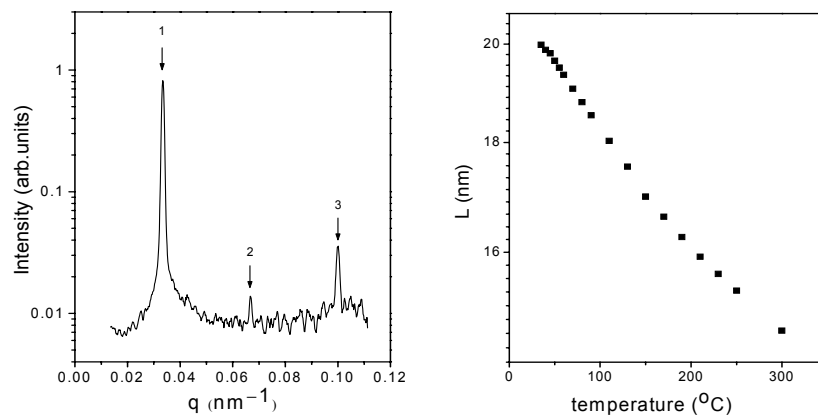


Figure 3.2. (a) SAXS profile of $B_{3700}E_{4300}$ in the melt (80°C) indicating a lamellar morphology. (b) Lamellar period L in the melt as a function of temperature.

The low-molecular-mass compound $B_{1270}E_{1450}$, with effectively the same volume fraction of the constituting blocks as $B_{3700}E_{4300}$, shows a lamellar morphology with a period changing from 8.1 nm at 100°C to 8.7 nm at 50°C (see Figure 3.3b). At temperatures around 110°C , $B_{1270}E_{1450}$ shows a distinct decrease of the intensity of the first-order reflection (see Figure 3.3a). This process is accompanied by a change in the line profile from Gaussian to Lorentzian (and in the accompanying FWHM) as well as a discontinuity in the peak position (lamellar period). The results are summarized in Figure 3.4. The pronounced discontinuities indicate the order-disorder transition from the microphase separated structure to a disordered state. The peak at q^* below T_{ODT} is the first-order Bragg reflection of the periodic lamellar structure and shows no discontinuity in its position. The width of the Lorentzian above the ODT corresponds to a correlation length of about 10 nm. Note that this value is rather constant; it is the intensity that decreases upon further heating.

As discussed in Sec. 1.2, for BE block copolymers the PEO block preferentially segregates on the substrate while PB_b part prefers to be exposed to the air. This situation corresponds to the antisymmetric case depicted in Figure 1.4. Figure 3.5 shows the typical resulting terrace structure formed when the film thickness does not conform to an integer or

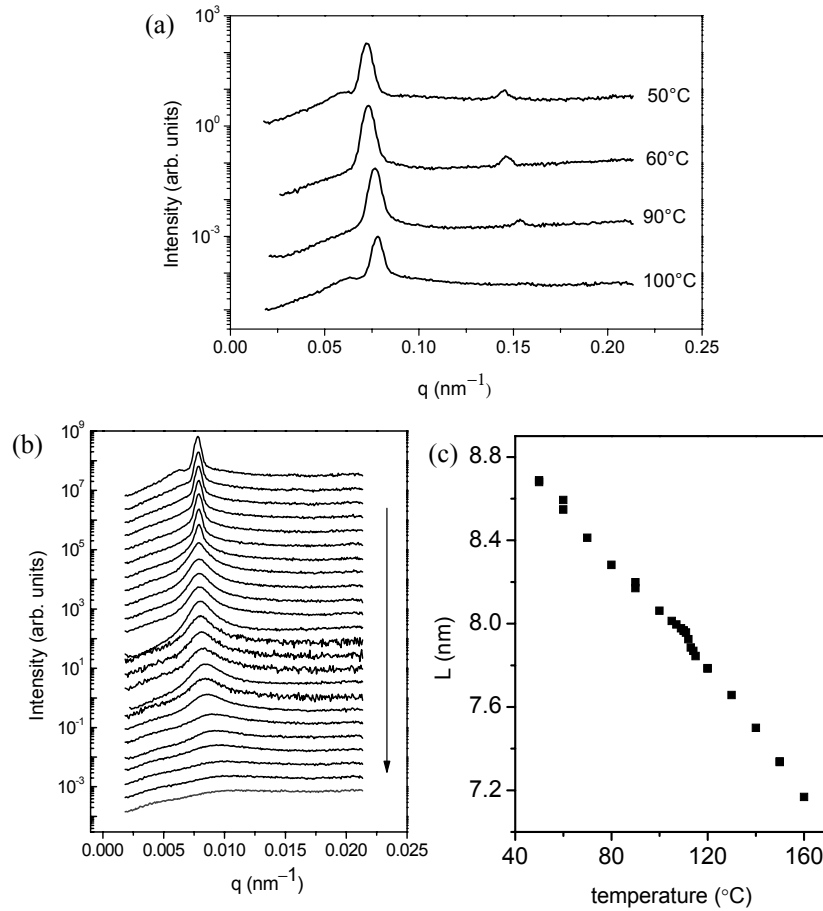


Figure 3.3. SAXS profiles from the phase separated lamellar melt of $B_{1270}E_{1450}$ (a) Low temperature data. (b) At various temperatures around the ODT (from top to bottom: 100-115 (1°C steps), 120-160 and 190-250 (10°C steps). The curves are shifted for clarity. (c) Periodicity L of the lamellar phase as a function of temperature.

half integer number parallel layers. The different grey scales indicate several distinct levels on the surface that differ in height by a full block period. A typical x-ray reflectivity curve from a lamellar $B_{1270}E_{1450}$ film is presented in Figure 3.6. The curve refers to a 9.5 layer film at $T=90^\circ\text{C}$ in the molten phase-separated state. Besides the Kiessig fringes indicating the film thickness, several orders of Bragg peaks are visible. Hence we can conclude the

presence of a lamellar ordering of alternating layers of PEO and PB_n oriented parallel to the substrate.

Figure 3.7 summarizes experimental data for the temperature dependence of the lamellar period L comparing thin films and the bulk. For B₃₇₀₀E₄₃₀₀ the period in the film shows a slight tendency to exceed the bulk values (about 5%). We ascribe this difference to a systematic error. This is corroborated by the results for B₁₂₇₀E₁₄₅₀ that show no influence of the thin film geometry on the lamellar spacing. We conclude that for film thickness studied (of the order of several lamellar periods) the surface field has an orientational effect on the layers, but does not result in frustration of the lamellar spacing.

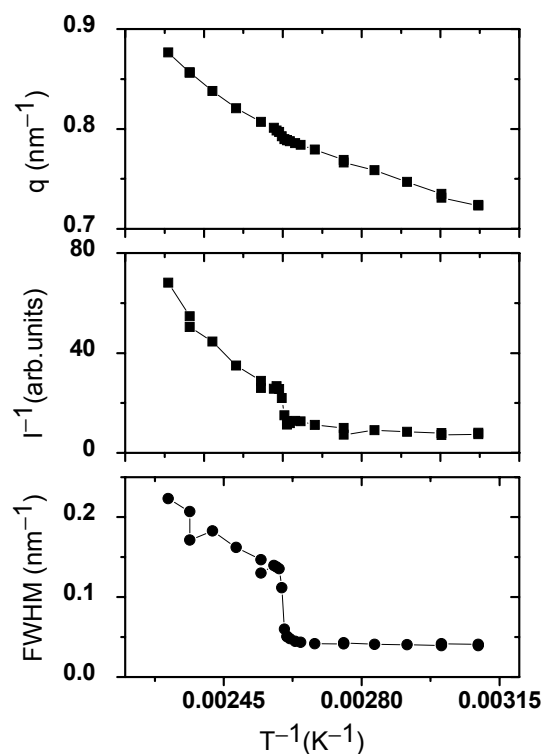


Figure 3.4. Temperature dependence of the position (q), the reciprocal intensity (I^{-1}) and the FWHM of the first-order reflection from B₁₂₇₀E₁₄₅₀.

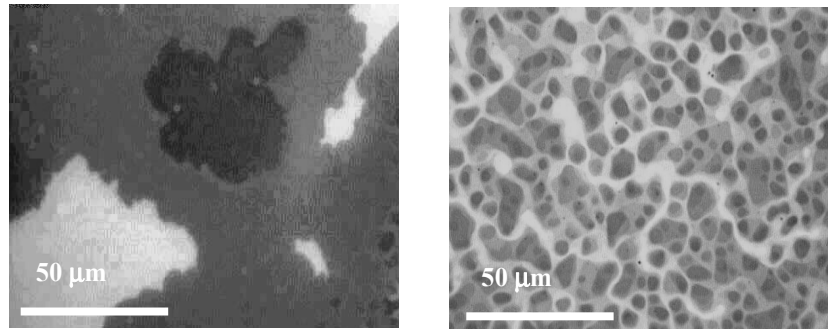


Figure 3.5. *Optical microscopy image of the surface topography of spin-coated $B_{3700}E_{4300}$ (left) and $B_{1270}E_{1450}$ (right) films with a thickness of 122 and 70 nm, respectively. Melt at $T = 90^\circ\text{C}$.*

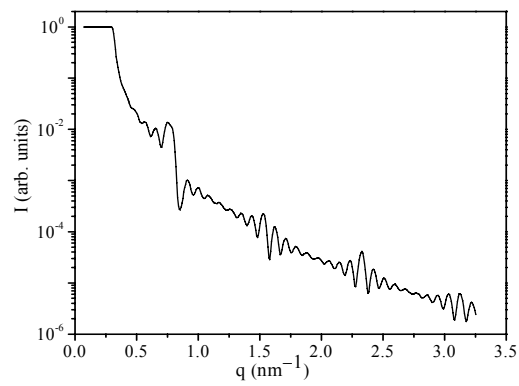


Figure 3.6. *X-ray reflectivity curve indicating a lamellar morphology in the melt of a 78 nm thick $B_{1270}E_{1450}$ film at 90°C .*

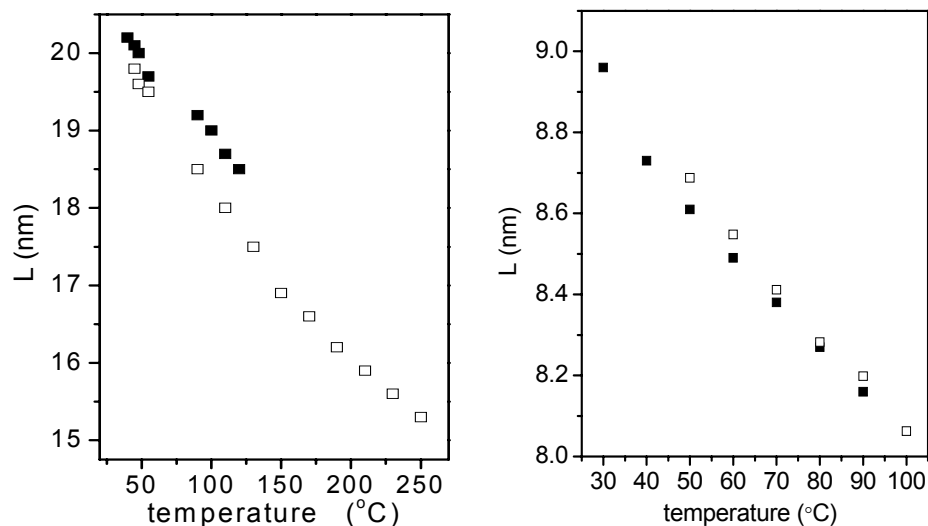


Figure 3.7. Temperature dependence of L in melt of $B_{3700}E_{4300}$ (left) and $B_{1270}E_{1450}$ (right). Filled and open squares indicate thin film and bulk data, respectively.

3.4.2 Crystallisation of the PEO block

The isothermal crystallisation and morphology of $B_{3700}E_{4300}$ indicates a continuous increase of the long period (from 20 to 50%) with increasing crystallisation temperature (see Figure 3.8a).³⁵ This necessarily implies noninteger-folded crystals. SAXS profiles following the crystallisation of $B_{1270}E_{1450}$ at different crystallisation temperatures are shown in Figure 3.8b. All samples were annealed for at least 5 min above T_{ODT} and show a lamellar morphology in the melt. Upon crystallisation, mixed SAXS patterns appear that can be interpreted as coexistent crystalline and amorphous parts. The amorphous peaks disappear with time. A common feature of all crystallised samples – regardless of crystallisation temperature – is a broad first- and third-order crystalline peak. The $B_{1270}E_{1450}$ sample as crystallised at 26°C gives four reflections, typical for a lamellar morphology with a ratio of peak positions 1:2:3:4. The period of the lamellar layers is $L = 15.14$ nm, as determined from the first-order maximum at $q^* = 0.415$ nm⁻¹. At $T_{cr} = 30^\circ\text{C}$ the same period is obtained, but the induction time of the crystallisation process is an hour longer than at 26°C. At 35°C

$B_{1270}E_{1450}$ needs several hours to start the crystallisation process and few days to crystallise completely, as judged from the disappearance of the first-order peak from the melt. The resulting peak now indicates $L = 16.8$ nm. In Figure 3.8c the lamellar periods are compared for the crystalline state and the melt.

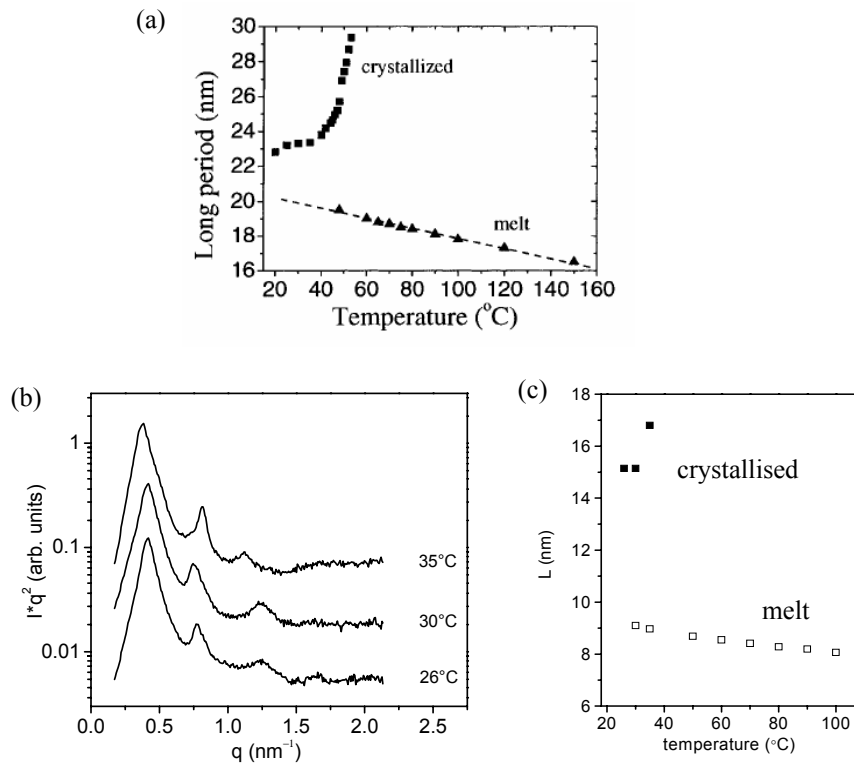


Figure 3.8. (a) Lamellar periodicity of $B_{3700}E_{4300}$ crystallised and in the melt.³⁵ (b) SAXS profiles of $B_{1270}E_{1450}$ crystallised at various temperatures. (c) Lamellar periodicity of $B_{1270}E_{1450}$ crystallised and in the melt.

The thin film behaviour of PEO crystallisation in lamellar BE films has been reviewed by De Jeu.²² For $B_{3700}E_{4300}$ the lamellar period has been reported to increase upon crystallisation²³ in spite of the decreasing volume (increasing density) of PEO. This expansion is needed to fit the thickness of the PEO sublayer to specific discrete values (see Figure 3.9), that were found to correspond to an integer (or half-integer) number of stems.²³ Density conservation forces the PB block to follow this stretching. As a consequence a

lateral contraction results through the whole film resulting in macroscopic pits and cracks. A microscopic picture of this effect is shown in Figure 10a; Figure 10b indicates a similar behaviour for $B_{1270}E_{1450}$.

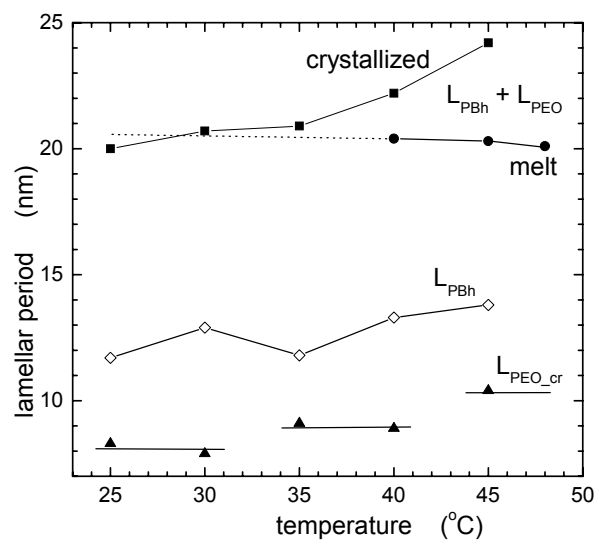


Fig. 3.9. Lamellar period L and sublayer thicknesses at various temperatures as determined by fitting the x -ray reflectivity of a $B_{3700}E_{4300}$ film, indicating discrete values $L_{PEO,cr}$ for the crystallised sublayer.²³

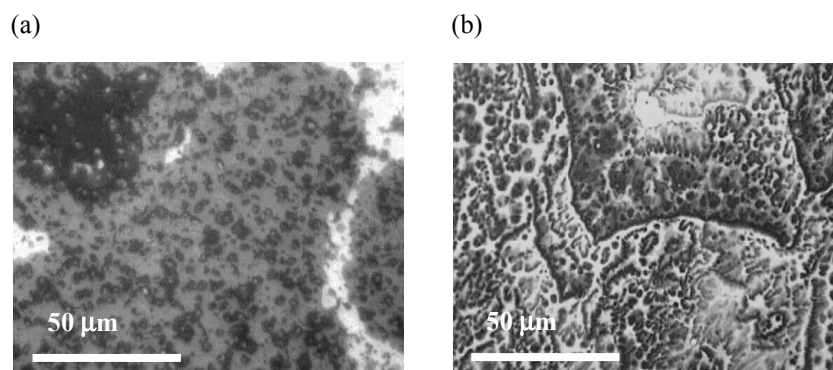


Figure 3.10. Optical microscopy image of the surface topography of a crystallised (a) $B_{3700}E_{4300}$ and (b) $B_{1270}E_{1450}$ at $T = 30^\circ\text{C}$.

Figure 3.11 shows an x-ray reflectivity curve from crystallised $B_{1270}E_{1450}$ at 30°C with $L = 14.6$ nm ($q = 0.86$ nm⁻¹), which is about 4% less compared to the bulk at the same temperature. The roughening of the surface due to the crystallisation smears the Kiessig fringes and obstructs a direct determination of the film thickness. Data from the same sample in the melt (Figure 3.6) indicates that the film consists of 9.5 layers, which gives an estimate of 139 nm for the film thickness in the crystalline state.

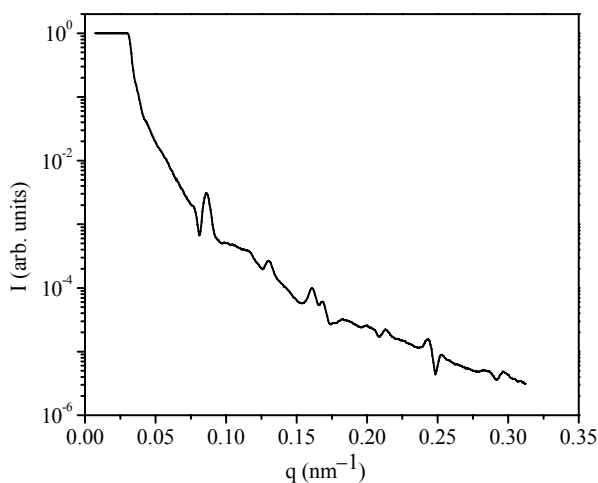


Figure 3.11. X-ray reflectivity curve of a crystallised $B_{1270}E_{1450}$ film.

3.4.3 Discussion

Diblock copolymers of the type PEO-*b*-P(alkane), where alkane stand for ethylene (PE), ethylethylene (PEE), ethylpropylene (PEP) and butadiene (PB), were synthesized by Hillmeyer and Bates.³⁶ The phase behaviour of PEE was described in some detail by Hadjuk et al.³⁷ Evidently our PB_h is closely related to PEE, moreover the PEE was reported to contain 10% PE.³⁶ In our situation that is around 50% (compare Fig. 3.1). Hence we shall use some of the PEO-*b*-PEE data for a semi-quantitative analysis of our samples, in particular the reported value $\chi \approx 1$ at 100°C. The phase diagram of PEE shows a lamellar phase for $f_{\text{PEO}} > 0.48$ and an hexagonal phase for $f_{\text{PEO}} < 0.39$. For three fractions in the intermediate region (f_{PEO} -values of 0.42, 0.44 and 0.46) mixed reflections were found upon

melting the PEO crystals, indicating coexistence of the two phases. Upon further heating they give way to reflections corresponding to a stable gyroid phase. Our materials with $f_{\text{PEO}} = 0.46 - 0.47$ would be in this region if the results were directly applicable. However, we did not find any evidence of a gyroid phase. In that case from the PEO-*b*-PEE data the transition hexagonal-lamellar would be expected around $f_{\text{PEO}} = 0.42$. This is well below the f_{PEO} -values of our lamellar materials.

Let us now discuss some aspects of the ODT and the temperature dependence of the lamellar period as observed for $\text{B}_{3700}\text{E}_{4300}$ and $\text{B}_{1270}\text{E}_{1450}$. First we note that for the latter compound with $M_n = 2720$ we find $T_{\text{ODT}} = 383$ K. Following $(\chi N)_{\text{ODT}} \approx 10.5$ we can estimate for $\text{B}_{3700}\text{E}_{4300}$ that the T_{ODT} should be a factor of the order $8000/2720 = 2.9$ larger. This is indeed well above our measurement limit of 300°C . The SAXS patterns of $\text{B}_{3700}\text{E}_{4300}$ in Figure 3.2 show three orders of x-ray peaks, with the third order relatively strong. The first peak corresponds to lamellar spacing $L = 2\pi/q^*$. In contrast, Figure 3.3 of $\text{B}_{1270}\text{E}_{1450}$ gives only a weak second-order peak. As could be anticipated for the low molar mass of the latter compound, the interfaces are no longer sharp and the density distribution normal to the layers is close to a sinusoidal. From the scaling relation Eq. 3.3 the ratio of the lamellar periods of the two compounds should be of the order of $2.9^{2/3} = 2.03$; experimentally we observed at 40°C a value $20/8.8 = 2.3$. As the temperature decreases, the lamellar period increases due to the temperature dependence $\chi \sim 1/T$ (compare Eq. 3.3). The conformational entropy of chains decreases leading to an increase of the end-to-end distance. As a result considerable stretching occurs upon cooling. The unstretched period can be estimated from the radius of gyration to be 9.6 nm and 5.4 nm for $\text{B}_{3700}\text{E}_{4300}$ and $\text{B}_{1270}\text{E}_{1450}$, respectively. At 50°C the observed value for $\text{B}_{3700}\text{E}_{4300}$ is $L = 19.6$ nm which indicates an elongation of about a factor of 2. The corresponding value for $\text{B}_{1270}\text{E}_{1450}$ is $L = 8.6$ nm, which is slightly less. Next we come to a discussion of the results of Figure 3.4 that describe the ODT in $\text{B}_{1270}\text{E}_{1450}$. In this context small-angle x-ray scattering is an accurate method of determining the ODT. To facilitate comparison with theory, the inverse peak intensity and width are plotted against the inverse temperature. Both show a pronounced discontinuity at the transition from the disordered state to the ordered lamellar structure, in agreement with theoretical predictions of Sec. 3.2. The broad peak that persists above T_{ODT} results from density fluctuations. Repulsive interactions between the PEO and PB_h blocks drive like segments together, which process results in a finite-size stabilization of the locally ordered

clusters on the microdomain length scale. This process extends to well above the T_{ODT} and induces according to Eq. 3.6 deviations from linearity in $S^{-1}(q)$ and thus in $I^{-1}(q)$.³⁴ Upon ordering, the lineshape of the scattering peak changes from Lorentzian to Gaussian. Above the ODT, L corresponds to the spatial extent of concentration fluctuations, activated by thermal energy, whereas in the ordered state it corresponds to the spacing for the lamellar structure generated by the block segregation. From the width of the peaks we estimate directly above T_{ODT} a correlation length of of 10 nm, and directly below the ODT a finite-size of the ordered domains of 140 nm.

Subsequently we come to the effects of the crystallisation of the PEO block, which takes place in the surroundings of the phase-separated morphology. As discussed in Sec. 3.1 the resulting confinement has a strong influence on the crystallisation process. In the bulk of $B_{3700}E_{4300}$ we found a continuous variation of the lamellar spacing with supercooling, which necessarily leads to noninteger-folded crystals (Fig. 3.8a). This can be contrasted to low-molecular mass PEO homopolymers for which noninteger-folded chain crystals are metastable and only observed at the beginning of the crystallisation.³⁸ For homopolymers, thickening through sliding diffusion is easy, especially during slow heating.³⁹ Li et al.³⁵ attributed the relative stability of noninteger-folded crystals in bulk block copolymer systems to two reasons. First, due to the loss of entropy due to attendant stretching of the amorphous block, the Gibbs free-energy landscape between integer-folded chain crystals will be rather flat. This reduces the thermodynamic driving force toward integer-folded chains in comparison with homopolymers. Second, kinetically, the thickening process must overcome not only the internal fraction within the PEO crystals, but also that within the amorphous part.^{40,41}

The thin film behaviour of PEO crystallisation in lamellar BE films has been reviewed by De Jeu.²² For $B_{3700}E_{4300}$ we calculated above that before crystallisation the molecules in the lamellae are already stretched compared to a Gaussian coil by about a factor of two. At low supercooling, upon crystallisation the lamellar period increases strongly further in spite of the decreasing volume (increasing density) of PEO (Figure 3.9). This expansion is needed to fit the thickness of the PEO sublayer to an integer (or half-integer) number of stems. To determine the number of stems at the various temperatures the extended chain length of PEO is divided by the number $n = 2, 3, \dots$ and compared with the PEO sublayer thickness. For the PEO layer at the substrate this leads with decreasing temperature to $n = 5$,

6 and 7 stems, respectively. This situation is sketched in Figure 3.12. Taking for the interior PEO layers in the film the same number of folds as for the bottom layer would lead to crystalline double layers. Alternatively a ‘zipper’-model could be assumed in which stems originating from opposite interfaces pass along each other (co-crystallisation). This would double the stem length leading to 2.5, 3 and 3.5 stems. Whatever be the case, the number of folds increases when the crystallisation temperature is lowered. This indicates that for fast crystallisation, kinetic (non-equilibrium) effects dominate. Conversely one may assume that at the highest temperatures probably equilibrium chain folding has been reached.

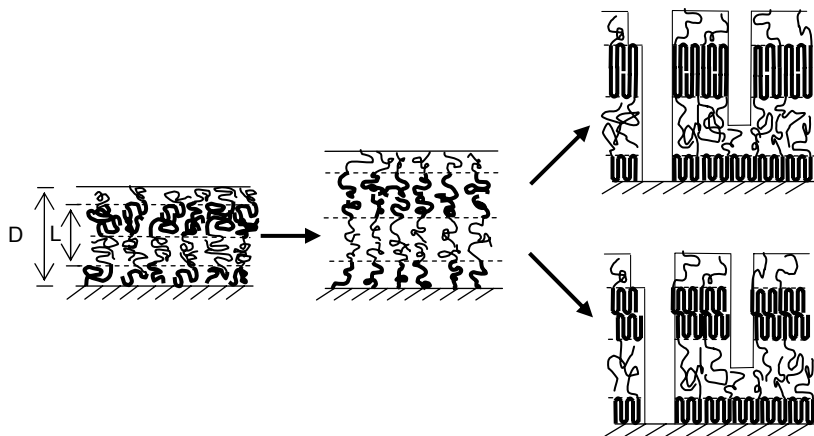


Figure 3.12. Model for the development of the layer structure and the polymer folds during crystallisation of a $B_{3700}E_{4300}$ film (from Ref. 23).

Density conservation forces the PB block to follow the stretching. Evidently the loss of entropy associated with the PB_h stretching is more than compensated for by the favourable packing of the PEO stems. As a consequence a lateral contraction results through the whole film resulting in macroscopic pits and cracks as shown in Figure 3.10. Implicit in this interpretation is that the folded PEO chains are perpendicular to the layers. The difference with the bulk SAXS results of $B_{3700}E_{4300}$ has tentatively been attributed to the two-dimensional crystallisation process in thin films, which causes the lateral sliding again to be important, similarly as in PEO homopolymers.²³

The bulk data for PEO crystallisation in B₁₂₇₀E₁₄₅₀ are limited (see Figure 3.8c). Taking the volume fraction of the PEO and the PB_h blocks into account and assuming the molecular chains to be perpendicular to the lamellae, we calculate for the PEO sublayer thicknesses of 7.0 nm and 7.7 nm for 26°C (and 30°C) and 35°C, respectively. This does not allow ascribing an integer or half-integer number of stems to the crystalline layer. Nevertheless, taking all the uncertainties into account, we speculate that the crystals at 35°C could be extended chain crystals.

For B₁₂₇₀E₁₄₅₀ films we found upon crystallisation similar cracks and pits as for B₃₇₀₀E₄₃₀₀ (Figure 3.10) suggesting similar processes. From the estimated film thickness in the crystalline state for the film of Figure 3.11 (139 nm or 9.5 layers) we calculate for PEO and PB_h a sublayer thickness of 6.7 nm and 7.9 nm, respectively. The number of crystalline stems in the crystalline PEO layer is then 1.5 or 3 (from $9.2/6.7 = 1.4$ nm), in agreement with the overall picture.

3.5 Asymmetric PB_h-PEO system

3.5.1 Ordering in bulk

In this section we consider the slightly asymmetric diblock B₃₇₀₀E₂₉₀₀ (see Table 3.1; PEO volume fraction 37%). This compound revealed a rather different bulk and surface behaviour than various related more symmetric compounds.^{24,25} In thin films optical observations gave island-hole patterns with a step height equal to the expected thickness of block lamellae parallel to the substrate. In addition for specific supercooling conditions, a unique structure of lamellae perpendicular to the substrate was found. As we shall see B₃₇₀₀E₂₉₀₀ has a composition where its morphology is just hexagonal. As a result crystallisation interacts strongly with the melt morphology.

Figure 3.13 shows SAXS patterns from the B₃₇₀₀E₂₉₀₀ melt upon heating from 40 to 300°C. At all temperatures the polymer remains phase separated, hence T_{ODT} is well above 300°C. Pronounced scattering peaks appear at relative positions $1:3^{1/2}:4^{1/2}:7^{1/2}:12^{1/2}:13^{1/2}$ as illustrated for 48°C in the top curve of Figure 3.14. This assignment (see Table 2.1) corresponds to a hexagonal lattice constant $a = 4\pi/(3^{1/2}q_{100})$ which varies from 16 nm around 300°C to 22.7 nm at 48°C (see inset Figure 3.13). Upon increasing the temperature

the intensity of some of the peaks decreases or completely vanishes, reflecting smearing of the density profile and broadening of the interfaces. Based on the values for the volume fractions,⁸ the relevant diblock copolymer morphology is assumed to consist of hexagonally packed cylinders of PEO in a matrix of the majority component PB_h. This conclusion differs from the assumption of a lamellar phase given in Ref. 25 on the basis of optical observations in films. In Ref. 22 B₃₇₀₀E₂₉₀₀ is reported to behave rather differently compared to several more symmetric lamellar BE block copolymers. This is in agreement with our assignment of a hexagonal phase on the basis of unambiguous SAXS data.

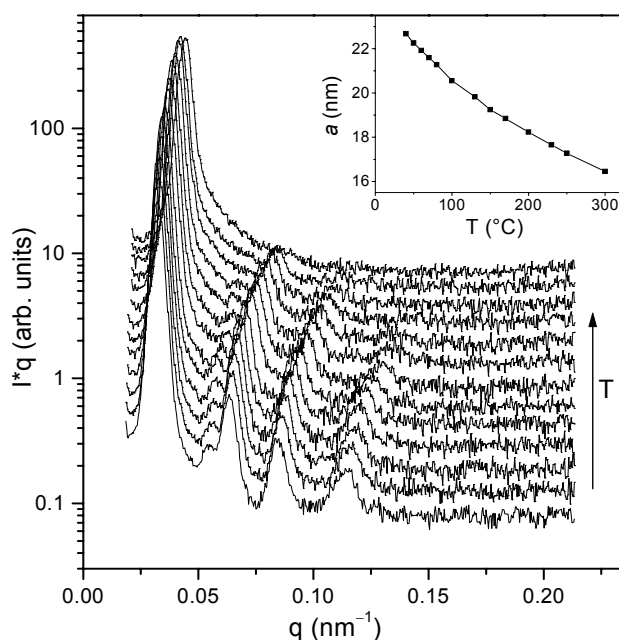


Figure 3.13. SAXS profiles of B₃₇₀₀E₂₉₀₀ in molten state at various temperatures (from bottom to top: 40-80 (with 10°C step), 100, 130, 150, 170, 200, 250, 300°C). The curves are shifted for clarity and indicate hexagonal symmetry. The inset presents the hexagonal lattice parameter $a=4\pi/(3^{1/2}q_{100})$ as a function of temperature.

Upon crystallisation the scattering profiles change considerably, see Figure 3.14. The reference curve from the melt morphology at 48°C ($a=22.7$ nm) represents also the melt at 38 and 40°C, since the difference in the intercylinder distance at these temperatures is only

a few tenth of nanometer. The sample crystallised at 38°C gives pronounced peaks at 0.29, 0.58 and 0.77 nm⁻¹. The ratio 1:4^{1/2}:7^{1/2} of their positions agrees with a hexagonally packed structure with $a = 25$ nm. Increasing T_{cr} results in similar scattering profiles. At 40°C the peaks are positioned at 0.27, 0.55 and 0.72 nm⁻¹, respectively, again at 1, 4^{1/2} and 7^{1/2} times the fundamental wave vector corresponding to $a = 26.9$ nm. The SAXS curve taken at $T_{cr} = 48^\circ\text{C}$ comprises contributions from both the crystalline morphology and the residual melt structure. On the time scale of the experiment (3 days) the first-order melt peak did not disappear fully. Reflections from the crystallised part at 0.21 and 0.56 nm⁻¹ (1:7^{1/2}) reveal hexagonal symmetry with $a = 34.5$ nm. The peak corresponding to $2q_{100}$ is probably hidden in the residual first-order molten peak.

To determine the morphology associated with the hexagonal symmetry in the crystallised B₃₇₀₀E₂₉₀₀, we performed AFM on a surface obtained by cryogenic

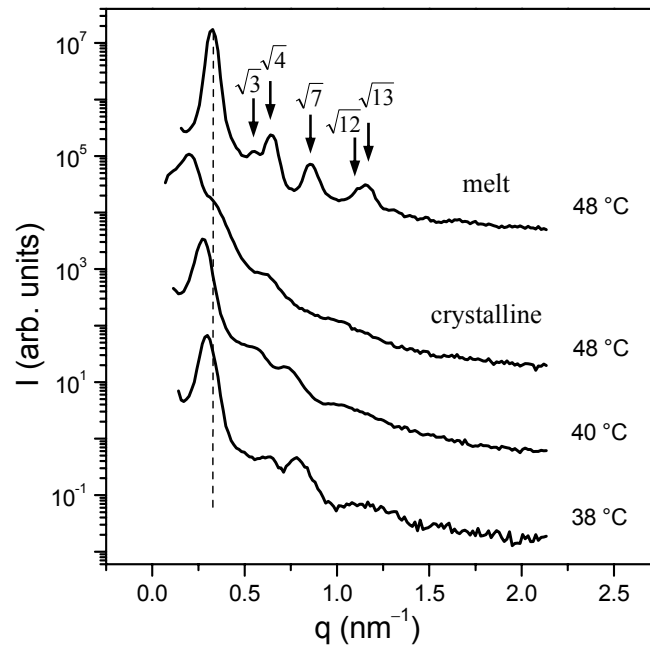


Figure 3.14. SAXS profiles of B₃₇₀₀E₂₉₀₀ crystallised at various temperatures. The melt morphology at 48 °C from Figure 3.13 is shown for comparison. The curves are shifted for clarity.

microtomography of the bulk polymer crystallised at 48°C. A typical picture presented in Figure 3.15a shows elongated structures that could in principle be lamellae or cylinders. However, in the case of cylinders we would also expect approximately hexagonal ‘head-on’

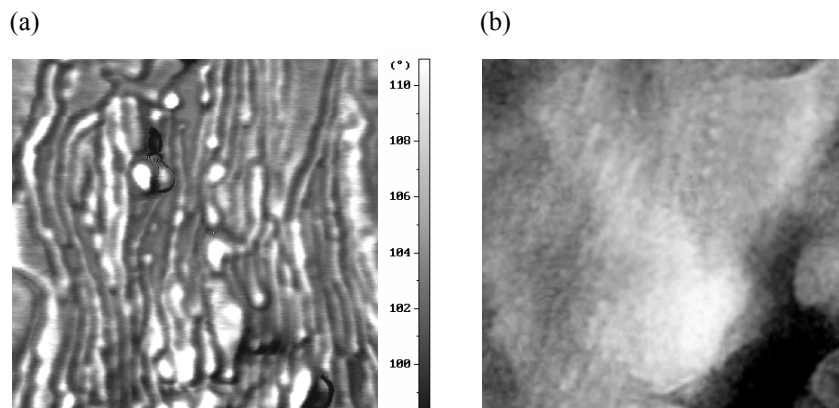


Figure 3.15. *Tapping mode AFM phase image (a) and non-stained TEM image (b) of bulk $B_{3700}E_{2900}$ crystallised at 48°C. The elongated lamellar patterns are modulated with a lateral period of 25–30 nm.*

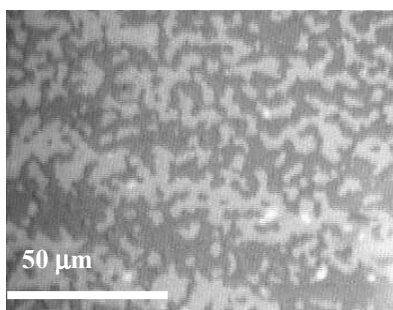


Figure 3.16. *Optical microscopy image of the surface topography of a $B_{3700}E_{2900}$ film spin-coated from 2% DCM solution (sample D). Molten state at $T=90^{\circ}\text{C}$ with terrace-like height variations.*

structures that were not observed. In addition lateral modulations are seen along the elongated structures with a period of about 25 – 30 nm, which are neither expected for cylinders nor for lamellae. Other parts of the sample show only small variations in the phase contrast and can be conceived as domains with different orientation. Supplementary TEM measurements on unstained B₃₇₀₀E₂₉₀₀ samples crystallised at 48 and 40°C (Figure 3.15b) corroborate the modulations seen in AFM. In Ref. 7 very similar modulations were seen in cryocut block copolymers, which could unambiguously be related to perforated lamellae by SAXS on an oriented sample. Analogous to these observations we interpret them here in B₃₇₀₀E₂₉₀₀ also as perforations of lamellae, characteristic of the HPL phase.

3.5.2 Ordering in thin films

To perform x-ray reflectivity measurements on thin films of B₃₇₀₀E₂₉₀₀ samples were prepared from 0.3, 0.5, 1 and 2% solutions in DCM, to be referred to as films A, B, C and D with a thickness of the order of 20, 40, 80 and 140 nm, respectively. Examination by optical microscopy indicates that in the molten state the surface is covered with terraces (see Figure 3.16). After crystallisation additional grain-like structures appear, which cause roughening of the air interface. In contrast to lamellar BE films, no crystallisation front of pits and cracks (see Figure 3.10) is observed during this process. Though the formation of terraces is typical of lamellar films, they are not restricted to this structure. They have also been observed for both cylindrical and spherical morphologies in thin films when the initial film thickness was not commensurable with the domain spacing.⁴² Therefore these features in films of B₃₇₀₀E₂₉₀₀ are compatible with the HPC phase observed in bulk. AFM images of the crystallised thicker samples C and D display the perpendicular lamellae observed earlier by Reiter et al.²⁴ However, the thinner films A and B show a hole/island topography (see Figure 3.17). The phase pictures reveal layers parallel to the surface coexisting with islands comprising perpendicular lamellae (Figure 3.17b, c).

To obtain a more quantitative picture of the thin film morphology we performed x-ray reflectivity of both the molten and the crystalline state (see Figure 3.18). The reflectivity curves are modulated by Kiessig fringes with a period $\Delta q_z = 2\pi/D$, in which D is the film thickness. The crystallised samples show smeared oscillations that reflect the roughening

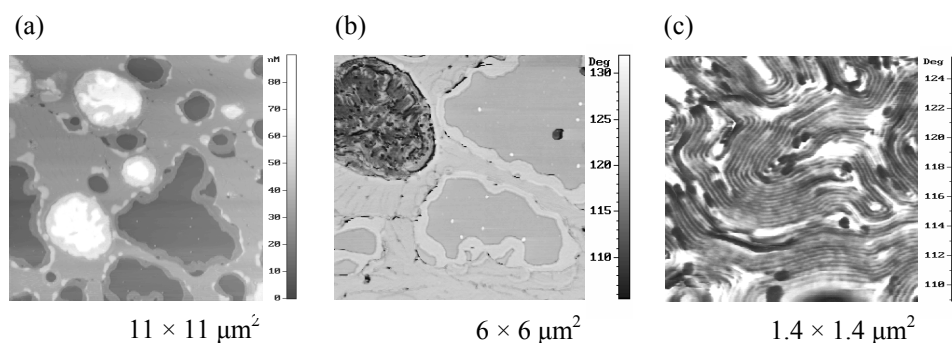


Figure 3.17. Tapping mode AFM images of $B_{3700}E_{2900}$ crystallised at 40°C in films spin-coated from 0.5% DCM solution (sample B). (a) Topography image showing multiple height levels on the surface resembling hole/island structure of lamellar diblock copolymer films. (b) Phase picture revealing difference in the phase contrast between an island (upper left corner) and the rest of the film. (c) Blowup of the island showing lateral phase variations with a period of about 20 nm.

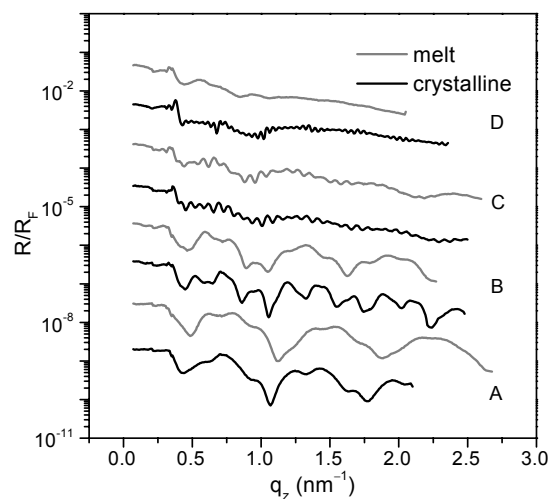


Figure 3.18. Pairs of specular x-ray reflectivity curves of $B_{3700}E_{2900}$ thin films at 90°C (melt) and 35°C (crystalline), respectively. A, B, C, D indicate the sample in increasing thickness. The curves are shifted for clarity.

seen by optical microscopy. The observed beating in the melt of samples C and D corresponds to discrete height levels on the surface with $\Delta\Lambda = 18 - 19$ nm. None of the curves displays Bragg peaks as found in lamellar B₃₇₀₀E₄₃₀₀ films,²³ excluding once more a regular planar lamellar morphology for the film structure.

3.5.3 Discussion

The results from bulk B₃₇₀₀E₂₉₀₀ indicate a melt morphology of hexagonally packed cylinders. From the combination of SAXS and AFM/TEM images we conclude that in the bulk upon crystallisation the HPC phase of the amorphous melt most probably transforms into a HPL phase. A HPL phase gives two fundamental x-ray reflections corresponding to the layer structure and the hexagonal perforations, respectively. From simple geometrical considerations their positions differ for a simple ABAB.. stacking by a factor $2/\sqrt{3}$.⁴³ It needs a uniform sample to observe this difference, which is not resolved in the relatively broad peak of Figure 3.14. In Ref. 7 SAXS from a uniform sample confirmed the interpretation as perforated lamellae of AFM images very similar to Figure 3.15a. Because we did not succeed in obtaining a uniform sample in the present case, additional TEM measurements were performed (see Figure 3.15b). Note that unstained samples were used, preventing any possible influence of the staining process on the morphology. The drawback is that the resulting pictures have little contrast and do not reproduce very well. Nevertheless, close inspection reveals lines with similar modulations as observed by AFM and again absence of any ‘head-on’ cylinders. We conclude that the TEM results substantiate the interpretation of a HPL phase upon crystallisation, though we cannot fully exclude the possibility of a strongly distorted HPC phase.

Cooling down the melt causes an increase in χ leading to stretching of the polymer chains. As a consequence an increase in both the intercylinder distance a and the peak intensity is measured by SAXS. The crystallisation of the PEO-block leads to a jump-like increase in χ . At low supercooling the increasing strength of the microphase separation is in kinetic competition with the tendency of the crystals to form lamellae. In several cases this has been observed to shift the morphology from HPC to lamellar.¹ Alternatively this can drive the development of a HPL phase as a compromise between improved cylindrical block ordering and crystalline lamellae.⁷ The HPL phase takes the form of alternating PEO

and PB_h layers, in which the PEO layers are interrupted by hexagonally arranged PB_h perforations. The HPL phase has been observed at thermally induced phase transitions from a lamellar to a HPC phase⁴⁴ and in mechanically sheared samples.⁴⁵

In thin films, additional surface interactions come into play imposing segregation of the components at the interfaces. In lamellar BE films the dissimilar film boundaries dictate wetting PEO and PB_h layers on the substrate and the air interface, respectively.²³ As a result the thickness of the film equals $(n + 0.5)L$. While any cross-section parallel to the lamellae exhibits the same symmetry as a planar surface, this is not the case in cylinder-forming systems. In the latter case a planar surface always breaks the symmetry of the bulk structure and the microdomain phase has to adjust. Hence, a variety of deviations from the bulk morphology has been observed near surfaces and in thin films, such as wetting layers, perforated lamellae, and lamellae, which have been identified as surface reconstructions (see Refs. 46 and 47). For dissimilar interfaces hybrid structures have been found and successfully modelled.⁴⁶ AFM images from the crystallised $B_{3700}E_{2900}$ films A and B (Figure 3.17) indicate wetting layers at the surface. We assume that in particular the affinity of the PEO-block for the silica surface drives the formation of parallel lamellae. The effect of the surface field persists over 3 layers in sample B (Figure 3.17a) unlike the predicted decay length of about one period.⁴⁶ Apparently, for a certain film thickness both the substrate and the air interfaces act coherently and cause parallel alignment over several layers. Yet in the interior of the thicker films C and D the bulk morphology should be preserved. Combining these two aspects we assume that in the melt of thick $B_{3700}E_{2900}$ films homogeneous wetting layers orient the cylinders in the central part of the films parallel to the substrate. Thus alternating quasi-layers of PEO cylinders surrounded by PB_h and pure PB_h regions will be formed. This model implies a terrace height $\Delta\Lambda$ of the order of the average bulk repetition period $L = 2\pi/q_{100}$. Indeed, $L = 18.1$ nm at 90°C is comparable to the height difference $\Delta\Lambda = 18 - 19$ nm given by the beating in the x-ray reflectivity (Figure 3.18).

To check the structure discussed, we modeled the density profile of the molten sample C in various ways. As a starting point we represented the PEO cylinders embedded in the rubbery PB matrix by four consecutive layers parallel to the surface with a thickness $L \approx 18$ nm. Each of them consisted of sublayers of pure PB (matrix) and of mixed PB/PEO (embedded cylinders). The density of the latter layers was taken as a weighted average of

the densities of the pure components. In addition we introduced half a wetting layer ($L/2$) of PEO at the substrate, bringing the total to 4.5 layers contributing to the film thickness. The resulting reflectivity curve had many orders of Bragg peaks not observed in the experimental data. Subsequent variation of the density of the layers, the roughness and the period did not lead to significant improvement. A reasonable fit (see Figure 3.19a) could only be obtained by modifying the slab close to the air interface taking instead of mixed PB/PEO (as in the ‘bulk’ of the film), a pure PEO sublayer (see Figure 3.19b). This leads to some redistribution of the PEO cylinders in the PB matrix disturbing the regular periodicity. Note that the results in Figure 3.19a are displayed as R/R_F on a logarithmic scale, highlighting the deviations from a perfect fit rather than the qualities of the fitting. In order to take the different height levels on the surface into account we simulated two curves for films with 4.5 and 3.5 layers. By adding them incoherently with a weight factor w we obtained the fit shown in Figure 3.19b. For the 3.5-layer film we used $D = 67.4$ nm and $w = 0.35$, and for the 4.5-layer film $D = 86.2$ nm and $w = 0.65$. The weight factors imply that, on average, the top layer consists of 65% elevations and 35% depressions and the total film thickness is quantized as $(n + 0.5)L$ with $L = 19 \pm 1$ nm. The results for the 4.5-layer film are summarized in Table 3.2. They show somewhat low values for the thickness of the PB/PEO sublayer and high ones for the pure PB sublayer. We attribute this to the interlayer roughness that is of the order of several nanometers. The results indicate a variation in L from layer to layer with the period in the interior of the film being close to the bulk one. Hence though layering is involved there is no repetition that would lead to Bragg reflections.

We applied the same model and fitting procedure to the other reflectivity curves from the melt. A fit of sample D with 7.5 layers gave $D = 142$ nm and an average period of 19 nm. The values of the parameters essentially confirm the results from the 1% sample. For the thinner films A and B different parameters of the cylindrical and lamellar layers along the limiting interfaces were needed. Moreover, due to the uneven surface coverage, several layers with different characteristics had to be added. As anticipated from the earlier discussion, because of the difference in interior structure the parameters of thicker films were not directly suitable to fit the curves of the thinner ones. Upon crystallisation the reflectivity curves smear due to roughening of the air/film interface and show no additional features. For samples A and B a model with a lamellar layer covering the surface of the

film is not applicable as the AFM pictures show lateral phase variation that coexist with laterally homogeneous layers. In the bulk $B_{3700}E_{2900}$ the HPC phase transforms to HPL, which, depending on the amount of supercooling, leads to a 10 to 50% increase in the period. The same phenomenon should lead to an increase in the film thickness but the quality of the fringes in the experimental XR curves does not allow an unambiguous direct estimate.

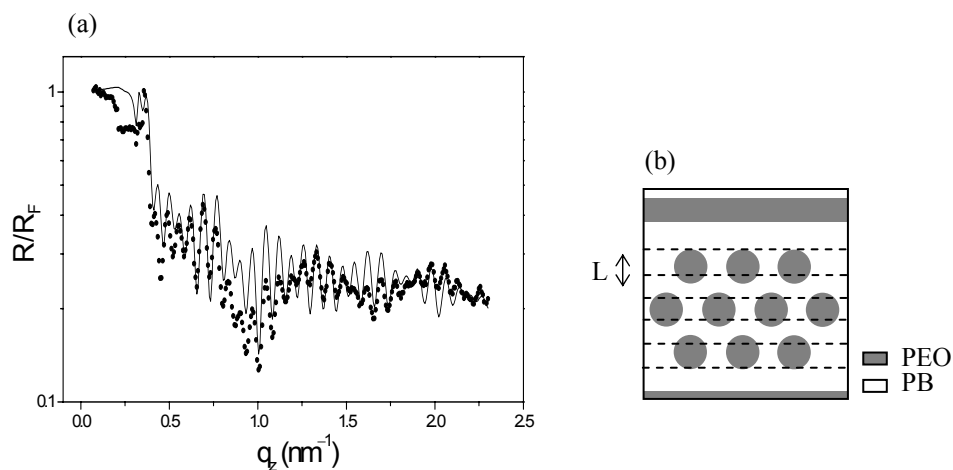


Figure 3.18. Modelling of the x-ray reflectivity of film C of $B_{3700}E_{2900}$ in the melt at 90°C . (a) Reflected intensity divided by the Fresnel reflectivity R_F and corresponding fit (full line). (b) Model of a cross-section of the thin film morphology.

Combination of all experimental results indicates a hybrid melt morphology for films of $B_{3700}E_{2900}$. The surface affinity of the copolymer blocks drives the formation of wetting layers on the top (PB_n) and bottom (PEO) interfaces. As a result, in the interior of the thicker films PEO cylinders tend to orient parallel to the surface. This hybrid morphology complicates the discussion of the subsequent PEO crystallisation, and does not seem to allow a simple model for understanding perpendicular crystalline lamellae we have been looking for. Nevertheless let us compare our results with the original observations in Refs. 24, 25, in which the authors associate the presence of terraces on the film surface with a lamellar structure parallel to the substrate. Our results indicate that the morphology in the interior of the thicker films differs from the top and bottom interfaces. Moreover the AFM images (Figure 3.17) unequivocally show a hybrid crystalline morphology for the thinner

films. In Refs. 24, 25 the crystallisation is assumed to be connected to a decrease in d_{PEO} , the PEO sublayer thickness. The associated lateral *expansion* is supposed to be difficult to accommodate, leading in thin films to vertical lamellae ('escape into the third dimension'). However, from the work of Opitz et al.²³ we know that in lamellar films d_{PEO} increases upon crystallisation to accommodate the nearest (half) integer number of stems. In uniform

Table 3.2 Fitting parameters for a 4.5-layer film (sample C).

slab	composition	density ($10^{-3} \text{ e}^{-} \text{ nm}^{-2}$)	d (nm)	L (nm)	roughness (nm)
1	PB	8.87	4.60		1.1
2	PEO	10.33	9.50	21	1.5
3	PB	8.87	11.5		0.9
4	PEO/PB	9.38	9.50	18.8	1.1
5	PB	8.87	9.30		1.7
6	PEO/PB	9.35	9.50	18.2	1.4
7	PB	8.87	8.70		1.5
8	PEO/PB	9.25	11.2	20.3	1.0
9	PB	8.87	9.10		1.0
10	PEO	10.44	3.25		1.0

lamellar films this is accompanied by lateral *contraction*, leading to cracks through the whole film. In the present case the crystallisation might start from the wetting layers at the interfaces that are necessarily most stretched. The strain in the wetting layers and the hybrid morphology now can probably serve to accommodate any contraction upon crystallisation. Note that for crystallisation inside a PEO cylinder the diameter of the cylinder (about 13.5 nm) can neither accommodate a non-folded PEO chain of 18.5 nm nor a series of (half)integer folded chains. Orientation of the stems along the cylinder axis (crystal lamellae perpendicular) would not lead to such restrictions and might be favoured. For cylinders parallel to the substrate this allows the possibility of crystalline lamella perpendicular to the substrate, even though other possibilities are not excluded. Further modelling should include the interaction between PEO in the cylinders and in the wetting

layer near the surface, which seems to be prohibitively difficult. Due to the complicated hybrid structures the final result is expected to depend strongly on the detailed experimental conditions, as is indeed observed.

In summary, in bulk $B_{3700}E_{2900}$ the melt morphology of HPC most probably transforms into a HPL phase upon crystallisation. In thin films, wetting layers of PB_h and PEO develop at the top and bottom interfaces respectively. In the melt these layers force the cylinders in the interior of the film to orient parallel to the substrate. The crystallisation of the PEO block giving perpendicular lamellae cannot be ascribed to a simple process. Because of the complicated hybrid structures, the final result can vary depending on the history and associated kinetic pathways, and in general lateral structures develop coexisting with lamellar layers in thinner films.

3.6 Concluding remarks

We have studied the bulk and thin film morphology of a PEO-*b*- PB_h copolymers, differing in molecular weight and volume fraction, using simultaneous SAXS/WAXS, x-ray reflectivity, optical microscopy, AFM and TEM. The morphology of symmetric $B_{3700}E_{4300}$ is lamellar in the molten and crystalline state, in accordance with theoretical expectations. For $B_{1270}E_{1450}$, a discontinuous ODT was found at 110°C accompanied by strong fluctuations. In the asymmetric $B_{3700}E_{2900}$, the melt morphology of HPC most probably transforms into a HPL phase upon crystallisation.

In thin films of PEO-*b*- PB_h copolymers wetting layers of PB_h and PEO develop at the top and bottom interfaces, respectively. In the symmetric samples, this results in formation of layers parallel to the surface, where the crystallisation of the PEO block leads to an increase in the lamellar thickness of both blocks. As the density of PEO increases upon crystallisation, this effect is accompanied by a contraction in the lateral direction, which results in cracking of the film. In the melt of $B_{3700}E_{2900}$, the wetting layers force the cylinders in the interior of the film to orient parallel to the substrate. Because of the complicated hybrid structures, the final result can vary depending on the history and associated kinetic pathways, and in general lateral structures develop coexisting with lamellar layers in thinner films.

References

- [1] See for example: Hamley, I.W., *The Physics of Block Copolymers* (Oxford University Press, Inc. New York), 1998.
- [2] DiMarzio, E.A., Guttman, C.M., Hoffman, J.D., *Macromolecules* 13, 1194, 1980.
- [3] Whitmore, M.D., Noolandi, J., *Macromolecules* 21, 1482, 1988.
- [4] Vilgis, T., Halperin, A., *Macromolecules* 24, 2090, 1991.
- [5] (a) Zhu, L., Chen, Y., Zhang, A., Calhoun, B.H., Chun, M., Quirk, R.P., Cheng, S.Z.D., Hsiao, B.S., Yeh, F.J., Hashimoto, T., *Phys. Rev. B* 60, 10022, 1999; (b) Zhu, L., Cheng, S.Z.D., Calhoun, B.H., Ge, Q., Quirk, R.P., Thomas, E.L., Hsiao, B.S., Yeh, F.J., Lotz, B., *J. Am. Chem. Soc.* 122, 5957, 2000.
- [6] (a) Loo, Y.-L., Register, R. A., Ryan, A. J., *Macromolecules* 35, 2365, 2002; (b) Loo, Y.-L., Register, R. A., Ryan, A. J., Dee, G. T., *Macromolecules* 34, 8968, 2001.
- [7] Li, L., Serero, Y., Koch, M. H. J., de Jeu, W. H., *Macromolecules* 36, 529, 2003.
- [8] Leibler, L., *Macromolecules* 13, 1602, 1980.
- [9] Keller, A., *Faraday Disc.* 68, 145, 1979.
- [10] Keller, A., Goldbeck-Wood, G., *Comprehensive Polymer Science, 2nd Supplement* (Elsevier, Oxford), Aggarval, S. L., Russo, S., 241, 1996.
- [11] Strobl, G.R., *The Physics of Polymers* (Springer, Berlin), 1996.
- [12] See the special issue: *Polymer* 41, 8751-8930, 2000.
- [13] Doye, P.K., Frenkel, D., *J. Chem Phys.* 110, 2692, 1999.
- [14] Liu, C., Muthukumar, M., *J. Chem Phys.* 109, 2536, 1998.
- [15] Hamley, I.W., *Adv. Polymer Sci.* 148, 113, 1999.
- [16] Hong, S., MacKnight, W. J., Russell, T. P., Gido, S. P., *Macromolecules* 34, 2876, 2001.
- [17] Helfand, E., Wasserman, Z. R., Chapter 4. In *Development in Block Copolymers I* (Applied Science Publishers, London), 99, 1982.
- [18] Hamley, I.W., Fairclough, J.P.A., Bates, F.S., Ryan, A.J., *Polymer* 39, 1429, 1998.
- [19] Mai, S., Fairclough, J.P.A., Hamley, I.W., Matsen, M.W., Denny, R.C., Liao, B., Booth, C., Ryan, A.J., *Macromolecules* 30, 8392, 1997.
- [20] Hamley, I.W.; Wallwork, M.L.; Smith, D.A.; Fairclough, J.P.A.; Ryan, A.J.; Mai, S.-M.; Yang, Y.-W.; Booth, C. *Polymer* 39, 3321, 1998.

- [21] Mai, S.-M.; Fairclough, J.P.A.; Hamley, I.W.; Matsen, M.W.; Denny, R.C.; Liao, B.; Y.-W.; Booth, C.; Ryan, A.J. *Macromolecules* 29, 6612, 1996.
- [22] de Jeu W. H., Polymer Crystallization: Observations, Concepts and Interpretations/ edited by Reiter G. and Sommer J.-U., Berlin: Springer, 196-207 (Springer Lecture Notes in Physics; 606), 2003.
- [23] Opitz, R., Lambreva, D. M., de Jeu W. H., *Macromolecules* 35, 6930, 2002.
- [24] Reiter, G., Castelein, G., Hoerner, P., Riess, G., Blumen, A., Sommer, J.-U., *Phys. Rev. Lett.* 83, 3844, 1999.
- [25] Reiter, G., Castelein, G., Hoerner, P., Riess, G., Sommer, J.-U., Floudas, G., *Eur. Phys. J. E.* 2, 319, 2000.
- [26] Bates, F. S., Frederickson, G. H., *Physics Today, February* 52(2), 32, 1999.
- [27] Helfand, E., Wasserman, Z. R., *Macromolecules* 9, 879, 1976; 11, 960, 1978; 13, 994, 1980; Noolandi, J., Hong, K. M., *Ferroelectrics* 30, 117, 1980; Hong, K. M., Noolandi, J., *Macromolecules* 14, 727, 1981; Whitmore, M. D., Noolandi, J., *J. Chem. Phys.* 93, 2946, 1990.
- [28] Semenov, A. N., *Sov. Phys. JETP* 61, 733, 1985.
- [29] Matsen, M. W., Schick, M., *Phys. Rev. Lett.* 72, 2660, 1994; *Macromolecules* 27, 6761, 1994; 27, 7157, 1994; Matsen, M. W., Bates, F. S., *Macromolecules* 29, 1091, 1996.
- [30] Frederickson, G. H., Helfand, E., J., *Chem. Phys.* 87, 697, 1987.
- [31] Bates, F. S., Rosedale, J. H., Frederickson, G. H., Glinka, C., *Phys. Rev. Lett.* 61, 2229, 1988.
- [32] Barrat, J. L., Fredrickson, G. H. *J. Chem. Phys.* 95, 1281, 1991.
- [33] Hajduk, D. A., Takenouchi, H., Hillmyer, M. A., Bates, F. S., Vigild, M. E., Almdal, K., *Macromolecules* 30, 3788, 1997.
- [34] Kim, D.-C., Lee, H.-K., Sohn, B.-H., Zin, W.-C., *Macromolecules* 34, 7767, 2001.
- [35] Li, L., Lambreva, D. M., de Jeu, W. H., *J. Macromol. Sci. B* 43, 59, 2004.
- [36] Hillmyer, M. A., Bates, F. S., *Macromolecules* 29, 6994, 1996.
- [37] Hajduk, A. D., Kossuth, M. B., Hillmyer, M. A., Bates, F. S. J., *Chem. Phys. B* 102, 4269, 1998.
- [38] Cheng, C. Z. D., Zhang, A. et al., *Macromolecules* 24, 3937, 1991.
- [39] Hu, W., Albrecht, T., Strobl, G., *Macromolecules* 32, 7548, 1999.

- [40] Hikosaka, M., *Polymer* 28, 1257, 1987.
- [41] Hikosaka, M., *Polymer* 31, 458, 1990.
- [42] Harrison, C., Park, M., Chaikin, P. M., Register, R. A., Adamson, D. H., Yao, N., *Polymer* 39, 2733, 1998.
- [43] Förster, S., Khandpur, A. K., Zhao, J., Bates, F. S., Hamley, I.W., Ryan, A. J., Bras, W., *Macromolecules* 27, 6922, 1994.
- [44] Hamley, I. W., Koppi, K. A., Rosedale, J. H., Bates, F. S., Almdal, K., Mortensen, K., *Macromolecules* 26, 5959, 1993; Hajduk, D. A., Gruner, S. M., Rangarajan, P., Register, R. A., Fetters, L. J., Honeker, C., Albalak, R. J. et al., *Macromolecules* 27, 490, 1994.
- [45] Qi, S., Wang, Z. G., *Macromolecules* 30, 4491, 1997; Hajduk, D. A., Takenouchi, H., Hillmyer, M. A., Bates, F. S., Vigild, M. E., Almdal, K., *Macromolecules* 30, 3788, 1997.
- [46] Lyakhova, K. S., Sevink, G. J. A., Zvelindovsky, A. V., *J. Chem. Phys.* 120, 1127, 2004.
- [47] Knoll, A., Horvat, A., Lyakhova, K. S., Krausch, G., Sevink, G. J. A., Zvelindovsky, A. V., Magerle, R., *Phys. Rev. Lett.* 89, 035501-1, 2002.

Chapter 4 Nano-structures in thin films of semifluorinated alkanes

In this chapter an x-ray study on the structure of supported monolayers of $F(CF_2)_{14}(CH_2)_{20}H$ will be presented. Depending on the preparation method these monolayers self-organize into 'ribbons' or 'spirals'. X-ray reflectivity reveals a layer thickness less than the extended length of the molecule. Grazing-incidence x-ray diffraction shows that the fluorinated segments orient normal to the layer and can be crystalline or amorphous without altering the morphology. We propose a model with tilted hydrocarbon chains resulting in an 'easy' axis that explains qualitatively the ribbon structure

4.1 Introduction

Semifluorinated alkanes $F(CF_2)_n(CH_2)_mH$ (abbreviated as F_nH_m) received much attention owing to their potential application as repellent systems in material and biological science.^{1,2} These ‘primitive surfactants’ segregate into distinct domains in the melt as well as in the crystalline state³⁻⁷ and self-organize in a variety of crystalline and mesogenic phases. This behavior originates from the presence of the two ‘mutually phobic’ blocks, a fluorinated and a hydrogenated chain, linked by a covalent bond. Their reciprocal phobicity or incompatibility stems from the atomic properties of the fluorocarbon part with its high electronegativity. Moreover the van der Waals radius exceeds by 25-30% the hydrocarbon van der Waals radius. Furthermore the reduced conformational freedom produces bulky and stiff chains, typically arranged in a helical conformation. The dense, electron-rich coating of the chain’s skeleton results in small intermolecular interactions.⁸ This is why fluorocarbons are thermally, chemically and biochemically more stable than hydrocarbons. The use of semifluorinated *n*-alkanes as side groups in homopolymers or block copolymers has been shown to generate polymers with low-surface-energy properties. On the other hand, semifluorinated *n*-alkanes have been reported to spread at the air-water interface and form Langmuir films. Other properties such as a low dielectric constant and refractive index, a high vapor pressure, compressibility and gas solubility,⁸ expand the possibilities for practical use of these rather special chemicals.^{1,9,10}

The antagonistic nature of the two building units and the mismatch in cross section between the perfluoro and the perhydro alkyl tail result in distinct superstructure formation. Depending on block length and temperature, the competition between ordering of the hydrocarbon blocks and fluorocarbon blocks results in a rich polymorphism of these compounds, not fully understood yet¹ Typically layered smectic structures are formed, in which interdigitation, tilting and partial disordering of the alkyl chain segments compensates for the mismatch in the van der Waals diameters of the two blocks.^{6,7,11,12}

In ultrathin layers with a thickness comparable to the molecular length, interactions with and constraints by the interfaces become important. In combination with competing ordering of the fluorinated and hydrogenated building blocks, this results in structures that can differ significantly from the bulk smectic organisation.^{12,13} This issue has been

addressed in earlier studies on Langmuir-Blodgett films.⁴ The interactions between the fluorinated moieties were found to dominate the structure of a monolayer, preserving a hexagonal close packing of the fluorinated segments.^{4,5} For the hydrocarbon block a layer with liquid-like order was reported. Scanning force microscopy showed that a Langmuir-Blodgett film, resulting from transfer of a monolayer of F_8H_{16} onto a silicon oxide surface, consisted of discrete monodisperse aggregates. The formation of these structures was explained by surface-induced aggregation i.e. as ‘surface micelles’, with a size controlled by the density mismatch between the fluorinated and hydrogenated segments.^{4,5} Similar superstructures have been observed for partially fluorinated fatty acids on an aqueous subphase.⁴

Significant effort has been dedicated to elucidate the effect of the relative length of each of the blocks on the ordering in a single layer, but so far no explanation has been given on the formation of finite aggregates. In the following we address this issue and report on the two-dimensional (2D) assembly of molecularly thin films of eicosylperfluorotetradecane, $F_{14}H_{20}$, on silicon/ SiO_2 .

A. Mourran et al.¹⁴ showed that monolayers of $F_{14}H_{20}$ (Figure 4.1) on a solid substrate are laterally structured. SFM revealed two types of nanostructures, named ribbons and spirals (see Figure 4.2) depending on the solvent used to prepare the samples. In solvents

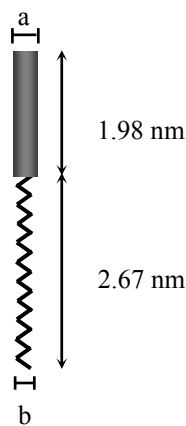


Figure 4.1. *Molecular dimensions of $F_{14}H_{20}$. The van der Waals diameters of (a) the fluorinated and (b) the hydrogenated parts are 0.56 and 0.42 nm, respectively.*

good for either the hydrocarbon part (decalin) or fluorocarbon part (perfluorodecalin) the formation of ribbons was favored, while in non-selective solvents (hexafluoroxylyene) a spiral morphology was dominating. In addition, morphological transformations were observed in situ when a sample was exposed to the vapor of the other type of solvents. The characteristic dimensions of both types of morphology are identical which suggests that the difference resides in the molecular packing.

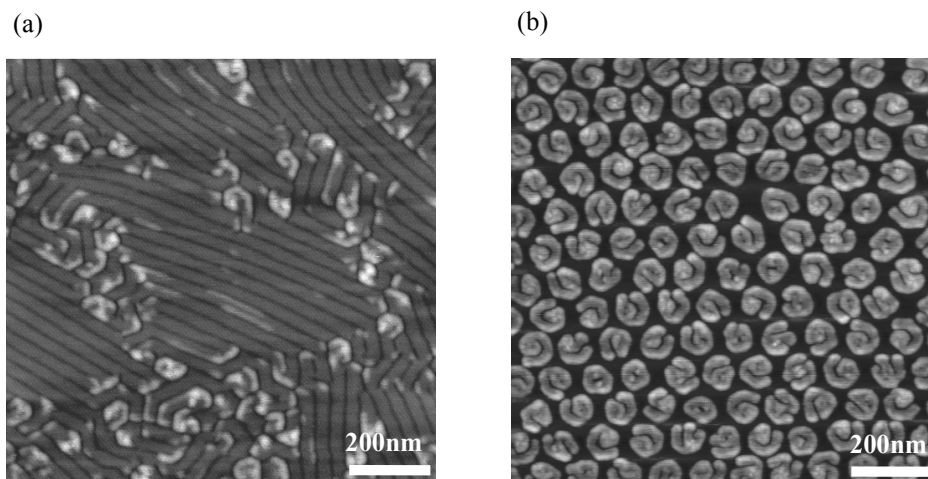


Figure 4.2. *SFM tapping-mode topography images of $F_{14}H_{20}$ monolayer on a silicon substrate, prepared from (a) decalin and (b) HFX solution.*

In this chapter we present a combined x-ray study of the in-plane and normal packing of $F_{14}H_{20}$. X-ray reflectivity was used to measure the film thickness and to probe the laterally averaged electron density normal to the substrate. Grazing-incidence x-ray diffraction provided insight into the in-plane molecular arrangement. The results allow us to propose a model for the molecular structure of the self-assembled objects.

4.2 Experimental

Materials and sample preparation. The samples and the SFM pictures for our study were kindly provided by A. Mourran (University of Ulm, Germany). Here we present only brief information on the sample preparation as adopted from Ref. [14]. $F_{14}H_{20}$ was synthesized

according to the procedures reported in Ref. [7]. Thin films were prepared from low-concentration solutions (0.1 g/L) in three types of solvents: selective solvents for either the fluorinated block (perfluorodecalin, perfluorohexane) or the hydrocarbon block (decalin, xylene, iso-octane, chloroform), and a solvent able to dissolve both parts of the molecule (hexafluoroxylene). Monolayers of $F_{14}H_{20}$ were transferred to a silicon substrate by the Langmuir-Blodgett (LB) technique. Starting from a compressed closed film on the LB-trough optimum coverage of the surface could be ensured. The quality of the transfer was controlled by SFM and only samples with a coverage $>90\%$ were used for the x-ray investigations.

X-Ray reflectivity. The films were investigated by specular x-ray reflectivity at beamline BW2 of HASYLAB (DESY, Hamburg) at an energy of 10 keV corresponding to a wavelength $\lambda = 0.124$ nm. The resolution was set at $\Delta q_z = 0.025$ nm⁻¹. The density profile was determined by comparing the calculated and the experimental reflectivity.¹⁵ Calculations were based on the Parratt algorithm using a parameterized molecular model in which two sub-layers were approximated by a box-like function characterized by thickness and density, convoluted with a Gaussian probability describing the interfacial roughness (see Sec. 2.3.1). The best-fit curve to the data was determined by a minimization procedure leading to a density and roughness profile along the film normal. The total thickness was directly determined by the interference oscillations (Kiessig fringes) between x-rays reflected from the top and bottom of the film, which is in principle model independent.

Grazing-incidence x-ray diffraction (GIXD). was performed both at beamline BW2 of HASYLAB (DESY, Hamburg) at 10 keV and at BM26 (DUBBLE) of the ESRF (Grenoble). In the latter case the energy was 15.9 keV leading to $\lambda = 0.0779$ nm. In GIXD the x-ray beam is incident at the surface of the sample at a small glancing angle below the critical angle of total reflection. Under these conditions only an evanescent wave is generated that propagates along the film-air interface and penetrates into the film with an intensity exponentially decaying with depth. As discussed in Sec. 2.3.3 the evanescent wave can be considered as an incident beam for 2D x-ray diffraction, giving information about the 2D structure in the plane of the film. The incident angle was set between the critical angles of $F_{14}H_{20}$ monolayer and the substrate, respectively, resulting in 2D diffraction from the complete monolayer. The overall resolution in the sample plane was set

to 0.01 nm^{-1} . The scattered intensity was recorded at different out-of-plane angles using a scintillation detector.

4.3 Results and discussion

4.3.1 X-ray reflectivity

In order to obtain insight in the structure of the monolayers x-ray reflectivity (XR) and grazing incidence x-ray diffraction have been used. The former allows deriving the thickness and the density distribution along the normal to the interfaces. The latter gives direct evidence about the in plane packing of the semifluorinated chain molecules. Figure 4.3a shows the reflected x-ray intensity of both a film with spirals and with ribbons. The ribbon sample was fitted in detail to a two-layer model, which resulted in the density profile of Figure 4.3b. The corresponding fitting parameters are given in Table 4.1. The smaller density of the bottom layer unambiguously puts the hydrogenated part of the molecules near the surface. The single-frequency oscillations indicate a uniform thickness. From the fit of the interference fringes this film thickness was derived to be

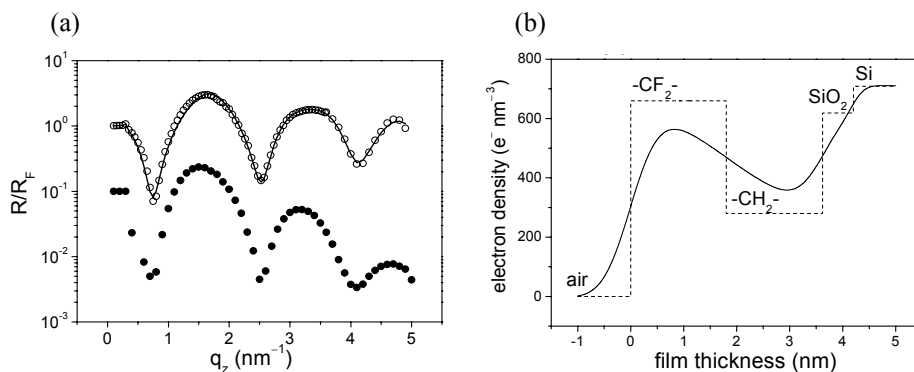


Figure 4.3. X-ray reflectivity results from a $F_{14}H_{20}$ monolayer (thickness 3.6 nm). (a) Intensity normalized to the Fresnel reflectivity for a ribbon (top) and a spiral sample (bottom). The latter has been shifted by a decade for clarity. (b) Electron density profiles.

3.6 ± 0.05 nm. This value is smaller than the length of the extended molecule i.e. 4.65 nm ($1.98 + 0.126 \times 20 + 0.15$) nm, where 1.98 nm is the length of the F block.¹⁶ It is, however, consistent with a monolayer with a tilt angle of 127° at the linkage between the fluorocarbon and the hydrocarbon segments. Geometrical considerations demonstrate that a tilt of 122° will allow closed packing of the chains in the plane defined by the zig-zag band of the all-trans planar $(\text{CH}_2)_n$ segment, this way compensating the larger cross section area of the fluorocarbon segment compared to the extended hydrocarbon tail within this plane. The van der Waals diameter of the fluorocarbon and hydrocarbon parts is 0.6 and 0.48 nm, respectively. This happens because a $-(\text{CF}_2)_m-$ sequence cannot exist in a planar zigzag configuration, as is possible for $-(\text{CH}_2)_n-$. Instead the $-(\text{CF}_2)_m-$ sequence adopts a 15/7 helix, leading to a rigid rod-like structure. The apparent tilt angle of 127° corresponds to an reduction of the length of the hydrocarbon chain by 0.2 nm by contribution of gauche conformations along the $-(\text{CH}_2)_n-$ segment caused by the mismatch of the cross-section of the constituting segments.

Table 4.1. Summary of the XR fitting results; d_{calc} is obtained from closed-packing.

	$d_{\text{fit}} \pm 0.05$ (nm)	d_{calc} (nm)	$\rho_{\text{fit}} \pm 10$ ($\text{e}^- \text{nm}^{-3}$)	ρ_{lit} ($\text{e}^- \text{nm}^{-3}$) ¹⁷	$\sigma \pm 0.05$ (nm)
$\text{F}(\text{CF}_2)_{14}$	1.80	1.98	660	670	0.42
$\text{H}(\text{CH}_2)_{20}$	1.82	2.67	280	320	1.20
SiO_2	0.58	-	fixed	618	0.39
Si	∞	-	fixed	708	0.18

The densities of the two parts of the monolayer deserve some more discussion. In the fitting procedure the densities of the substrate (silicon plus an oxide layer) are kept fixed at their literature values (Table 4.1). The top-layer density is in good agreement with the calculated one for fluorocarbons using literature data. The somewhat lower value can be attributed to the coverage of the surface, which is less than 100%. However, in the fitting

procedure the densities of the sub-layers couple strongly to their thickness. As the minimum is very shallow, this leaves some ambiguity. Therefore we have chosen to fix the densities according to the closed-packed model, taking a density slightly below the literature value for the fluorinated top-layer, and correct for the bottom layer the hydrocarbon literature values for the loose packing in the direction perpendicular to the easy axis, i.e. the ribbons. The values in Table 4.1 are the result of this procedure. Incorporation of roughness σ of the interfaces in the model (see Figure 4.3b) effectively partly mixes the two different parts, leading to some averaging of the densities. The value of σ of the top and bottom interface is as expected for soft films, but the value of the middle interface is rather large. It is difficult to imagine large density variations at this interface without the other ones also being affected. We take this large roughness as further evidence of a transition region. Hence it seems that a three-layer fit to the XR data could be more appropriate. We did not pursue such an exercise because of the associated increase in the number of parameters.

4.3.2 *Grazing-incidence x-ray diffraction*

The major results from GIXD of ribbon and spiral monolayers are summarized in Figure 4.4. Note that these results effectively correspond to 2D ‘powder’ averaged intensities. Hence the azimuthal orientation should not make any difference. For all samples we find a broad composite in-plane liquid-like peak that comprises the range of crystalline and liquid fluorocarbon and hydrocarbon (lattice) spacing d_{10} . Note that upon crystallization, the spacing of fluorocarbons hardly changes, contrary to the situation in hydrocarbons. In the latter case the closed-packed value does not necessarily correspond to full crystallization as also intermediate solid-rotator phases can play a role.¹⁸ Figure 4.5 gives details of the fitting of the upper curve from Figure 4.4 to three Lorentzians, which is significantly superior to a two-peak fit. Similar results are found for the ribbon samples (not shown). The final results are given in Table 4.2, where $d_{10} = 2\pi/q_{xy}$ and Δq_{xy} is given as the full-width-at-half-maximum (FWHM) with the correlation length as $\xi = 2/\Delta q_{xy}$. The value of ξ indicates the range of ordering associated with the peak and extends to a few molecular lengths, which is quite normal for liquid order.

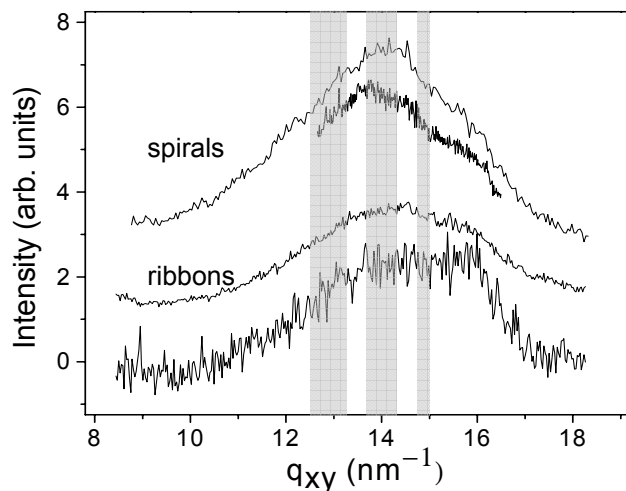


Figure 4.4. Summary of the GIXD results on $F_{14}H_{20}$ monolayers at ESRF, indicating composite liquid peaks. The gray bands indicate the q -range of literature data of (from left to right) hexagonal packed fluorocarbons, liquid-like ordered hydrocarbons and close-packed hydrocarbons, respectively.

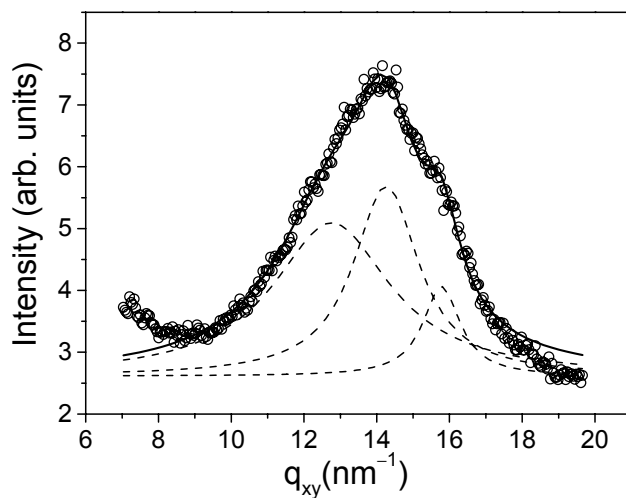


Figure 4.5. GIXD data (circles) from the amorphous $F_{14}H_{20}$ monolayer in the spiral morphology of Figure 4.2b, fitted to the sum of three Lorentzians (broken lines).

Summarizing the results so far we conclude that both the alkylated and the fluorinated parts are largely in a liquid-like state. Several liquid-like peaks have been observed and within the experimental accuracy the fits indicate q -values close to the three types of ordering indicated in Figure 4.4. The dominant fluorocarbon top layer can be considered as a single smectic-A layer with liquid in-plane ordering. Evidently any tendency to crystallize in these monolayer samples is strongly suppressed.

At a later stage we studied a new series of samples at HASYLAB and found the rather different behavior indicated in Figure 4.6. In contrast to the previous series, a crystalline peak now dominates the in-plane diffraction. The fitting results for the central Gaussian crystalline peaks are given in Table 4.3 with the width given by $L = 2\pi/\Delta q_{xy}$. From the observed spacing we conclude that the fluorocarbon top layer is involved in the crystallization. The finite width of the crystalline peak agrees well with the transverse size of the ribbons. Figure 4.7 shows a 2D contour plot of the x-ray intensity in the (q_z, q_{xy}) -plane, indicating clearly that the fluorocarbon chains in the crystalline layer are not tilted. We emphasize that for this second series of samples the morphology as seen in AFM (studied both before and after the x-ray measurements) is not different from the earlier series. The only different aspect of the sample treatment is transport between Aachen and Amsterdam in July for the first series (summer) and in December for the second one (winter). Hence we assume that crystallization has occurred in the second series by exposure to lower temperatures during transport.

Table 4.2: *Summary of the three-Lorentzian GIXD fitting results from the amorphous monolayers (ESRF).*

Sample type	$q_{xy} \pm 0.1$ (nm^{-1})	$d_{10} \pm 0.05$ (nm)	$\Delta q_{xy} \pm 0.05$ (nm^{-1})	$\xi \pm 0.1$ (nm)
Ribbon	13.4	0.47	3.3	0.6
	14.9	0.42	2.0	1.0
	15.9	0.39	0.9	2.3
Spiral	12.8	0.49	3.9	0.5
	14.3	0.44	2.2	0.9
	15.8	0.40	1.2	1.6

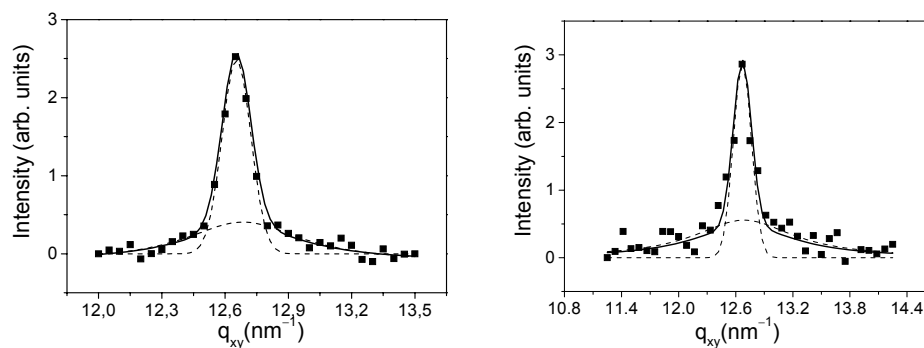


Figure 4.6. GIXD data (HasyLab) from crystallized $F_{14}H_{20}$ monolayers with donut (left) and ribbon (right) morphology (solid squares). The full line gives a fit to a Gaussian diffraction peak and a Lorentzian amorphous background (broken lines).

Table 4.3. Summary of the Gaussian GIXD fitting of the crystallized monolayers (HasyLab).

Sample	$q_{xy} \pm 0.01$	$d_{10} \pm 0.05$	$\Delta q_{xy} \pm 0.05$	$L \pm 0.5$
	(nm^{-1})	(nm)	(nm^{-1})	(nm)
Ribbon	12.6	0.49	0.19	33
Spiral	12.6	0.49	0.14	46

The final conclusions from the GIXD experiments can be summarized as follows. (i) The non-tilted fluorocarbon top layer determines the morphology both for ribbons and spirals. (ii) Whether this top layer is smectic (liquid in-plane order) or crystalline, appears to be of minor importance. At first sight the latter point might be surprising. However, from free-standing smectic liquid crystalline films it is known that for thin films up to several tens of layers, there is hardly any difference in physical behavior between smectic-A films with liquid layers and crystalline-B films in which the layers are crystallized¹⁹. In both situations the film properties are surface dominated because it takes many layers to build up the 3D structure for which shear elasticity starts playing a role. Transferring this knowledge to the present situation there is no reason to expect much difference between a liquid and a crystallized fluorinated single smectic layer.

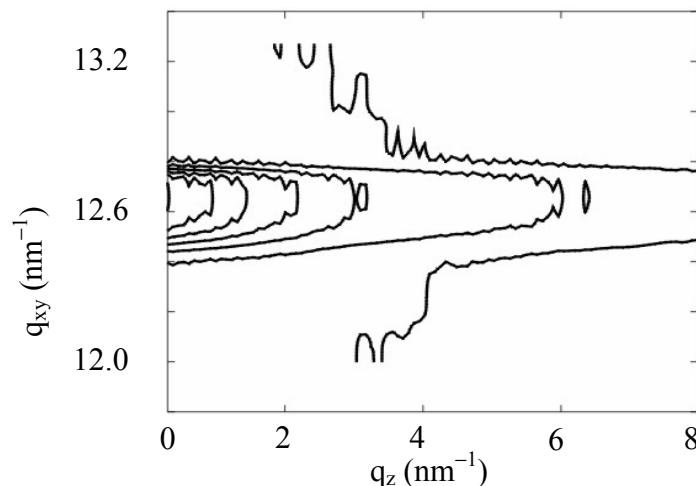


Figure 4.7. *Two-dimensional contour plot of the GIXD intensity of crystallized $F_{14}H_{20}$ monolayers with spiral morphology.*

4.3.3 Model considerations

To put the results so far in a broader context, we first note that F_nH_m compounds in their high-temperature bulk solid phase are commonly arranged in monolayer lamellar stacks. In these stacks the fluorinated chains are oriented vertical to the planes of the 2D close packing, while the hydrocarbon tails are in a weakly ordered liquid-like state with large number of gauche defects along the chain.¹¹ This type of structure is retained in the monolayers found at surface freezing of semifluorinated alkane melts $F_{12}H_n$ above the bulk freezing point,¹² at least for the shorter H-blocks. For $F_{12}H_{18}$ (which is close to our sample) only short-range in-plane order was observed. GIXD of monolayers of $F_{12}H_{18}$ at the air-water interface indicated hexagonal closed packing, though this equilibrium was only reached after appreciable time.²⁰ From these results it seems that our $F_{14}H_{20}$ system is close to a transition region (in terms of the respective block length) for which the monolayers ‘hesitate’ to crystallize. This explains at least partly the difference in behavior between series 1 (composite liquid in-plane order) and series 2 (crystallized fluorocarbon layers). Another factor contributing to suppression of crystallisation is probably the confined

structure of the ribbons. In series 2 this lateral confinement is expressed as finite-size broadening of the crystalline peaks of the fluorinated layers.

Let us now consider the basic elements of the ribbon structure. The possibility of a tilted arrangement of the hydrogenated part with respect to the fluorinated part of the molecules, has so far received little attention in the vast literature about fluorinated alkanes.²¹ However, as mentioned above this optimum packing can only materialize in one plane, leading to an ‘easy’ long direction that in principle explains the ribbon-like structures. Perpendicular to the easy direction the frustration due to the difference in van der Waals radii of the fluorinated and hydrogenated parts is not released. In Figure 4.8 two extreme possible models are sketched for the structure of a cut perpendicular to the long direction of a ribbon. In model I the fluorocarbon parts of the molecules are assumed to interact strongly and to form a single smectic or crystalline layer. The hydrocarbon parts have to accommodate to this situation leading to a frustrated bottom layer. The hydrocarbon parts in the long direction of the ribbons are close-packed allowing only a little freedom to coil in the frustrated direction. The chains can mainly tilt and may coil somewhat in order to optimize the packing. As a result, only a fluorinated layer of limited width can be supported, which will end abruptly. Evidently this leads to an approximately constant width, which should vary with the length of the alkyl chains.

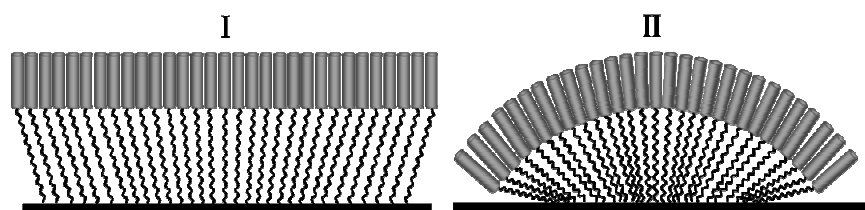


Figure 4.8. *Cartoon of two extreme possibilities for the organization of $F_{14}H_{20}$ ribbons in the frustrated direction.*

Model II can be considered as the other extreme, in which the molecules are assumed to be effectively wedge-shaped. It assumes that the hydrocarbon packing dominates and the thicker fluorocarbon part follows. Such packing is known for some smectic phases of liquid

crystalline molecules.²² It will lead to a continuous curvature of the upper surface, and consequently to a constant width.

Considering the overall situation there is considerable evidence in favour of model I:

- In x-ray reflectivity relatively pronounced minima are observed, indicating a well-defined structure of layers. In the case of a strong curvature (model II) a parallel x-ray beam would experience a broad distribution of incident angles. In that situation there is no well-defined thickness and no Kiessig fringes would be observed in the x-ray reflectivity. In fact the minima disappear at an angular spread larger than about 0.1° . Hence this number puts an upper limit to curved regions that still contribute to the distinguishing features of the reflectivity curve. Kraft et al. reached a similar conclusion for monolayers of F_8H_{16} for which a top interface with an ellipsoidal curvature could not fit their data.²³
- The densities of the two layers as observed in XR agree well with the calculated values. This is not expected for model II where an increased density of the bottom layer due to the bended fluorocarbon parts would result.
- GIXD of $F_{14}H_{20}$ indicates that the fluorinated parts of the molecules are arranged perpendicular to the surface in a layered structure. Depending on temperature and history the $-(CF_2)_n$ -layer is either crystallized or smectic (liquid-like), which does not make much of a difference for the present discussion. In agreement with this statement the AFM morphologies are in both cases very similar.

In model I the constant width in the frustrated direction should depend on the length of the CH_2 parts. Indeed we observed for various choices of CF_2 -length that the width increases with n_H , the number of CH_2 groups. A larger value of n_H is expected to allow a larger variation of CH_2 -conformations, and thus more possibilities to support the CF_2 -layer. We conclude that a model I for the finite width of the ribbons will be close to the cartoon mode I of Figure 4.8. Of course it should be realized that a realistic model will not be as extreme as pictured, and can be expected to contain local differences in structure.

Finally we come to a discussion of ribbons versus spirals. From the results so far it seems that the ribbon pattern is the natural way to accommodate a monolayer of $F_{14}H_{20}$. This is conclusively explained by the difference between the closed packing along the ribbons and the frustrated packing in the transverse direction. The latter leads to a constant width that is preserved in the spiral structure as well. Note that spiral-like patterns have been reported earlier in monolayers, but have usually been treated as hemispherical

micelles.²³ In the present case of $F_{14}H_{20}$, the resolution of the SFM micrographs unambiguously depicts turning of short ribbons. This observation is quantitatively supported by the finite width of the crystalline peaks in Figure 4.6 (see also Table 4.3). In fact both right-handed and left-handed structures are found. Yet, Figure 4.1 is one of many examples where no change of rotation direction is observed within the spiral. Starting from the ribbon structure we note that the kinks along the ribbon direction can be directed either forward or backward. A transition from one direction to the other leads to a defect. The stresses in packing near such a defect can be released by creating a discrete angular step along the ribbon leading to a change in the azimuthal tilt angle direction. The ribbon needs a preference to continue in the same direction after the first turn, to explain the spirals of Figure 4.2b. Note that the first azimuthal step can be directed either clock-wise or counter-clockwise, which explains the two types of spirals. At present it is not clear to us why a certain angular direction is continued and why the nano-spirals can be obtained so easily with narrow size distributions. We would like to speculate that the spirals grow at the air solution interface at the outer end and wind to the center where they can grow no further due to the steric constraint. This might also explain why we find closed toroids only sometimes and why spirals can be compressed and open again.

4.4 Conclusions

We have presented a surface x-ray scattering (XR and GIXD) study on the structure of supported monolayers of $F(CF_2)_{14}(CH_2)_{20}H$. SFM images have shown lateral structuring expressed in two morphologies: straight ribbons and nanospirals. Whether the one or the other formed depended on the solvent from which the sample was prepared. The characteristic dimensions of both morphologies are identical which suggests that the difference resides in the molecular packing. XR analysis confirmed that the height of the structures is less than the extended length of the molecules and revealed the layered structure of the monolayer. GIXD proves that the fluorinated segments tend to pack with a chain orientation normal to the layer in an arrangement that would allow large 2D-films. Thus, the observed peculiarities in the morphology must be caused by ordering of the hydrocarbon chains. We have proposed a model with tilted hydrocarbon chains resulting in

an easy axis that explains qualitatively the ribbon structure and the origin of the nanospirals. In the direction perpendicular to the easy axis the mismatch of dense packing of CF_2 and CH_2 groups can be released by partial disordering of the alkyl chains corresponding to an interlayer. Yet this incommensurability can only be compensated over a restricted length. These arguments give a first coarse indication for the formation of stripes or bands of uniform width. In one direction the incommensurability is compensated by the tilt of the hydrocarbon chain towards the normal of the monofilm, in the other direction it can be compensated only for a limited length by partial disordering of the hydrocarbon segment.

References

- [1] Riess J. G., *Tetrahedron* 58, 4113, 2002.
- [2] Lo Nostro P., *Curr. Opin. Colloid Interface Sci*, 8, 223, 2003.
- [3] Mahler W., Guillon D., Skoulios A., *Mol. Cryst. Liq. Cryst. Lett.* 2, 111, 1985.
- [4] Viney C., Russell T. P., Depero L.E., *Liq. Cryst.* 5, 1783, 1989.
- [5] Rabolt J. F., Russell T. P., Twieg R. J., *Macromolecules* 17, 2786, 1984.
- [6] Russell T. P., Rabolt J. F., Twieg R. J., Siemens R. L., Farmer B. L., *Macromolecules* 19, 1135, 1986.
- [7] Höpken J., “Fluorocarbon-Hydrocarbon Molecules, structural Components for Self-Organizing Materials”, *Dissertation*, University of Twente, Netherlands, 1991; Höpken J., Pugh C., Richtering W., Möller M., *Makromol. Chem.* 189, 911, 1988.
- [8] Krafft M. P., *Adv. Drug. Deliv. Rev.* 47, 209, 2001.
- [9] Johns K., Stead G., *J. Fluor. Chem.* 104, 18, 2000.
- [10] Padua A. A. H., *J. Phys. Chem. A* 106, 116, 2002.
- [11] Marczuk P., Lang P., *Macromolecules* 31, 9013, 1998.
- [12] Gang O., Ellmann J., Möller M., Kraack H., Sirota E. B., Ocko B. M. and Deutsch M., *Europhys. Lett.* 48, 761, 2000.
- [13] Marczuk P., Lang P., Findenegg G. H., Mehta S. K., Moeller M., *Langmuir* 18, 6830, 2002.
- [14] Mourran A., Tartsch B., Gallyamov M., Magonov S., Lambreva D. M., Ostrovskii B. I., Dolbnya I. P., de Jeu W. H., Moeller M., *Langmuir* 21, 2308, 2005.
- [15] See, for example, M.Tolan, *X-ray scattering from Soft Matter Thin Films*, (Springer, Berlin), 1999.
- [16] Lo Nostro P. L., Ched S.-H., *J. Phys. Chem.* 97, 6535, 1993.
- [17] Daillant J., Gibaud A., *X-ray and neutron reflectivity: principles and applications* (Springer-Verlag), 1999.
- [18] Ocko B. M., Wu X. Z., Sirota E. B., Sinha S. K., Gang O., Deutsch M., *Phys. Rev. E* 55, 3164, 1997.
- [19] Fera A., Dolbnya I. P., Opitz R., Ostrovskii B.I., de Jeu W.H., *Phys. Rev. E* 63, 020601, 2001.

- [20] Huang Z., Acero A. A., Lei N., Rice S. A., Zhang Z., Schlossman M. L., *J. Chem. Soc. Faraday Trans. 92*, 545, 1996.
- [21] Krafft M-P., *Curr. Opin. Coll. Interf. Sci. 8*, 243, 2003.

Chapter 5 Order and disorder in smectic elastomers

In this chapter we present a high-resolution x-ray study of the effect of random crosslinking on the one-dimensional translational ordering in smectic elastomers. At a small crosslink density of about 5%, the elastomer network stabilizes the smectic structure against layer-displacement fluctuations, and the algebraically decaying layer ordering extends up to several micrometers. With increasing concentration of crosslinks, the finite size of these domains is strongly reduced, indicating that disordering takes over. Finally, at a crosslink concentration of 20%, the structure factor can be described by a Lorentzian, which signals extended short-range correlations. The findings are discussed in terms of recent theories of quenched disorder by random fields.

5.1 Order and disorder in smectic systems

In a three-dimensional crystal the particles vibrate around well-defined lattice positions with an amplitude which is small compared to the lattice spacing. As the dimensionality is decreased, fluctuations become increasingly important. As a result, long-range translational order cannot exist in less than three dimensions, as it would be destroyed by thermal fluctuations. For example, for a two-dimensional solid positional correlations decay algebraically with of distance. Similar behavior is found for the layer ordering in smectic-A liquid crystals.^{1,2} In this phase the orientationally ordered elongated molecules are arranged in stacks of fluid layers. The one-dimensional layer correlations do not possess long-range ordering. This is also the case for surfactant membranes^{3,4,5} and the melts of lamellar block copolymers.^{1,6} In all these systems thermally excited fluctuations cause the mean-squared layer displacements of the layer positions to diverge logarithmically with the system size (Landau-Peierls instability). As a result, the correlation function describing the one-dimensional translational ordering decays with distance r algebraically as $r^{-\eta}$, in which the exponent η is small and positive (quasi-long-range order).

A completely different way of changing positional ordering can occur under the influence of a random field. One way to apply such a field is by confinement of a smectic phase in highly porous, chemically bonded silica gels (aerogels). The effect on the smectic ordering in the vicinity of the smectic-nematic phase transition has been well characterized by several methods including x-ray diffraction, specific heat, static and dynamic light scattering measurements.⁷⁻¹⁰ Even at very low concentrations of the aerogels (about 1-3%) the ordering of the smectic layers is destroyed, which is consistent with the theoretical prediction that any quenched disorder, no matter how weak, should cause this effect.^{12,13} The remaining smectic order persists only locally on a macroscopic length scale $\xi(T) \approx 100$ nm, the 'x-ray correlation length' (see Figure 5.1). Thus there is no distinct smectic-A phase and nematic-smectic-A transition anymore in such a system, in agreement with theoretical predictions.^{7,11,13}

By attaching liquid-crystalline (mesogenic) molecules to a polymer backbone via flexible linkages the one-dimensional quasi-long-range layer ordering can be combined with polymer properties. In the smectic phase the mesogenic units still form ordered stacks

of fluid monolayers, while the backbone chains perform a random walk within the two-dimensional layers and hop across them. The backbone polymer, in turn, can be weakly crosslinked to form an elastomer network,⁶ in which the side chains retain their internal mobility (Figure 1.6). The macroscopic rubber elasticity introduced via such a percolating network interacts with the liquid crystal ordering field.¹⁵ In nematic elastomers, in which

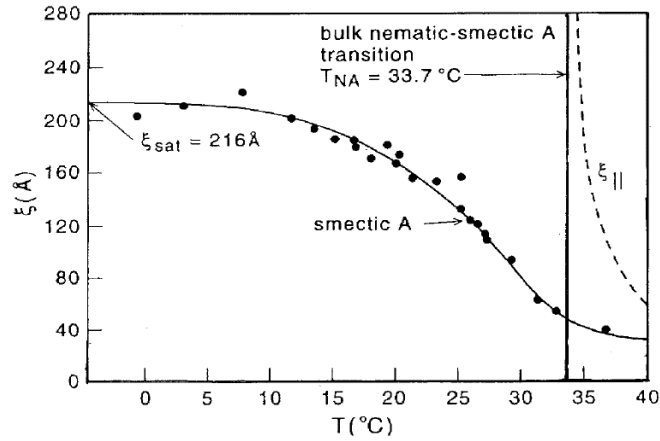


Figure 5.1. Correlation length for smectic layer ordering in bulk (broken line) and in a random field of aerogels (full line). In the latter case the smectic layer correlation at T_{NA} is reduced to only about 4 nm. After Ref. [14].

the mesogenic units are only orientationally ordered, this leads to specific orientational transitions and memory effects driven by the soft rubber elasticity. In a smectic elastomers, the distributed crosslinks create constraints on the relative displacement of the layers. Unlike in conventional smectics, the layers cannot move easily across the polymer network: in particular, movement is impossible across crosslinking points where a polymer backbone is attached. Hence, layer displacement fluctuations are coupled to distortions of the elastomer network and are therefore energetically penalized. Consequently, the thermally excited layer displacements are suppressed, which effectively stabilizes the one-dimensional periodic structure. This can lead to reestablishment of true long-range order,

even though the translational order is still one-dimensional as in a non-crosslinked smectic polymer.¹⁶⁻¹⁸

On another hand, the random network of crosslinks is a source of disorder in the system. The effects of randomness and disorder on the properties of condensed matter systems constitute a source of challenging problems.¹¹ Examples include systems as different as the pinning of the Abrikosov flux vortex lattice by impurities in superconductors, disordered Ising magnets, superfluid transitions in helium and the confined phase transitions in smectic liquid crystals mentioned above. Usually, the effects of so-called quenched disorder are considered, in which the source of distortion is fixed in space and time. Smectic elastomers provide a new model system to investigate the effects of disorder due to a random field. However, the situation is complex, because the crosslinking defects are flexible chains, which are embedded in the fluctuating elastomer network and therefore not fixed. We conclude that in smectic elastomers two opposing tendencies exist that can interfere with each other: the suppression of layer displacement fluctuations, which enhances the translational order in the system, and the random dislocation field of the crosslinks, which should lead to a frustrated distorted state with increased disorder.

In order to probe the effect of the crosslinking on the positional correlations in smectics we conducted a high-resolution x-ray scattering study of smectic elastomers with different crosslink densities. High-resolution x-ray diffraction of the (quasi) Bragg peak due to the smectic layering provides direct information about the asymptotic behavior of the positional correlation function. In the next section we shall discuss the smectic structure factor in some detail, while, in Sec. 5.3, the extension to smectic elastomers will be made. After a description of the experiments in Sec. 5.4, the results are finally presented and discussed in Sec. 5.5. At a relatively small density of the crosslinks (about 5%), the elastomer network enhances the stability of the layered structure against layer-displacement fluctuations. The layer ordering extends to length-scales of several micrometers, yet true long-range positional order does not develop. With increasing crosslink density up to 15%, the algebraic decay of the positional correlations is preserved but within smectic domains of decreasing size, down to values as small as 400 nm. Finally, the smectic ordering is destroyed at a crosslink concentration of about 20% and is replaced by short-range smectic correlations with a characteristic correlation length of the order of 100 nm.

5.2 The structure factor in the smectic phase

In this section we summarize some basic theory concerning the smectic phase, which serves as a reference point for the later discussion. The free energy associated with elastic deformations of the smectic layers can be described by the displacement field $u(\mathbf{r}) = u_z(r_\perp, z)$ that characterizes layer displacement along the layer normal z , in dependence of the in-plane position r_\perp . Symmetry considerations lead to the so-called Landau-de Gennes free energy¹⁵

$$F = \frac{1}{2} \int d^3r \left\{ B \left(\frac{\partial u(\mathbf{r})}{\partial z} \right)^2 + K \left[\frac{\partial^2 u(\mathbf{r})}{\partial x^2} + \frac{\partial^2 u(\mathbf{r})}{\partial y^2} \right]^2 \right\}, \quad (5.1)$$

where the elastic moduli B and K correspond to compression and bending of the layers, respectively (see Figure 5.2), and the integration is carried out over the volume of the system.

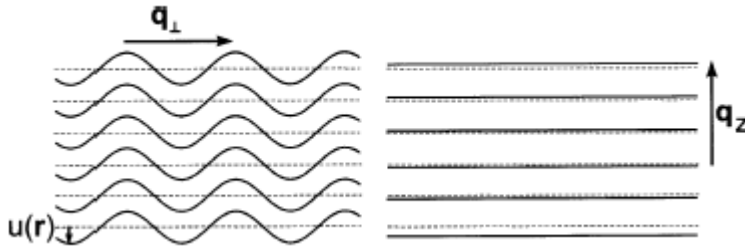


Figure 5.2. Undulation and compression of smectic layers with corresponding wave vector.

In the full spectrum of layer displacement modes the long-wavelength fluctuations are dominant, which can be easily understood from the observation that a solid rotation or translation (infinite wavelength) does not cost any energy. In the harmonic approximation, the mean-squared value of fluctuations of wave vector \mathbf{q} is given by:

$$\langle u^2(\mathbf{q}) \rangle = \frac{k_B T}{Bq_z^2 + Kq_\perp^4}, \quad (5.2)$$

where $u(\mathbf{q})$ is the Fourier transform of the layer displacement field $u(\mathbf{r})$, q_z and q_\perp are the wave vector components along and perpendicular to the layer normal, respectively, and $k_B T$ is the thermal energy. The mean-squared layer displacement $\langle u^2(\mathbf{r}) \rangle$ is obtained by integrating over the full spectrum of wave displacement vectors. The integration boundaries are $2\pi/L \leq q_z \leq 2\pi/d$ and $2\pi/W \leq q_\perp \leq 2\pi/a$, where L and W are the sample size normal to the layers and in-plane, respectively, a is the lateral molecular spacing and d the layer spacing. For many common situations $W \gg L$ and $a < d$, in which case the limits of integration can be expanded to $W \rightarrow \infty$ and $a \rightarrow 0$. In that case we obtain:

$$\langle u^2(\mathbf{r}) \rangle = \frac{k_B T}{8\pi\sqrt{KB}} \ln\left(\frac{L}{d}\right). \quad (5.3)$$

The logarithmic divergence of $\langle u^2(\mathbf{r}) \rangle$ with the sample size is known as Landau-Peierls instability.^{19,20} As a consequence, for sufficiently large L , the fluctuations would become of the order of the layer spacing d and the layered structure would be wiped out. However, for a typical experimental situation, L is in the mm-range, $K \approx 10^{-11}$ N and $B \approx 10^7$ N/m², leading to a layer-displacement amplitude $\sigma = \langle u^2(\mathbf{r}) \rangle^{1/2} \approx 0.5 - 0.7$ nm. Thus, in terms of the relative displacement we find $\sigma/d \approx 0.2$ and the smectic layers are still well defined. Note the difference from common three-dimensional crystals, for which the expression for the mean-squared layer displacement is given by

$$\langle u^2(\mathbf{r}) \rangle = \frac{k_B T}{\pi a C}. \quad (5.4)$$

At room temperature this gives for typical values of the elastic modulus $C \approx 10^{10}$ N/m² and $a \approx 0.5$ nm a result $\sigma = \langle u^2(\mathbf{r}) \rangle^{1/2} \approx 0.02$ nm, while no dependence on the sample size is present.

The positional order in a condensed medium can be described by the density-density correlation function. Thus, the quasi-long-range order in smectic-A systems is distinguished from true long-range order by its pair-correlation function $G(\mathbf{r})$. In the harmonic approximation this function can be written as

$$G(\mathbf{r}) = \langle \rho(\mathbf{r})\rho(0) \rangle - \langle \rho(\mathbf{r}) \rangle \langle \rho(0) \rangle \propto \langle \exp\{iq_0[u(\mathbf{r}) - u(0)]\} \rangle = \exp\left[-\frac{1}{2}q_0^2 g(\mathbf{r})\right] \quad (5.5)$$

where

$$g(\mathbf{r}) = \langle [u(\mathbf{r}) - u(0)]^2 \rangle \quad (5.6)$$

is the layer displacement correlation function, $\rho(\mathbf{r})$ is the density distribution and $q_0 = 2\pi/d$. In the case of true long-range order, $G(\mathbf{r})$ approaches a constant value for $r \rightarrow \infty$. In contrast, the short-range order of liquids is described by a $G(\mathbf{r})$, which decays exponentially. Caillé has calculated the pair-correlation function describing the algebraic decay, typical for the layer structure of a smectic liquid crystal, in the harmonic approximation, which is given by^{21,4}

$$G(\mathbf{r}) = G(r_\perp, z) \propto \exp(-2\eta\gamma_E) \left(\frac{2d}{r_\perp}\right)^{2\eta} \exp\left[-\eta E_1\left(\frac{r_\perp^2}{4z\sqrt{KB}}\right)\right] \quad (5.7)$$

where γ_E is Euler's constant and $E_1(x)$ the exponential integral. The dimensionless exponent η describing the power-law behavior can be written as

$$\eta = \frac{q_0^2 k_B T}{8\pi\sqrt{KB}} \quad (5.8)$$

Using the asymptotic expression for the exponential integral in Eq. (5.7) the following limiting cases can be written explicitly:

$$\begin{aligned} G(0, z) &\propto z^{-\eta}, \\ G(r_\perp, 0) &\propto r_\perp^{-2\eta}. \end{aligned} \quad (5.9)$$

As discussed in Sec. 2.1, in x-ray experiments, the Fourier image of the density-density correlation function $G(\mathbf{r})$ is determined, which can be expressed as the structure factor:

$$S(\mathbf{q}) = \int d^3r G(\mathbf{r}) \exp(i\mathbf{q} \cdot \mathbf{r}). \quad (5.10)$$

$G(\mathbf{r})$, as obtained from a measurement of $S(\mathbf{q})$, yields information on the nature of the translational order. For an ideal three-dimensional crystal, the long-range translational order results in delta-function-type diffraction peaks (Bragg peak), $S(\mathbf{q}) \sim \delta(\mathbf{q} - \mathbf{q}_n)$ (see Figure 5.3). The Bragg peak at each reciprocal lattice vector position is accompanied by weak tails of thermal diffuse scattering $\sim (\mathbf{q} - \mathbf{q}_n)^2$. The algebraic decay of the positional correlations of the smectic layers given by Eq. (5.9) implies that the x-ray structure factor has a power-law singularity (Caillé structure factor) (Figure 5.3).^{21,22}

$$\begin{aligned} S(q_{\perp} = 0, q_z) &\propto (q_z - q_n)^{-2+\eta_n}, \\ S(q_{\perp}, q_z = q_n) &\propto q_{\perp}^{-4+2\eta_n}, \end{aligned} \quad (5.11)$$

where $\eta_n = n^2\eta$ with η given by Eq. 5.8 while n is an integer. Thus, the peaks in the smectic structure function are called quasi-Bragg rather than Bragg peaks, and smectics are said to be characterized by quasi-long-range order. In a conventional liquid the positional correlations decay exponentially with distance as $G(\mathbf{r}) \sim \exp(-r/\xi)$, in which ξ is the

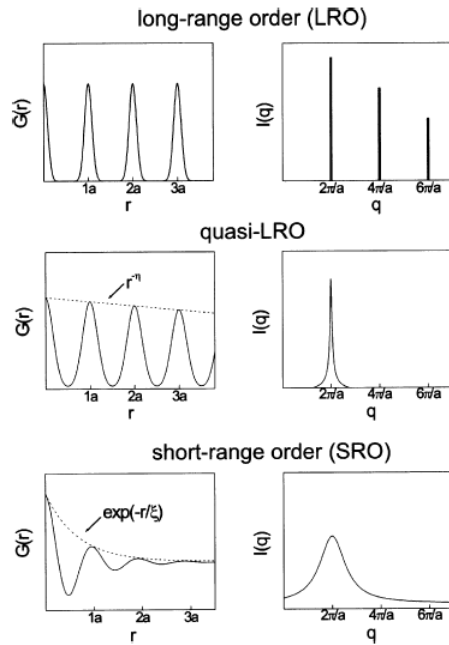


Figure 5.3. Correlation function and resulting diffraction pattern for various types of positional order.

correlation length, giving a Lorentzian scattering profile of Eq. 2.5 (Figure 5.3). Convolution of a Gaussian resolution function with a Lorentzian structure factor gives a lineshape with ‘long tails’ of the Lorentzian type. The correlation length ζ can be determined experimentally from the full width at half maximum (FWHM) of the diffraction peak as $\zeta \sim \pi/\text{FWHM}$.

In the case of finite-size samples,²² boundaries restrict the integration region in Eq. 5.10. The resulting x-ray intensity consists of the thermal diffuse scattering given by Eq. 5.11, and a true, albeit weakened, Bragg peak (see Figure 5.4). The form factor of a domain of dimension L leads to a Bragg peak of width $\sim L^{-1}$ and height $\sim LW^{2-2\eta}$ (W being the lateral size), which is accompanied by wings decreasing on average as $1/q^2$. However, the effects of the algebraic decay mask this contribution to the lineshape. The central part of the experimental longitudinal peak can be described by a Gaussian lineshape convoluted with the resolution function (also Gaussian). Its width is determined by the average size of the finite smectic domains, which can be estimated using the Scherrer formula as $L \sim 2\pi/\text{FWHM}$.

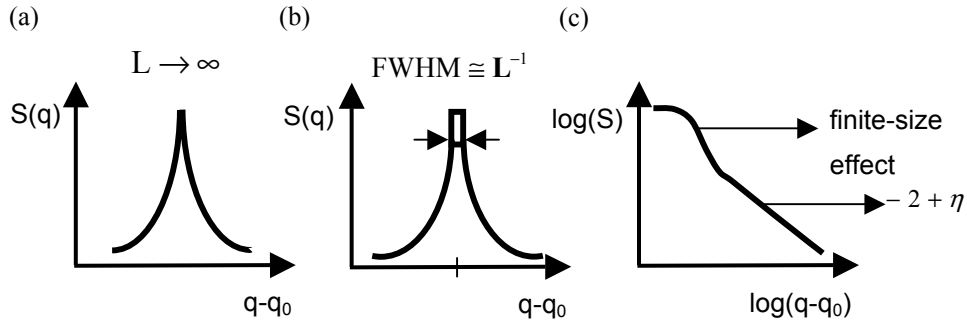


Figure 5.4. Characteristic lineshapes of systems with quasi-long-range order: (a) power-law singularity for infinite sample; (b) quasi-Bragg peak due to the finite-size effects; (c) double logarithmic plot of (b) revealing the contributions to the lineshape from finite sizes as well as from thermal fluctuations.

For samples with a mosaic distribution of the layer normal, Caillé’s structure factor (Eq. 5.11) must be averaged over the orientations of the various regions of the sample. For

a sample with random orientations, the average over all solid angles is analogous to that in powder diffraction. It gives for a longitudinal scan an intensity distribution $S(\mathbf{q}) \sim q^{-1+\eta}$ instead of $q^{-2+\eta}$, as quoted for an ideally oriented sample. For smectic samples with a small mosaic distribution (typically 1.5°), the structure factor varies continuously with increasing wave vector q from a power-law with index $2-\eta$ to one with index $1-\eta$. The transition occurs at a characteristic wave vector q_c given by²³

$$q_c = \lambda q_n \phi^2 / 4, \quad (5.12)$$

where ϕ is the mosaic distribution (angular misorientation) of the layer normal as measured by the FWHM of a rocking curve at a given wave vector position q_n .

The various contributions to the x-ray intensity distribution in the vicinity of the Bragg peak are summarized in Figure 5.5. At large deviations from q_n , the power-law due to the algebraic decay of the positional correlations leads to a behavior $(q_z - q_n)^{-2+\eta}$; at smaller

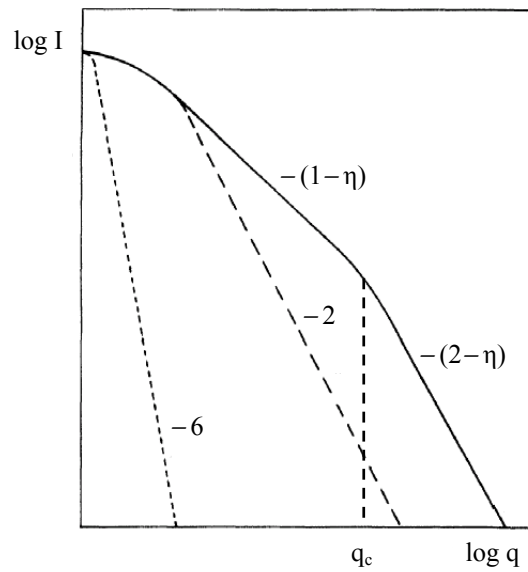


Figure 5.5. Summary of the various contributions to the lineshape: the solid line represents scattering by thermal fluctuations, the long-dashed line indicates finite-size effects, the short-dashed line the possible instrumental resolution (after Ref. [23]).

distances from q_n the mosaic effect gradually takes over giving $(q_z - q_n)^{-1+\eta}$; finally the central part including the FWHM is determined by the finite-size Bragg peak. To obtain reliable information on the structure factor, a high-resolution x-ray set-up should be used, capable of measuring length scales on the order of a micrometer. In addition, the tails of the resolution function should decrease as a function of $q_z - q_n$ faster than $(q_z - q_n)^{-2}$.

5.3 Smectic elastomers

In contrast to conventional smectics, smectic elastomers¹⁶⁻¹⁸ have an additional source of long-wavelength distortions: the elastic deformations determined by the local network displacements. Hence, the smectic ordering field interacts with the elastomer network elasticity. On the continuum level, the coupling between the layer fluctuations and the rubber matrix can be considered as layer pinning by crosslinks, which provides a penalty for local relative displacements.¹⁶⁻¹⁸ This coupling is an addition to the smectic elastic energy of deformation and to the elastic energy of the anisotropic rubber network as a whole. As a result the usual smectic degeneracy with respect to uniform layer rotations (no resistance to shear) is lost. Though the resulting expression for the free energy as a function of layer displacements is rather complicated, the essential physics can be seen from the dispersion law for the phonon modes of the elastomers:¹⁸

$$\langle u^2(\mathbf{q}) \rangle_{\perp} = \frac{k_B T}{B^* q_z^2 + 2C_5^* q_{\perp}^2 + 2C_5^{eff} (q_z^4 / q_{\perp}^2)}, \quad (5.13)$$

where B^* and C_5^* are renormalized bulk compression and shear moduli, respectively. The elastic modes now feature a solidlike elastic energy proportional to an overall squared power q^2 . This can lead to reestablishment of true long-range order, even though the translational order is still one-dimensional, as in a noncrosslinked smectic polymer.⁶ Accordingly, the resultant x-ray diffraction should show an extended range of Bragg peaks accompanied by diffuse scattering decaying as $(q - q_n)^2$. In contrast to the algebraic decay in smectics, in this case the exponent η can attain the limit $\eta \rightarrow 0$. As typical values of the

exponent are quite small ($\eta \approx 0.1$), it is difficult to discriminate between Caillé lineshapes and thermal diffuse scattering. The best way to distinguish between these two cases is to consider higher-order diffraction peaks for which the lineshape scales in the case of quasi-long-range order according to $\eta_n = n^2\eta$.

So far, the crosslinks – pinning the layers in a number of points – were assumed not to alter the smectic density. However, the crosslinks are also expected to disturb the layer structure itself, which effect will become more important with increasing concentration. A preferential reduction of the smectic density around a crosslink can be modeled by a local random field that adjusts the phase of the smectic density wave.¹⁷ A full theory of such a system – still to be developed – might require a correlation function that is a product of two independent terms describing size and strain effects, respectively. Such possibilities have been discussed for various defect situations by Krivoglaz.²⁴ This problem is also well known in metal physics, where this type of decoupling is used to describe strain-induced lineshape broadening, increasing with q and thus with the order of the reflection.²⁵

5.4 Experimental

Materials. We have studied two types of elastomer, based on smectic-A (Sm-A) polysiloxanes (Figure 5.6), synthesized in the group of Prof. Heino Finkelmann at the Makromolekular Institute in Freiburg (Germany), as reported elsewhere.²⁶ The average degree of polymerization is about 250, with a broad distribution typical of a polycondensation reaction. Both types of elastomer contain as mesogenic groups benzoic acid phenylesters (R_1 ; R_2), and a bifunctional hydroquinone derivative (R_3) as the crosslinking agent. Type II differs from type I by the presence of a second mesogenic group (R_2). We studied elastomer I for volume fractions of crosslinks $x=0$ (homopolymer) and $x=0.5$, and elastomer II for crosslinks fractions of 0, 0.10, 0.15 and 0.20 in the Sm-A phase at room temperature. The Sm-A phase was identified by sharp ($00n$) quasi-Bragg peaks along the layer normal at a wave vector q_n , and a broad liquidlike peak from the in-plane short-range order (see Figure 5.7).

Aligned elastomer samples (typically 40×10 mm² and 0.5 mm thick) were obtained by a two-stage process. During a first crosslinking step, the networks were isotropic while

solvent was still present. The solvent was slowly removed at room temperature under a uniaxial load. During this process, the isotropic sample passed through a nematic phase, and subsequently became smectic. In the nematic phase, the director is oriented in the direction of the uniaxial stress. This determined the long direction of the sample (coinciding with the smectic layer normal) and was fixed by a second crosslinking step. Homopolymer films were prepared at temperatures close to the smectic-isotropic transition (65-75°C) by moving a spreader over a glass substrate to give films with a thickness of about 100 μm and a mosaic distribution of the layer normals $\leq 1.5^\circ$.

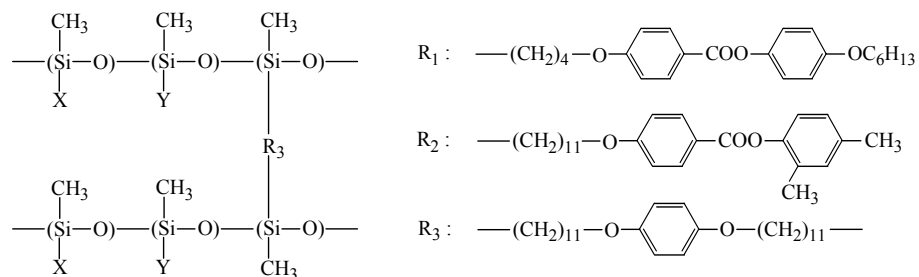


Figure 5.6. Chemical structures. Elastomer type I has $X=Y=R_2$; type II has $X=R_2$ (45%) and $Y=R_1$ (55%).

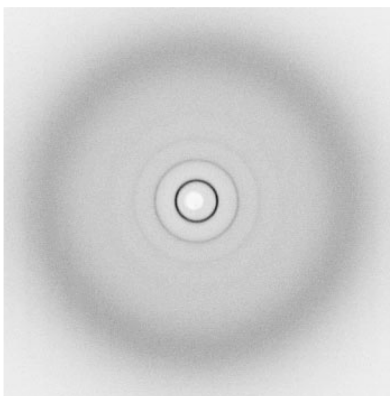


Figure 5.7. Example of an x-ray scattering pattern of smectic-A phase (after Ref. [27]).

X-ray set-up. The experiments were performed at the Exxon beam line X10A at the National Synchrotron Light Source, Brookhaven National Laboratory (Upton, NY, USA) with 8 keV radiation (wavelength $\lambda = 0.155$ nm). The scattering plane (z, x plane) was vertical with the q_z axis parallel to the smectic layer normal. Hence the quasi-Bragg peaks were measured along q_z while the mosaic distribution was determined by transverse (rocking) curves varying q_x at different $q_z = q_n$. The resolution function in the scattering plane was close to a Gaussian with $\Delta q_z = 0.003$ nm⁻¹ (FWHM). Using a double bounce Ge(111) monochromator and a triple-reflection channel-cut Ge(220) or Si(111) analyzer crystal, the wings were reduced to a functional dependence $\sim (q_z - q_n)^{-4.5}$ at small deviations from the Bragg position, and to $\sim (q_z - q_n)^{-3}$ further away (see Figure 5.8). The resolution function along q_x could be taken to be a delta-function. Out of the scattering plane, the resolution was set using slits to $\Delta q_y = 0.02$ nm⁻¹. The incident intensity was about 5×10^9 cts/s; the beam size was 0.5×1 mm² (V×H). All data were normalized in order to get

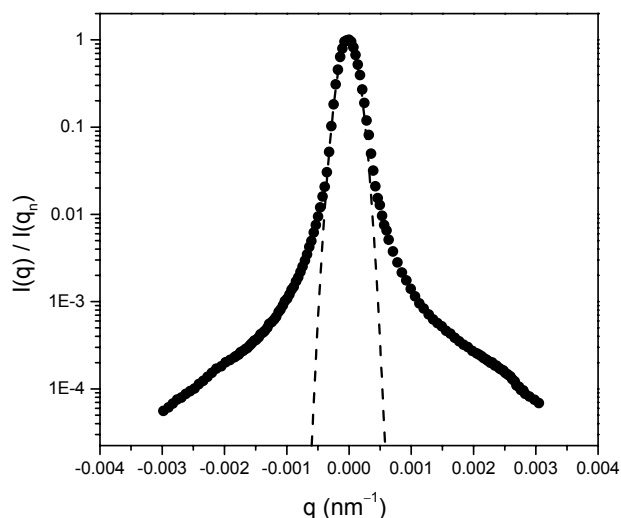


Figure 5.8. X-ray lineshape of a triple-pass Ge(220) crystal. The dashed line is a Gaussian fit to the relevant central part of the experimental data.

intensity values at the maximum of the peaks equal to 1, by calculating $I(q)/I(q_n)$. Resolution corrections were made using the relation $\sigma_{\text{peak}} = (\sigma_{\text{exp}}^2 - \sigma_{\text{res}}^2)^{1/2}$, where σ_{exp} , σ_{res} ,

σ_{peak} are the FWHM of the experimental peak, the resolution function and the real peak, respectively. Corrections were made for the first order harmonics of samples with $x=0.10$, 0.15 , where the intensities of the tails of the peaks were close to the background level. In practice, this was done by subtraction of the values of the experimentally measured background from the intensity of the peaks.

5.5 Results and discussion

Figures 5.9-11 show typical x-ray profiles from elastomer I and II for different volume fraction of crosslinks x , together with the lineshape of the direct beam and the corresponding linear fits for η . Figure 5.9 displays the experimental data for the first-order reflections from elastomers I and II with $x=0$. The homopolymer II shows two orders of reflection originating from the smectic layering. The intensity of the second order was not sufficient to obtain precise data for the tails of the structure factor; therefore we do not display the respective curve. The characteristic features of the scattering from the smectic layers are clearly seen on a double-logarithmic scale: a rounded central region at small deviations from q_n due to the finite size of the smectic domains, and tails with power-law behavior $(q - q_n)^{2-\eta}$ at larger distances. For both types of polymer, the quasi-Bragg peaks are not resolution limited, from which the finite size of the smectic domains along the layer normal can be estimated to be of dimension $L \approx 1 \mu\text{m}$. Away from the center of the peaks algebraic decay is observed with $\eta_n/n^2 = \eta = 0.10 \pm 0.04$, similar to that reported for other smectic polymers.²⁸ Interestingly, upon crosslinking the homopolymer the layer spacing d increases (see Table 5.1). However, the relative increase $\Delta d/d \leq 0.03$ is rather small and d stays almost constant upon further increase of the crosslink density.

For elastomer I at $x=0.05$ (Figure 5.10), the finite size L depends slightly on the order of the reflection. The exponent of the algebraic decay was found to be larger than for the homopolymer: $\eta = 0.19 \pm 0.03$, which might indicate some ‘softening’ of the smectic layering due to coupling with the network of the elastomer. Upon crosslinking, the finite size of the smectic domains increases from $L \approx 1 \mu\text{m}$ up to $L \approx 3 \mu\text{m}$. The full experimental results are summarized in Table 5.1.

Table 5.1. Summary of linewidth results for elastomer I.

Concentration crosslinks x	Order n	d (nm)	Δq_z (10^{-3} nm^{-1})	Mosaic distribution (deg)
0	1	2.78	8.8	1.7
0.05	1	2.88	2.1	0.9
0.05	2		2.4	1.3

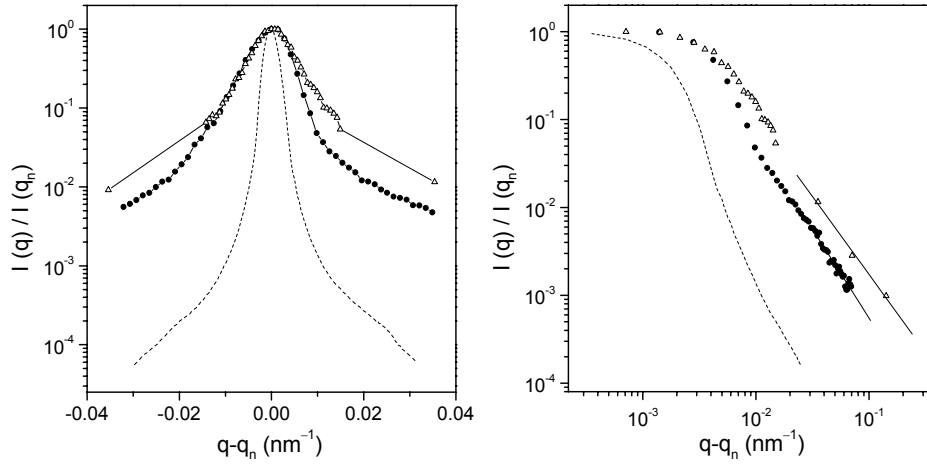


Figure 5.9. X-ray lineshape of the first-order diffraction peaks of a homopolymer ($x=0$) of compound I (full circles) and II (open triangles). The dashed line is the direct beam from a triple-pass Ge(220) crystal; the full lines are drawn to lead the eyes.

For elastomer II at $x=0.1$ three orders of diffraction have been measured (Figure 5.11) with a systematic increase of the exponent η_n with n . The general trend is well described by the scaling law $\eta_n/n^2 = \eta = 0.15 \pm 0.04$. The FWHM of the quasi-Bragg peaks is not resolution limited and the central part can be well described by a Gaussian. From the first-order peak, the finite size along the layer normal is calculated to be $L \approx 1.6 \mu\text{m}$. Rather surprisingly, we find a broadening of the peak with the order of reflection, which has not previously been reported for smectic systems. The same behavior is observed at larger crosslink densities. The complete results are summarized in Table 5.2. They indicate a systematic increase of the peak width along q_z (Figure 5.12) as well as along q_x (mosaic

distribution), both with increasing crosslink density (Figure 5.13b) and with the order of the reflection (Figure 5.13a).

Table 5.2. Summary of linewidth results for elastomers II.

Concentration crosslinks x	Order n	d (nm)	Δq_z (10^{-3} nm^{-1})	Mosaic distribution (deg)
0	1	2.86	9.3	1.6
0	2		12	3.3
0.1	1	2.91	5.5	2.6
0.1	2		10.3	2.6
0.1	3		23	3.3
0.15	1	2.92	24	7.5
0.15	2		35	8.1
0.2	1	2.92	51	15

For elastomer II at $x=0.15$, the algebraic decay of the positional correlations is still preserved with $\eta \approx 0.15$, but is masked by a substantial broadening of the peak along q_z and by the mosaic of the sample (see Table 5.2). Later measurements²⁹ indicate that the observed asymmetry (Figure 5.11c) is an artifact. The central part of the peak can still be well described by a Gaussian (see Figure 5.14a), and the FWHM indicates smectic domains as small as $L \approx 400$ nm. Similar to the case where $x=0.1$, the linewidth increases with diffraction order. Finally, at $x=0.20$ only a first-order diffraction peak can be observed, which is strongly broadened along q_z and q_x . The intensity profile can no longer be described by a Gaussian, but fits to a Lorentzian centered at $q_0 = 2.16 \text{ nm}^{-1}$ with a correlation length $\xi \approx 50$ nm (see Figure 5.14b). We conclude that at crosslink concentrations between 15 and 20%, a crossover takes place from quasi-long-range order (characterized by an algebraic decay of the positional correlations in a finite domain) to short-range positional correlations characteristic of a disordered phase.

The above findings are summarized in Figure 5.15. At the low crosslink concentration $x=0.05$, the finite size of the smectic domains is 2-4 times larger than for the homopolymer. Evidently, the elastomer network enhances the stability of the layered structure in agreement with the predictions of layer pinning theory, Eq. 5.13. From the intensity ratio of

the second-order Bragg peak to the first harmonic we find that $\langle u^2(\mathbf{r}) \rangle$ in the elastomers is about two times smaller than in the corresponding homopolymer. However, the system still shows slow (algebraic) decay of the positional correlations. This can be contrasted with earlier results³⁰ in which the introduction of 2-5 mol% crosslinks was reported to restore true long-range order, though for a rather different elastomer system. However, in these experiments only a first-order peak was observed and no proof from a scaling relation could be given.

With increasing concentration of crosslinks, the disorder gradually takes over as indicated by broadening of the x-ray peaks along and perpendicular to the layer normal. For $x=0.10$ the width Δq_z of the peak along q_z increases quadratically with the order of the reflection n (see Figure 5.12). In addition, the mosaic also increases with n (Figure 5.13a). Such behavior cannot be described by a simple harmonic theory of smectics in which the width of the peaks remains constant with the order of diffraction. Evidently, the layer displacements around crosslinks (or other types of defects generated by them) are no longer small compared to the layer spacing. The observed dependence of the peak width on crosslink density and on the order of diffraction resembles that predicted for an elastic fields of distant dislocations or other topological defects.^{23,31}

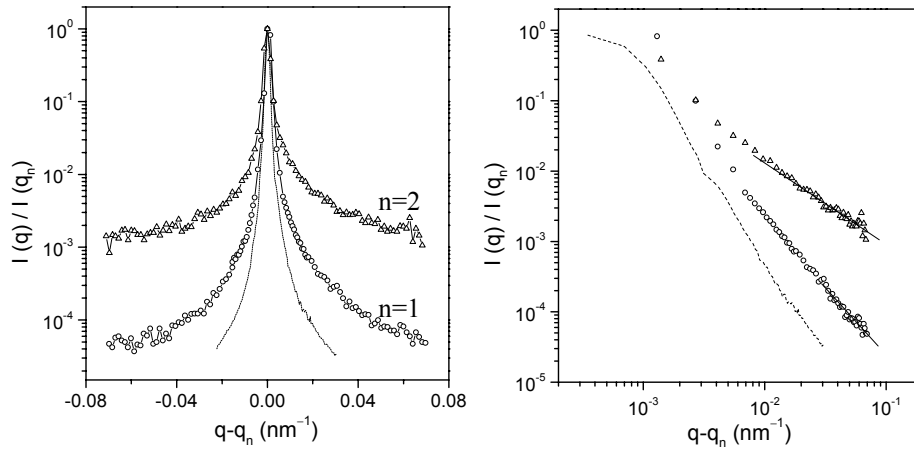


Figure 5.10. X-ray lineshape of two orders of diffraction peaks of elastomer I at $x=0.05$. Open circles and triangles indicate experimental data for the first and second harmonic, respectively. The dashed line is the direct beam from a triple-pass Si(111) crystal; the full lines are drawn to lead the eyes.

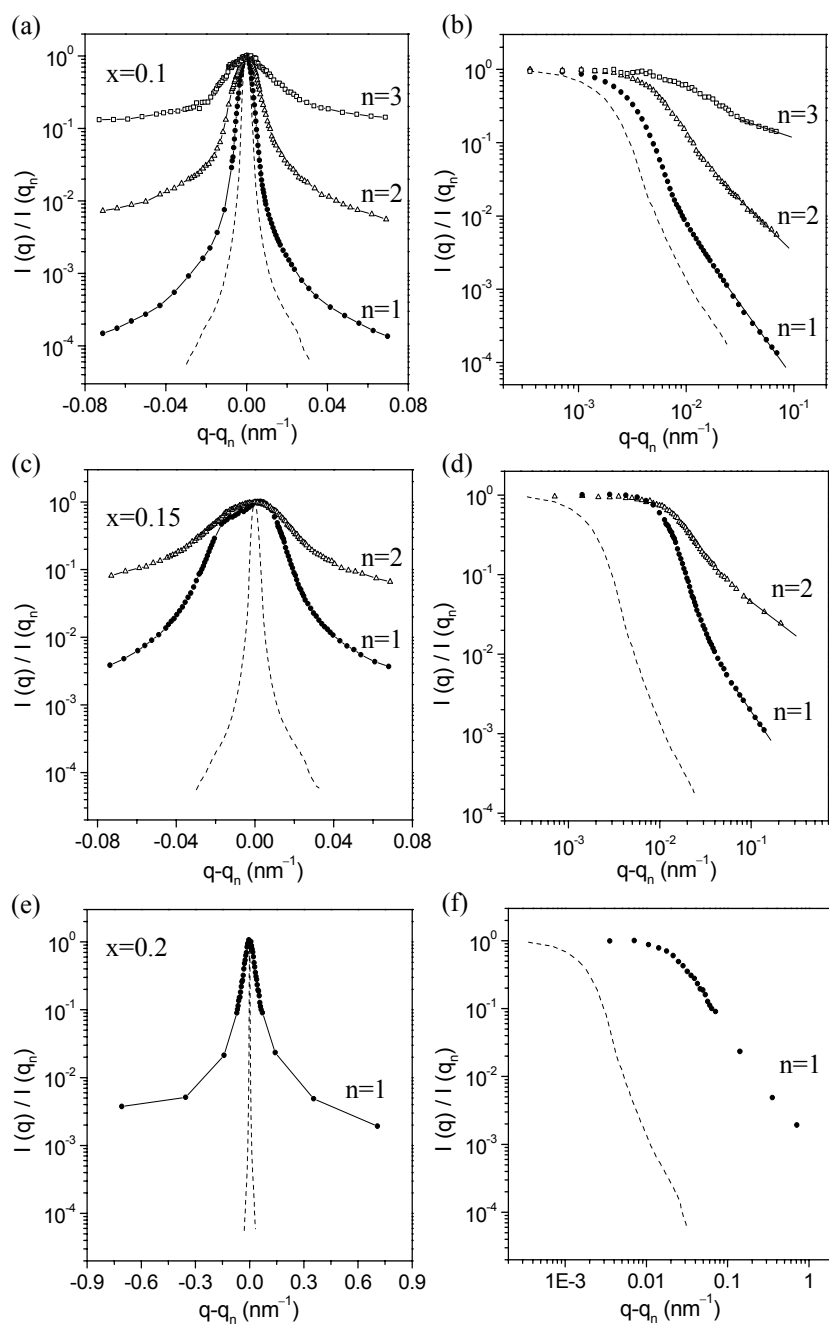


Figure 5.11. X-ray lineshape of diffraction peaks of elastomer II for $x=0.10$, 0.15 and 0.20 . The dashed line is the direct beam from a triple-pass Ge(220) crystal; n denotes the order of the diffraction peak; the full lines are drawn to lead the eyes.

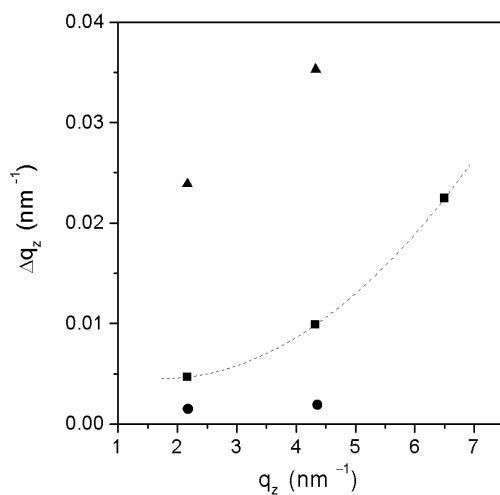


Figure 5.12. *FWHM of the Bragg peaks as a function of the peak position q_z . Full circles, squares and triangles indicate experimental data for elastomer I at $x=0.05$, elastomer II at $x=0.1$ and 0.15 , respectively.*

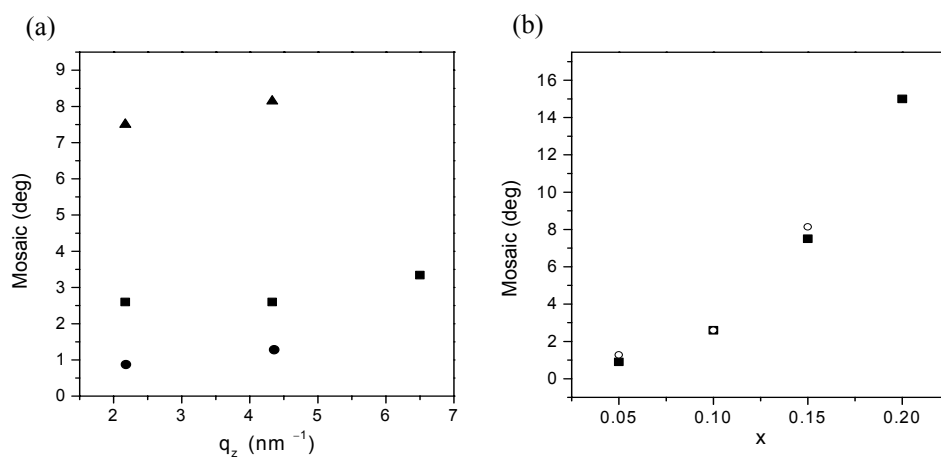


Figure 5.13. (a) *Mosaic distribution as a function of the Bragg position q_z . Full circles, squares and triangles indicate experimental data for elastomer I at $x=0.05$, and elastomer II at $x=0.1$ and 0.15 , respectively.* (b) *Mosaic distribution as a function of the crosslink density x . Full squares and the open circles indicate experimental data for the first and second harmonic, respectively.*

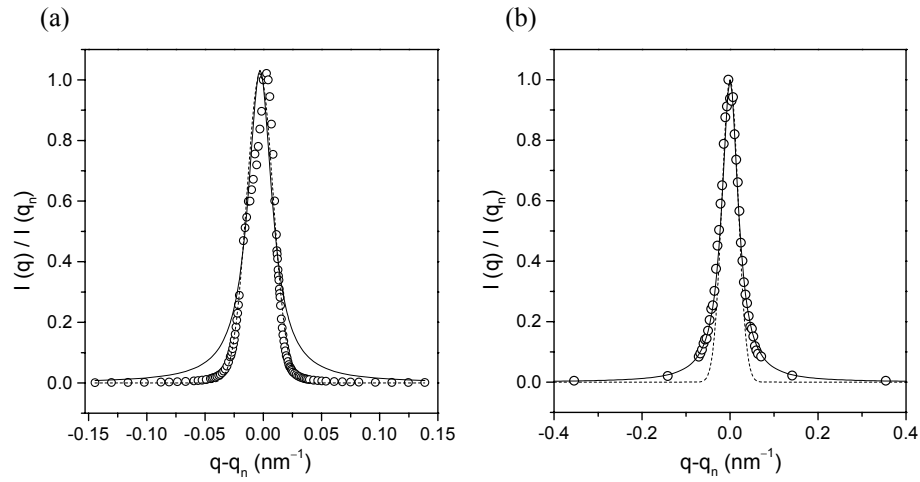


Figure 5.14. First harmonic lineshape of elastomers II at (a) crosslink density $x=0.15$ and (b) $x=0.2$. The dashed line is the best fit to a Gaussian, the full line to a Lorentzian.

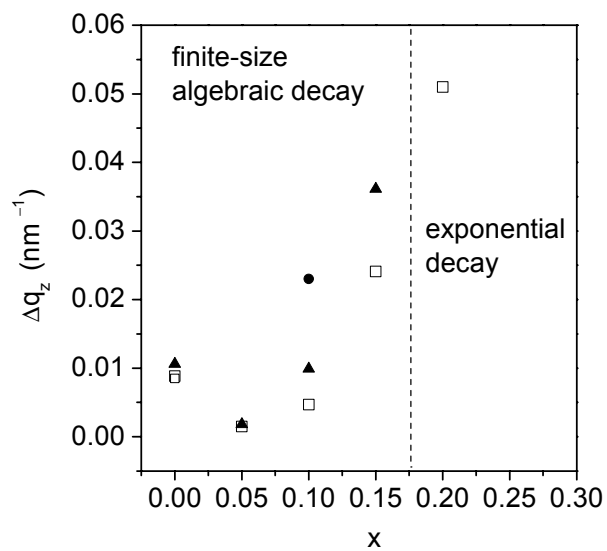


Figure 5.15. Summary of the overall behaviour of the FWHM of the smectic Bragg peak as a function of the crosslink density; squares: first harmonic, triangles: second harmonic, circles: third harmonic.

At a crosslink concentration $x=0.15$, the finite size of the smectic domains has diminished to a few hundred nm, but the central part of the x-ray peaks is still well described by a Gaussian function. In addition, the algebraic decay of the smectic layer correlations is preserved. At higher crosslink densities, the quasi-long-range order is lost, giving way to extended short-range smectic correlations. This transition leads to the replacement of the power law structure factor by an anisotropic Lorentzian, characteristic of a positionally disordered nematic-like phase. Though this behavior is consistent with the general predictions for quenched disorder, the theory cannot explain how the algebraic decay can survive up to such a large crosslink density. The analogy might fail because in smectic elastomers the crosslinks are not rigidly fixed in space and time, but consist of flexible chains embedded in the slowly fluctuating elastomer. Clearly this makes the situation very different from the type of quenched disorder found for low-molecular mass smectics confined in aerogels. We speculate that above a certain concentration of crosslinks, many defects of higher strength are generated, which causes large displacements of the layers, $q_u \gg 1$. The elastic field of such defects, for example, dislocation loops, will suppress the Bragg peaks and lead to a diffuse scattering with a Lorentzian lineshape.

5.6 Conclusions

We have used high-resolution x-ray scattering to gain insight into the positional correlations in smectic elastomers with increasing number of crosslinks. At small crosslink density, the elastomer network enhances the stability of the layer structure against thermal fluctuations. Up to a relatively large concentration of about 15% crosslinks, the algebraic decay of the positional correlations survives in domains of decreasing size. After a further increase of the density of crosslinks, the smectic ordering is destroyed by the random field of the crosslinks and replaced by extended short-range correlations.

The measurements presented indicate that the one-dimensional periodicity in smectic elastomers remains a challenging and unresolved issue. The randomly disordered state is believed to correspond to thermodynamic equilibrium of the system, with depressed thermal fluctuations on top.³² Contrary to smectics in silica aerogels – essentially an isotropic confinement – the rubbery network in smectic elastomers is highly

anisotropic. Crosslinking in the nematic phase under uniaxial stress produced the well-aligned, optically transparent samples studied. Alternatively, random disorder could be introduced through crosslinking in the isotropic phase, leading to a highly non-uniform smectic state. Also the nature (rigidity, length) of the crosslinker is expected to play a role. It remains to be investigated if and how these differences affect the positional correlations in the system and the lengths scales involved.

References

- [1] Chaikin, P. M., Lubensky, T. C., Principles of Condensed Matter Physics (Cambridge University Press), 1995.
- [2] De Gennes, P. G., Prost, J., The Physics of Liquide Crystals (Oxford Science Publications), 1993.
- [3] de Jeu, W. H., Ostrovskii, B. I., Shalaginov, A. N., *Rev. Mod. Phys.* 75, 181, 2003.
- [4] Als-Nielsen, J., Litster, J. D., Birgeneau, R. J., Kaplan, M., Safinya, C. R., Lindegaard-Andersen, A., Mathiesen, S., *Phys. Rev. B* 22, 312, 1980.
- [5] Safinya, C. R., D. Roux, G. S. Smith, S. K. Sinha, P. Dimon, N. A. Clark, A. M. Belloq, *Phys. Rev. Lett.* 57, 2718, 1986.
- [6] M. Warner and E. M. Terentjev, Liquid Crystal Elastomers (Clarendon Press, Oxford), 2003.
- [7] Bellini, T., Radzihovsky, L., Toner, J., Clark, N., *Science* 294, 1074, 2001.
- [8] Park, S., Leheny, R. L., Birgeneau, R. J., Gallani, J. L., Garland, C. W., Iannacchione, G. S., *Phys. Rev. E* 65, 050703, 2002.
- [9] Leheny, R. L., Park, S., Birgeneau, R. J., Gallani, J. L., Garland, C. W., Iannacchione, G. S., *Phys. Rev. E* 67, 011708, 2003.
- [10] Kutnjak, Z., Kralj, S., Lahajnar, G., Zumer, S., *Phys. Rev. E* 68, 021705, 2003.
- [11] Blatter, G., Feigelman, M., Geshenbain, V., Larkin, A., Vinokur, V., *Rev. Mod. Phys.* 66, 1125, 1994.
- [12] Larkin, A. I., *Sov. Phys. JETP* 31, 784, 1970; Giamarchi, T., LeDoussal, P., *Phys. Rev. B* 52, 1242, 1995.
- [13] Radzihovsky, L., Toner, J., *Phys. Rev. Lett.* 79, 4214, 1997; Radzihovsky, L., Toner, J., *Phys. Rev. Lett. B* 60, 206, 1999.
- [14] N.A. Clark, T. Bellini, R.M. Malzbender, B.N. Thomas, A.G. Rappaport, C. Muzny, D.W. Schaefer, L. Hrubesh, *Phys. Rev. Lett.* 71, 3505, 1993.
- [15] Landau, L. D., Lifschitz, E. M., Pitaevskii, L. P., Statistical Physics (Pergamon, New York), 1980.
- [16] Terentjev, E. M., Warner, M., Lubensky, T. C., *Europhys. Lett.* 30, 343, 1995.
- [17] Olmsted, P. D., Terentjev, E. M., *Phys. Rev. E* 53, 2444, 1996.
- [18] Osborne, M. J., Terentjev, E. M., *Phys. Rev. E* 62, 5101, 2000.

- [19] Landau, L. D., *Phys. Z. Sowjet* 11, 545, 1937.
- [20] Peierls, R. E., *Helv. Phys. Acta* 7 supplement II, 81, 1934.
- [21] Caillé, A., C. R., *Acad. Sci. Paris B* 274, 891, 1972.
- [22] Gunther, L., Imry, Y., Lajzerowicz, J., *Phys. Rev. A* 22, 1733, 1980.
- [23] Kaganer, V. M., Ostrovskii, B. I., de Jeu, W. H., *Phys. Rev. A* 44, 8158, 1991.
- [24] Krivoglaz, M., *X-ray and Neutron Diffraction in Non-ideal Crystals* (Springer, Berlin), 1996.
- [25] Ungar, T., Borbely, A., *Appl. Phys. Lett.* 69, 3173, 1996.
- [26] Nishikawa, E., Finkelmann, H., *Macromol. Chem. Phys.* 198, 2531, 1997.
- [27] Nishikawa, E., Finkelmann, H., *Macromol. Rapid Commun.* 19, 181, 1998.
- [28] Nachaliel, E., Keller, E. N., Davidov, D., Boeffel, C., *Phys. Rev. A* 43, 2897, 1991.
- [29] Muresan, A. and de Jeu, W.H. (unpublished results).
- [30] Wong, G., de Jeu, W. H., Shao, H., Liang, K., Zentel, R., *Nature* 389, 576, 1997.
- [31] Kaganer, V. M., *Sov. Phys. Crystallogr.* 34, 327, 1989.
- [32] Terentjev, E. M., *Macromol. Symp.* 117, 79, 1997.

Chapter 6 Concluding remarks and outlook

The self-assembling materials investigated in this thesis are interesting both from a scientific and technological perspective. As model systems they bring together fundamental phenomena such as strive for orientational and positional order, and self-assembly, phase transitions, and frustration of the order by internal and external constraints. This allowed us to study the interplay of these aspects and to search for means to control the ordering. On the other hand the diversity in systems is also considerable and in the course of time objectives have changed to some extent. Nevertheless, for all soft condensed systems described, x-ray methods – applied in nonstandard and non-trivial ways – allowed us to (partially) resolve the phase morphology and the nature of positional order.

The work on semicrystalline-amorphous poly(butadiene-*b*-ethyleneoxide) diblock copolymers was initially concerned with studying confined crystallisation. The idea that in such systems equilibrium chain folding can be achieved should provide a handle on the crystallisation process itself. To some extent this has been proven to be indeed the case. The chain folding observed in lamellar films with a (half-)integer number of stems is remarkable in its consequence of a counterintuitive anisotropic expansion. The theoretical meaning and the differences with the bulk behaviour are still not completely understood. In terms of confinement, a film on a substrate gives limited possibilities compared to a film between two hard surfaces. This applies to homopolymers, but especially to block copolymers in which also the block ordering would be constrained. We have extensively investigated this possibility at Hasylab (Hamburg) in cooperation with Dr. Oliver Seeck. To observe Kiessig fringes from two parallel Si wafers limiting a polymer film of B₃₇₀₀E₄₃₀₀ requires ultimate control of their parallelism. Unfortunately the method of ‘self-settlement’ was not reproducible. Hence no report of these experiments is included in this thesis. Alternatively some questions about the phase behaviour of asymmetric poly(butadiene-*b*-ethyleneoxide) have been investigated. In particular the establishment of non-lamellar structures for the bulk B₃₇₀₀E₂₉₀₀ clarified discrepancies in the literature about the origin of the vertical lamellae appearing in thin films.

The semifluorinated alkanes F(CF₂)_n(CH₂)_mH have a possible practical importance for applications as repellent systems. Much work is being devoted to fluorinated systems attempting to retain these properties using as little fluorine as possible incorporated. In comparison with the available literature and the complex behaviour as a function of the length (n, m) of the respective chains, our work on F₁₄H₂₀ has been modest. However, the

discovery in the group of Prof. Martin Moeller (Aachen) of ‘ribbons’ and ‘spirals’ in thin films and the transition between them is remarkable. We have contributed to the understanding by establishing that the close-packed tilted structure gives an easy direction, which allows the system to accommodate the shape mismatch between the fluorinated and hydrogenated parts. Though no full explanation of the spiralling could be given, this has brought a much-needed new element into the discussion.

Finally influencing the ordering in smectic elastomers by crosslinking constitutes a somewhat different topic of more fundamental nature. It can be placed in the much broader framework of the physics of (dis)ordering by random fields. Over the last years considerable progress has been made in the group of Prof. Heino Finkelmann (Freiburg) regarding the preparation of ordered smectic elastomers. This allowed us to perform for the first time quantitative measurements of the subtle, partially counteracting, effects of increased crosslinking on the smectic layering. New theory is required to fully understand these results. More variations are still possible – like changing the nature of the crosslinker – which are being pursued at the time of this writing.

Summary

This thesis describes a series of experiments on the ordering of self-assembling soft condensed systems. A variety of the different types of material have been considered. These include block copolymers, semi-fluorinated alkanes and smectic elastomers, which all consist of incompatible constituting units that give rise to structural order on mesoscopic length scales. Possible control over the self-assembly can be achieved by varying either external conditions (bulk, thin films) or molecular parameters. Various x-ray methods have been applied to probe both bulk structures (small- and wide-angle x-ray scattering) and surface ordering (x-ray reflectivity and grazing-incidence x-ray diffraction). In appropriate cases the results were complemented with direct images from atomic force microscopy and optical microscopy.

Semicrystalline-amorphous block copolymers are central to this work. They provide unique opportunities to examine the interplay of various types of phase transition, resulting in a rich phase behaviour including molecular ordering over several length scales. We report on the microphase separation and crystallization in a series of poly(butadiene-*b*-ethyleneoxide) diblock copolymers. In these materials the amorphous polybutadiene blocks provide a rubbery confinement for the crystallization of the polyethyleneoxide blocks. Two approximately symmetric compounds with lamellar phases have been investigated, both in bulk and in uniformly oriented thin films. They differ in molecular mass, the order-disorder transition being within experimental reach for the low-mass compound. A weakly first-order phase transition occurs at about 110°C accompanied by strong concentration fluctuations above this temperature.

Upon crystallization of the polyethyleneoxide block in bulk, the long period of the crystalline lamellae varies continuously with the crystallisation temperature (degree of supercooling). In thin films the lamellar period increases upon crystallisation in spite of the decreasing volume (increasing density) of polyethyleneoxide. The crystalline sublayers adjust to discrete values corresponding to an integer or half-integer number of folded stems. The difference with the bulk behaviour has been tentatively attributed to the two-dimensional crystallization process in thin films, which causes the lateral sliding to become important.

Upon crystallisation in the bulk of an asymmetric poly(butadiene-*b*-ethyleneoxide) diblock copolymer with hexagonal cylinder morphology, a conflict arises between the crystallisation in lamellae and the microphase separated structure. The resulting coupling leads to a perforated lamellar phase. In thin films the situation is more complex due to wetting layers of polybutadiene and polyethyleneoxide that develop at the top and bottom interface, respectively. These layers force the cylinders in the interior of the film to orient parallel to the substrate. Because of this hybrid structure, the final result after crystallization in thin films varies with history and the associated kinetic pathways.

In the next system, semifluorinated alkanes $F(CF_2)_{14}(CH_2)_{20}H$, the antagonistic nature of the two building units and the mismatch in their cross section results in distinct superstructure formation. We have performed an x-ray analysis of self-assembled monolayers of $F_{14}H_{20}$ in the form 'ribbons' or 'spirals'. Analysis of the x-ray reflectivity puts the hydrogenated part of the molecules near the surface. The films have a uniform thickness that is consistent with a monolayer with a tilt angle of 127° at the linkage between the fluorocarbon and the hydrocarbon segments. Geometrical considerations indicate that a tilt of 122° allows closed packing of all-trans planar alkyl segment in one direction. This results in an 'easy axis' that explains qualitatively the ribbon structure. Perpendicular to this direction the system is highly frustrated leading to a finite width of the ribbons. Grazing incidence x-ray diffraction indicates that the fluorinated segments indeed orient normal to the film interfaces as required in such a model.

Finally the algebraically decaying ordering in smectic liquid crystal systems has been studied. The quasi-long-range correlations are due to thermal fluctuations of the layers that diverge logarithmically with the size of the sample. The ordering can be influenced by application of a random field, which was accomplished by crosslinking a smectic liquid-crystalline polymer to form an elastomer network. The macroscopic rubber elasticity introduced via such a percolating network interacts with the liquid-crystalline ordering field. Insight into the positional correlations was obtained by high-resolution analysis of the lineshape of the x-ray peak from the smectic layering. At a small crosslink density of about 5%, the elastomers network enhances the stability of the layer structure against thermal fluctuations. At larger concentration up to about 15% crosslinks, the algebraic decay of the positional correlations survives in domains of decreasing size. For a larger density of crosslinks the smectic ordering is destroyed by the random field of the crosslinks and

replaced by extended short-range correlations. Present theory of disordering by a random field does not account for this behaviour.

Samenvatting

Dit proefschrift beschrijft een reeks experimenten met betrekking tot de zelforganisatie van zachte gecondenseerde systemen. Daarbij komen verschillende soorten materialen aan de orde, zoals blok copolymeren, gefluorideerde alkanen en smektische elastomeren. Ze hebben gemeen dat ze opgebouwd zijn uit onderdelen die elkaar slecht verdragen, hetgeen aanleiding geeft tot structuurvorming op mesoscopische schaal. Controle over het proces van zelforganisatie kan verkregen worden door variatie van externe condities (bulk of dunne lagen) of van moleculaire parameters. Verschillende röntgen-methoden zijn gebruikt voor het onderzoek aan bulk structuren (röntgenverstrooiing bij kleine en grote hoeken) en aan oppervlakken en dunne lagen (röntgenreflektiviteit en röntgenverstrooiing onder totale reflectie). In enkele gevallen zijn deze resultaten aangevuld met directe beelden via atomaire krachtmicroscopie en optische microscopie.

In de geschetste context nemen blok copolymeren met een half-kristallijn en een amorf blok een centrale positie in. Ze bieden unieke mogelijkheden om de interacties tussen verschillende typen fase-overgangen te bestuderen, wat resulteert in een veelvoud van fasen waarin de moleculen over diverse lengteschalen geordend zijn. Microfasescheiding en kristallisatie worden behandeld voor een serie diblok co-polymeren van het type poly(butadieen-*b*-ethyleenoxide). In deze materialen kristalliseert het polyethyleenoxide in de rubberachtige omgeving van het amorphe polybutadieen. Twee vergelijkbaar symmetrische verbindingen, die beiden microfasescheiding vertonen in een lagenstructuur, zijn zowel in bulk als in uniform georiënteerde dunne films onderzocht. Door het verschil in molekulgewicht kan voor de laag-moleculaire verbinding de orde-wanorde overgang experimenteel bereikt worden. Een faseovergang van de eerste orde vindt plaats bij ongeveer 110°C; boven deze temperatuur treden sterke fluktuaties op in de concentratie van de twee componenten.

Bij kristallisatie van polyethyleenoxide in de bulk verandert de dikte van de kristallijne lagen op een continue wijze met de kristallisatietemperatuur (de mate van onderkoeling). In dunne films neemt bij kristallisatie de dikte van de lagen toe, ondanks het ontstane kleinere volume (grotere dichtheid) van het polyethyleenoxide. De kristallijne lagen nemen nu echter discrete diktes aan waarin het gevouwen polymeer een geheel aantal

malen past, of de helft daarvan. Het verschil met het continue gedrag in de bulk wordt toegeschreven aan het tweedimensionale karakter het kristallisatieproces in dunne films waardoor de laterale diffusie belangrijk wordt.

Bij kristallisatie van een asymmetrisch poly(butadien-*b*-ethyleenoxide) blok copolymeer met een hexagonaal cilindrische morfologie in de bulk, treedt een conflict op tussen de kristallisatie in lagen en de structuur van de geordende microfase. De resulterende interactie leidt tot een fase met een structuur van geperforeerde lagen. In dunne films is de situatie ingewikkelder door het optreden oppervlak-geïnduceerde lagen van polybutadien en polyethyleenoxide, respectievelijk aan het luchtoppervlak en aan het substraat. Deze lagen zorgen ervoor dat de cylinders in het binnenste deel van een film parallel aan het substraat gaan staan. Door deze hybride structuur is het eindresultaat na kristallisatie in dunne films afhankelijk van de voorgeschiedenis en het daardoor bepaalde kinetische traject.

In het tweede systeem, half-gefluorideerde alkanen van het type $F(CF_2)_{14}(CH_2)_{20}H$, ontstaan verschillende superstructuren door het antagonisme van de twee groepen in combinatie met het verschil in hun dwarsdoorsneden. Met behulp van röntgenmethoden zijn spontaan geordende monolagen van $F_{14}H_{20}$ op een substraat in de vorm van 'linten' of 'spiralen' geanalyseerd. De resultaten van röntgenreflektiviteit tonen aan dat de alkylketen zich aan het substraat bevindt. De structuren in de films hebben een homogene dikte die overeenkomt met een monolaag als daarin een hoek van 127° wordt aangenomen bij de overgang tussen de gefluorideerde en de gealkyleerde segmenten. Geometrische overwegingen leiden bij een nabij gelegen hoek van 122° tot een dichtste pakking van alkyl segmenten in één richting. Dit resulteert in een voorkeurrecht die kwalitatief de langgerekte structuur van linten verklaart. Loodrecht op deze richting is het systeem gefrustreerd, wat leidt tot een eindige breedte van de linten. Röntgenverstrooiing onder totale reflectie toont aan dat de gefluorideerde segmenten loodrecht op het filmpoppervlak staan, zoals vereist in het voorgestelde model.

Als laatste onderdeel is de algebraïsch afnemende ordening in smektisch vloeibare kristallijne systemen bestudeerd. De daardoor beperkte korrelaties over grote afstanden worden veroorzaakt door thermische fluktuaties van de lagen, welke logaritmisch toenemen met de grootte van het preparaat. De manier van ordenen kan beïnvloed worden door toepassing van een random veld. Dat is gedaan door verknoping van een smektisch

vloeibaar kristallijn polymeer tot een elastomeer. Tussen de zo geïntroduceerde macroscopische rubber-elasticiteit van het netwerk en het ordende veld van het vloeibaar kristal treedt koppeling op. Inzicht in de korrelaties tussen de posities van de smektische lagen is verkregen door analyse van de lijnvorm van de röntgenpiek, waarbij een hoog oplossend vermogen vereist is. Bij een kleine dichtheid van kruisverbindingen van ongeveer 5%, versterkt het elastomeer netwerk de stabiliteit van de lagenstructuur met betrekking tot thermische fluctuaties. Bij een hogere concentratie kruisverbindingen tot ongeveer 15% wordt nog steeds een algebraïsche afname van de positiekorrelaties gevonden, maar over steeds kleinere gebieden. Bij een nog hogere dichtheid van kruisverbindingen gaat de smektische organisatie verloren en wordt vervangen door (vloeistachtige) korrelaties over korte afstanden. De huidige theoriën over wanorde ten gevolge van een random veld kunnen dit gedrag niet verklaren.

Thank you!

Wim H. de Jeu, Boris I. Ostrovskii, M.A.J.Michels (Thijs), Maarten Altelaar, Liam McDonnell, Rosalind Allen, Omair Ghafur, Paige Shaklee, Ricarda Opitz, Dmytro Byelov, Tommi Markkula, Irakli Sikharulidze, Igor P. Dolbnya, Adrian Muresan, Ernst Prins, Wim Barsingerhorn, Anna Tchegotareva, Thea Hoogesteijn, Georgiana Languri, Christian Buggle, Chinmay Das, Evtim Efremov

Curriculum Vitae

Denitza Lambreva was born on March 5, 1976 in Sofia, Bulgaria. In 1998 she obtained a degree in Chemistry and Physics at the Chemistry Department of University of Sofia. The topics of her Master research projects were on the new ways of implementation of the subjects “public waste” and “wave processes” in the Bulgarian educational programs. Between October 1998 and October 2000 she specialized Chemical Engineering and worked as a research assistant in the Laboratory of Chemical Physics and Engineering (Chemistry Department, University of Sofia). The topic of her project was on the formulation and properties of mixed solid/liquid antifoams. In October 2000 she started work on a PhD project, investigating the ordering of self-assembling soft condensed systems, under the supervision of Prof.dr.ir. Wim H. de Jeu in the group “Order/Disorder in Soft Matter” at the FOM - Institute for Atomic and Molecular Physics (Amsterdam, Netherlands). The result of this work has been presented in this thesis.

